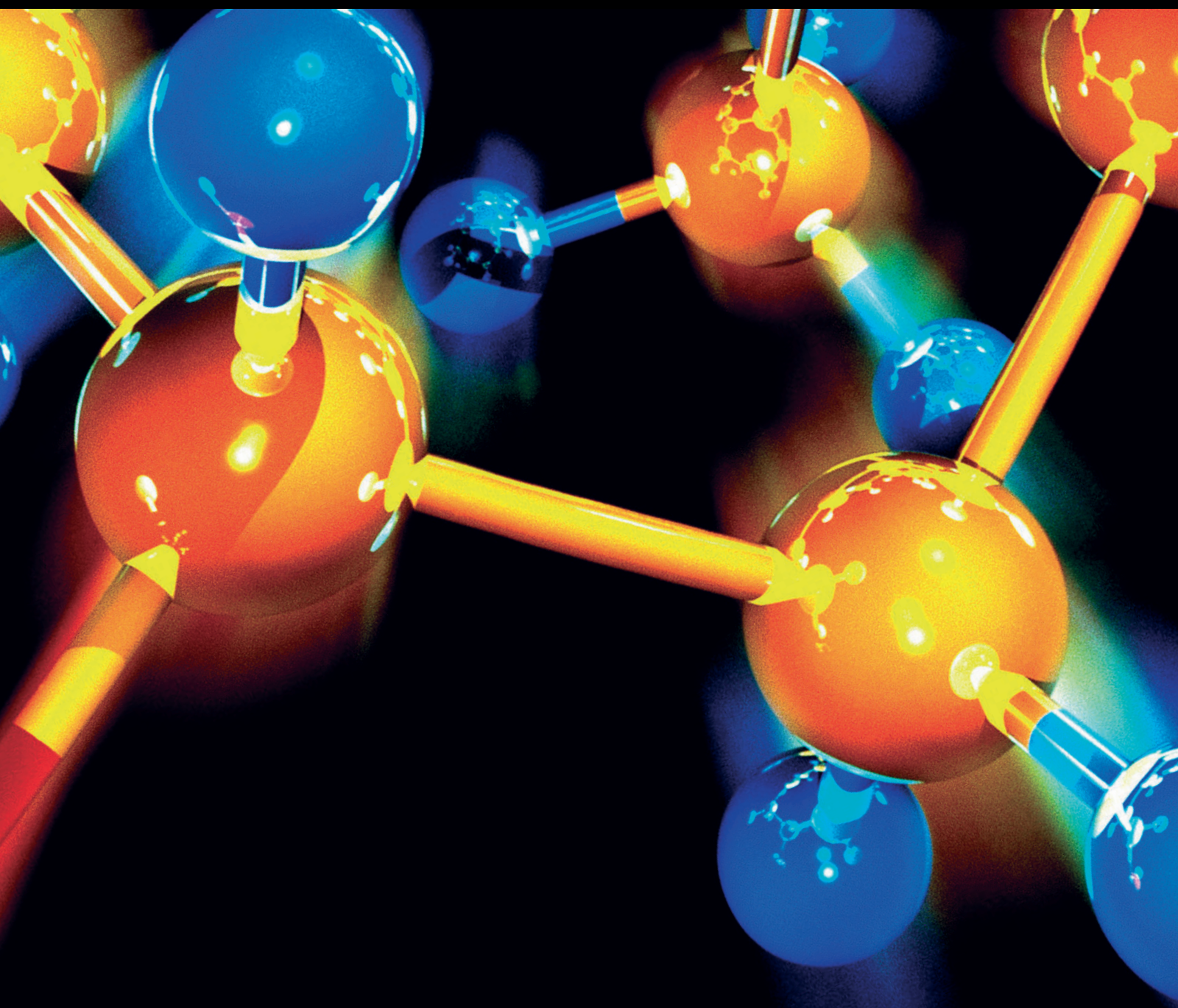


Porous Materials: Synthesis, Characterizations, and Applications

Guest Editors: Bachari Khaldoun, Juan M. Coronado, Amel Boudjema, and Talhi Oualid





Porous Materials: Synthesis, Characterizations, and Applications

**Porous Materials: Synthesis, Characterizations,
and Applications**

Guest Editors: Bachari Khaldoun, Juan M. Coronado,
Amel Boudjema, and Talhi Oualid



Copyright © 2016 Hindawi Publishing Corporation. All rights reserved.

This is a special issue published in "Journal of Chemistry." All articles are open access articles distributed under the Creative Commons Attribution License, which permits unrestricted use, distribution, and reproduction in any medium, provided the original work is properly cited.

Contents

Porous Materials: Synthesis, Characterizations, and Applications

Bachari Khaldoun, Juan M. Coronado, Amel Boudjemaa, and Talhi Oualid
Volume 2016, Article ID 5028795, 1 page

Effect of Water Adsorption on Cation-Surface Interaction Energy in the Na-Mordenite of 5.5 : 1 Si/Al Ratio

Sekou Diaby
Volume 2016, Article ID 2152180, 9 pages

Novel Mesoporous Silica Materials with Hierarchically Ordered Nanochannel: Synthesis with the Assistance of Straight-Chain Alkanes and Application

Haidong Zhang and Xiaohong Li
Volume 2016, Article ID 5146573, 16 pages

Effect of Mo-Doped Mesoporous Al-SSP Catalysts for the Catalytic Dehydration of Ethanol to Ethylene

Titinan Chanchuey, Chaowat Autthanit, and Bunjerd Jongsomjit
Volume 2016, Article ID 9672408, 8 pages

Preparation of Flower-Like Cu-WO₃ Nanostructures and Their Acetone Gas Sensing Performance

Hao Zhou, Dong-Yao Xu, Hai-Qing Zuo, Wei Liu, and Shuang Lin
Volume 2015, Article ID 382087, 7 pages

Functionalized Mesoporous Silica Membranes for CO₂ Separation Applications

Hyung-Ju Kim, Hee-Chul Yang, Dong-Yong Chung, In-Hwan Yang, Yun Jung Choi, and Jei-kwon Moon
Volume 2015, Article ID 202867, 9 pages

Evaluation of Optimal Pore Size of (3-Aminopropyl)triethoxysilane Grafted MCM-41 for Improved CO₂ Adsorption

Zhilin Liu, Yang Teng, and Kai Zhang
Volume 2015, Article ID 608265, 8 pages

An Investigation of Fractal Characteristics of Marine Shales in the Southern China from Nitrogen Adsorption Data

Jian Xiong, Xiangjun Liu, and Lixi Liang
Volume 2015, Article ID 303164, 12 pages

Editorial

Porous Materials: Synthesis, Characterizations, and Applications

Bachari Khaldoun,¹ Juan M. Coronado,² Amel Boudjemaa,¹ and Talhi Oualid³

¹*Centre de Recherche Scientifique et Technique en Analyses Physico-Chimiques, BP 384, Siège ex-Pasna Zone Industrielle, Bou-Ismaïl, 42004 Tipaza, Algeria*

²*IMDEA Energy Institute, 28935 Móstoles, Spain*

³*Universidade de Aveiro, 3810-193 Aveiro, Portugal*

Correspondence should be addressed to Bachari Khaldoun; bachari2000@yahoo.fr

Received 30 January 2016; Accepted 1 February 2016

Copyright © 2016 Bachari Khaldoun et al. This is an open access article distributed under the Creative Commons Attribution License, which permits unrestricted use, distribution, and reproduction in any medium, provided the original work is properly cited.

The interest in the field of porous materials is continually increasing; a very important step for any applications of these materials is the preparation and characterization of materials. In parallel, applications of these materials are also rising in areas such as catalysts, electrochemistry, membranes, gas separation, and selective adsorption for environmental and energy uses. Accordingly, researches in this area are often challenged with a rapidly growing literature on the subject, describing the development of porous materials with uniform pore sizes, good stability, selectivity, activity, and also enhanced crystallinity.

The contributions to the present special issue have been grouped into several categories according to their subject matter: synthesis, processing, characterizations, and property evaluation of porous materials. Contributors were requested to provide work introductions to their areas of expertise, so that the subject matter might be more generally accessible to non-specialists. Authors were also encouraged to provide the readers with updated information on different aspects of their field. The editors hope that the objectives of the present special issue have been met, so that the articles will be useful not only to working materials researchers but also to interested engineers as well as students and researchers in materials field.

*Bachari Khaldoun
Juan M. Coronado
Amel Boudjemaa
Talhi Oualid*

Research Article

Effect of Water Adsorption on Cation-Surface Interaction Energy in the Na-Mordenite of 5.5 : 1 Si/Al Ratio

Sekou Diaby

Laboratoire de Chimie-Physique, Unité de Formation et de Recherche en Sciences des Structures de la Matière et Technologie (UFR-SSMT), Université FHB de Cocody-Abidjan, 22 BP 582, Abidjan 22, Côte d'Ivoire

Correspondence should be addressed to Sekou Diaby; sekoudiaby@yahoo.fr

Received 2 October 2015; Accepted 18 January 2016

Academic Editor: Talhi Oualid

Copyright © 2016 Sekou Diaby. This is an open access article distributed under the Creative Commons Attribution License, which permits unrestricted use, distribution, and reproduction in any medium, provided the original work is properly cited.

The mobility of the Na⁺ cations localized at the inner surface of the studied mordenite zeolite depends on the material surface properties. In this work, we show that the activation energy, ΔE_{hop} , relating to the Na⁺ cation hopping displacement is associated to the surface potential and therefore can be used to get a better insight into the zeolite surface properties. Indeed, when molecules as water are adsorbed at the surface, they modify the surface potential energy and hence influence the value of ΔE_{hop} . If the adsorbed molecules are polar they directly interact with the cations which become more mobile. The more the ΔE_{hop} value is, the less the amount of adsorbed water molecules is. Alterations of the ΔE_{hop} value with respect to the amount of adsorbed water molecules are interpreted using the Dubinin model which is based on simple adsorption principle.

1. Introduction

Zeolites are crystalline aluminosilicate minerals with highly interconnected latticeworks of nanopores. These materials are thus characterized by an important surface area which gives them very interesting properties to be utilized in adsorption and catalysis. There are hundreds of zeolites showing differences in the geometric shape of the nanopore and the chemical features of the nanopore surface. The latter is directly related to the zeolite Si/Al ratio since the substitution of an Al atom for a Si one yields an excess of negative electrical charges which is compensated by cations localized at the nanopore surface. These cations are so-called extra-framework (later abbreviated EFC) or compensation cations. The type and density of EFC at the surface play a crucial role in the surface properties. For instance, the presence of H⁺ or of some metallic cations is known to be the most relevant feature that controls the adsorption and catalysis efficiency of a given zeolite. Therefore, the accurate knowledge of the EFC localization at the surface as well as their nature and density is imperative for a better understanding of the zeolite surface properties and hence for a better control of their practical uses.

Owing to electrostatic interaction, the polarity of water molecules strongly favours their adsorption on or near the cations. Hydration and dehydration (which are important practical issues) of the zeolites are therefore much dependent on the EFC. Basically, it is thought that the solvation of the EFC by the adsorbed water molecules reduces the direct interaction between the EFC and the zeolite framework and consequently enhances the EFC mobility. The change in the EFC mobility with the amount of water molecules adsorbed into the zeolite can thus be seen as a significant outcome for characterizing the water adsorption process and the zeolite surface properties.

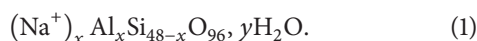
In this paper, we investigate the water adsorption into a mordenite zeolite with 5.5 : 1 Si/Al ratio and its influence on the EFC Na⁺. The amount of adsorbed water is determined using thermogravimetric analysis (TGA). Besides, Dielectric Relaxation Spectroscopy (DRS) which is well known to be a very convenient tool to probe electrical charge displacement or dipole reorientation is used to measure the evolution of the EFC mobility as a function of the amount of adsorbed water molecules and of the temperature. The activation energy for the Na⁺ mobility, ΔE_{hop} , can be then determined from the Arrhenius treatment of the DRS data. The experimental

modification of ΔE_{hop} with respect to the amount of adsorbed water molecules is finally interpreted using the Dubinin model which is based on simple adsorption principle.

The paper is constructed as follows. In Section 2.1, we recall some of the structural features of the mordenite zeolite studied here. In Section 2.2, the experimental methods used for measuring the amount of adsorbed water (TGA) and the EFC mobility (DRS) are briefly described. The Dubinin model is given in Section 2.3 whereas the analysis of the experimental results with this model is reported in Section 3.1. In Section 3.2, we discuss the data and their analysis. Conclusion is in Section 4.

2. Materials and Methods

2.1. The Na^+ Mordenite. The sodium mordenite is an aluminosilicate of the formula



Its structure consists of a linkage of tetrahedral compounds $(\text{SiO}_4)^{4-}$ and tetrahedral compounds $(\text{AlO}_4)^{5-}$, joined between them through their vertexes. Like the zeolite, the sodium mordenite is characterized by its structural unit otherwise called unit cell (u.c). It is comprised of tetrahedrons whose centres are occupied by silicon cations (Si^{4+}), or aluminium cations (Al^{3+}) whereas the oxygen atoms strongly attached to these centre cations occupy the vertexes of the tetrahedrons that link together in various ways. Each of the four tetrahedron oxygen atoms can exchange with the centre cation, an electron which causes a negative charge to arise when the concerned cation is trivalent as is Al^{3+} . Then this charge is balanced by a Na^+ cation referred to as a compensation cation or EFC (for the alkaline group or alkaline earth group). The crystalline arrangement of the tetrahedral compounds, shaped like rings between them, is imparted to the mordenite zeolite porous properties. The compensation cations while being responsible for the catalysis do not form part of the open structure of the mineral, and under certain conditions one can replace them by other cations without altering the crystal structure. Thus, channels large enough to let the ions in and out appear throughout this crystal lattice. We showed a unit cell of mordenite with a diagram in Figure 1, and we indicated the different cationic sites I, II, III, IV, and VI denoted following Mortier's classification system for the crystallographic sites [1].

The pore size varies according to the nature of the additional cation, electrical neutrality being maintained. The compensation cations contribute a lot to many properties of the mordenite zeolites. They particularly attract polar molecules like those of water. So some mordenite zeolites hold, besides the alkaline ions and alkaline earth ions, water molecules in the ducts, and cavities located within the framework of the aluminosilicates. Thus, under the effect of heat energy, a Na-mordenite crystal is expelled from its framework, water molecules. However, the crystal does not become smaller. It conserves its initial measurements and shape. The places that occupied the water molecules remain unoccupied, making the dehydrated Na-mordenite

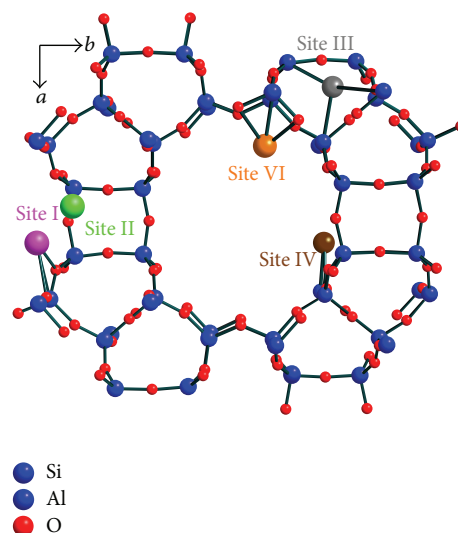


FIGURE 1: Showing the cationic sites within a unit cell of Na-mordenite [1].

into a desiccant or an adsorbent for the water vapour or for other gases. Numerous industrial methods involving heterogeneous catalytic reactions like oil refining generally employ zeolites. These reactions use elemental processes that take place at the interfacial area separating the solid catalyst from the fluid phases containing the reactants and products. So it is essential to have sufficient knowledge of reactive molecule fixation on the solid and then expect to master the successive steps in this heterogeneous catalysis.

2.2. Experimental Methods

2.2.1. Thermogravimetric Analysis (TGA) Measurements. The Na-mordenite sample placed in the capacitor as a dielectric is prepared in the following way: first, the zeolite is finely ground in an agate mortar and then it is compacted in the form of a disc, 15 mm thick and 1 mm in diameter, under a pressure of 10^8 Pa. Then, it is placed for 24 hours under an atmosphere saturated with water vapour, at temperature $T = 298$ K for the purpose of being completely hydrated. A series of measurements performed by using thermogravimetric analysis (TGA) allows the number of water molecules fastened per unit cell (u.c) to be determined for a series of treatment temperatures (TT). These measurements are carried out when inputting a known quantity of powdered zeolite fully hydrated following the steps earlier outlined, into an apparatus (SETARAM, Labsys™). The mordenite zeolite is submitted to heating, at the fixed rate of 4°C per hour, under a flow of perfectly dried argon up to the equilibrium characterized by the treatment temperature (TT). The apparatus measures uninterruptedly the mass losses due to the departure of water molecules and makes it possible to determine the remaining quantity of water, at equilibrium, in the sample, at each treatment temperature (TT) ranging from 100°C to 220°C . As shown in Figure 2, we plotted the variations in the number (N_a) of the adsorbed water

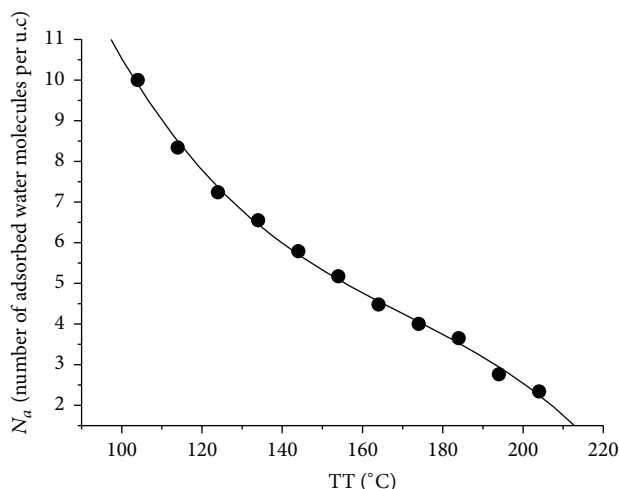


FIGURE 2: Number (N_a) of adsorbed water molecules per unit cell (u.c) of Na-mordenite as a function of treatment temperature (TT) to which the zeolite was heated.

molecules per unit cell of Na-mordenite, as a function of the treatment temperature (TT), at which the zeolite is held.

2.2.2. Study by Means of Dielectric Relaxation Spectroscopy (DRS)

(1) *Electric Polarization.* Unlike the conductors that contain free charges moving around the medium, under the effect of an electric field, the dielectrics are substances whose electrons are strongly linked to their atom so that one can observe neither a current due to the free electrons nor a current induced by the displacements of ions. By applying an electric field, however, one observes in this poor electricity conductor, that is, the dielectric, tiny displacements of unlike charges in opposite directions, and this relative movement causes dipoles to appear; the dielectric is said to be polarized. Many different mechanisms can be responsible for the development of these electric dipoles, but the experiments show that an induced polarization arises in any dielectric submitted to an electric field. The microscopic laws that describe this polarization, in the case of the polar dielectrics, allow the relative permittivity to be defined as a complex quantity (ϵ_r^*):

$$\epsilon_r^* = \epsilon_r' - j \times \epsilon_r'' \quad (2)$$

Then one shows [2–6] that, under the effect of an alternating electric field of angular frequency ω , this relative permittivity varies according to the relaxation time (τ) that characterizes the movement that brings dipoles into alignment with this field:

$$\epsilon_r^* = \epsilon_{r,\infty} + \frac{\epsilon_{r,0} - \epsilon_{r,\infty}}{1 + j \times \omega \times \tau} \quad (3)$$

By using (2) to separate the imaginary and real parts of (3), one gets

$$\begin{aligned} \epsilon_r' &= \epsilon_{r,\infty} + \frac{\epsilon_{r,0} - \epsilon_{r,\infty}}{1 + (\omega \times \tau)^2}, \\ \epsilon_r'' &= \frac{(\epsilon_{r,0} - \epsilon_{r,\infty}) \times (\omega \times \tau)}{1 + (\omega \times \tau)^2}. \end{aligned} \quad (4)$$

It is noted, regarding these equations, that the curves schematizing the value of ϵ_r'' as a function of ω , for a given value of τ , pass through a peak when $\omega = 1/\tau$. In actual practice, it is noticeable that the peaks of these curves move towards the high values of ω when the temperature (T) of the sample rises.

(2) *Jumping Mechanism.* This last remark inspired us to bring in a microscopic modelling for relating the relaxation time (τ) to the temperature (T). In this model, each of the component particles of the studied sample is placed at the minimum of a potential well when it is in its equilibrium position. It can climb out of there only when the thermal motion [7, 8] enables it to reach an energy level high enough to make it possible to cross over a potential barrier characteristic of its structural environment. If one imagines its state when the system is held at $T = 0$ K, each charge carrier is trapped into a site whose geometry solely determines its frequency of oscillations (τ_0^{-1}) in this fundamental state [9, 10]. The thermal motion provides additional energy for it, which is excited to a state of higher energy, and increases the likelihood of it crossing over the potential barrier (ΔE_{hop}) separating the two neighbouring positions characterized by the same fundamental energy. This operation enables it to move between two neighbouring equilibrium positions. This description of an elemental jumping also indicates that the value of the barrier (ΔE_{hop}) gives a measure of the energy associated with the pseudo dissociation reaction of the matching pair of charge carrier-site. Then, one can use Maxwell-Boltzmann's distribution law to calculate the number of charge carriers likely to climb out of this potential well, under the effect of the thermal motion, which allows us to express the relaxation time of the sodium cations as

$$\tau = \tau_0 \times \exp \left[\frac{\Delta E_{\text{hop}}}{k \times T} \right], \quad (5)$$

where $k = 1.38 \times 10^{-23}$ J·K⁻¹ is the Boltzmann constant. This equation can be written in the following form:

$$\text{Log} \left(\frac{1}{\tau} \right) = \text{Log} \left(\frac{1}{\tau_0} \right) - \frac{\Delta E_{\text{hop}}}{k \times T}. \quad (6)$$

The dipoles that came into being in the phenomenon of polarization within the studied Na-mordenite of 5.5:1 Si/Al ratio are oriented from the side of the rigid network of the aluminium silicate where the negative pole materializes, towards the side of the compensation cations (Na⁺), located in the sites I, IV, and VI [11–13], that is, in turn the positive pole. The calculations show that, in the system, τ_0 varies

slightly from one site to another and always remains very close to a value such that $\text{Log}(1/\tau_0) = 30.61$.

(3) *Measuring Method.* The Na-mordenite sample compacted under a pressure of 10^8 Pa, in the form of a disc, is placed between the conducting surfaces separated by a distance (d) of a plane capacitor whose vacuum capacitance is denoted by C_0 . When one applies across the capacitor a sinusoidal tension $U(\omega)$, with an angular frequency (ω), an electric polarization (\vec{p}) occurs, with a phase difference relative to the electric field \vec{E} . Under these conditions, the electric current ($I(\omega)$), flowing through the capacitor, is expressed as a complex quantity (7) and with the use of (2) can be rearranged as a sum of a real part and an imaginary one (8). Consider the following:

$$I(\omega) = U(\omega) \times [j \times \omega \times \epsilon_r^* \times C_0], \quad (7)$$

$$I(\omega) = U(\omega) \times \left[(\omega \times \epsilon_r'' \times C_0) + j \times (\omega \times \epsilon_r' \times C_0) \right]. \quad (8)$$

The capacitor filled with Na-mordenite can also be described by an equivalent circuit, formed of a parallel connection of a resistance (R) with a capacitor (with capacitance C). The admittance of such circuit is written as $[(1/R) + j \times C \times \omega]$ and allows calculating the electric current $I(\omega)$ which passes in this capacitor when it is subjected to a tension $U(\omega)$:

$$I(\omega) = U(\omega) \times \left[\frac{1}{R} + j \times C \times \omega \right]. \quad (9)$$

The comparison of (8) and (9) leads to

$$\begin{aligned} \epsilon_r'' &= \frac{1}{R \times C_0 \times \omega}, \\ \epsilon_r' &= \frac{C}{C_0}. \end{aligned} \quad (10)$$

In actual practice, by the aid of an impedance-meter (NOVO-CONTROL), we determined the characteristics of a capacitor with the Na-mordenite as dielectric by measuring its capacitance (C) and its conductance ($G = 1/R$), when it is submitted to a 0.5 V alternating electric field, whose angular frequency ranges from $6.28 \times 10^{-3} \text{ rad} \times \text{s}^{-1}$ to $6.28 \times 10^{+7} \text{ rad} \times \text{s}^{-1}$.

2.3. Gas Adsorption in Solids and the Dubinin Model

2.3.1. *Reminder of Some Modelling of Gas Adsorption on Some Solids.* As far back as 1916, Langmuir [14, 15] went through a model likely to account for a fully gaseous monomolecular layer adsorption on a solid surface, by assuming that the molecules making up this layer do not interact between them. This model was designed for interpreting the formation of the monolayer. This assumes that the evaporation rate (v_e) is proportional to the fraction ($\theta = N_a/N_0$) of the surface area covered at any given time by the adsorbed molecules, N_a being the number of adsorbing molecules or adsorbates fastened on the surface and N_0 the total number of the adsorption sites. The condensation rate (v_c) of the molecules on the surface is proportional to the surface not yet covered

($1 - \theta$) and the pressure P on the gas. At equilibrium, the condensation rate ($v_c = k_c \times P \times (1 - \theta)$) of the molecules on the surface is equal to the evaporation rate ($v_e = k_e \times \theta$) of the molecules from the surface, given with

$$k_c \times P \times (1 - \theta) = k_e \times \theta. \quad (11)$$

One can write

$$\frac{P}{N_a} = \frac{P}{N_0} + \frac{1}{K(T) \times N_0}. \quad (12)$$

Denoting by $K(T) = k_c/k_e$, equilibrium is constant. Thus, when one knows the surface covered by an adsorbing molecule, one can deduce from the Langmuir isotherms, corresponding to (12), the specific surface area of the adsorbent.

In 1938, Brunauer et al. [16] proposed a new model of the adsorption phenomenon, taking into account the formation of several molecule layers adsorbed and gas-gas interaction on the one hand and gas-solid ones on the other hand. They have got the following equation called BET equation, which enables a convenient representation of the adsorption isotherms to be obtained:

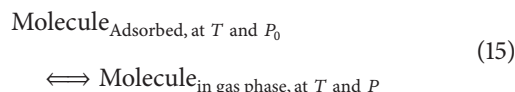
$$\frac{P}{(P - P_0) \times N_a} = \frac{1}{c \times N_0} + \left[\frac{c - 1}{c \times N_0} \times \frac{P}{P_0} \right], \quad (13)$$

where

$$c = \exp \left[\frac{E_1 - E_\ell}{R \times T} \right]. \quad (14)$$

The quantity c provides information on the affinity of the adsorbed molecules with the solid. The energy E_1 constitutes an estimate of the heat of adsorption by the prime layer, and energy E_ℓ is a measure of the adsorbate condensing heat, R is the universal gas constant, and T is the isotherm temperature. The graphic representation of (13), for the values of the ratio P/P_0 , such that $0.05 \leq P/P_0 \leq 0.3$, allows on the one hand the quantity c and on the other hand the specific area of the adsorbent to be determined.

In 1940, Dubinin, by analyzing a whole series of experimental results, contributed interestingly to describing the gaseous molecule adsorption phenomenon on microporous solids. He showed clearly a correlation by relating the amount of adsorbed gas to the energy involved in the molecule fixation mechanism on the surface. In cooperation with many other authors [17–22], he compared this energy to $-\Delta G$, ΔG being Gibbs free energy change of the transformation reaction from the adsorbed phase to the gaseous one, which is described by the following chemical equation:



Applying the laws of thermodynamics on equilibrium states, then one obtains

$$\begin{aligned} \Delta G + R \times T \times \text{Ln} \left[\frac{P}{P_0} \right] &= 0 \\ \text{hence } -\Delta G &= R \times T \times \text{Ln} \left[\frac{P}{P_0} \right]. \end{aligned} \quad (16)$$

For a given system of adsorbate-adsorbent, Dubinin showed that the graphic representation of the adsorption rate ($\theta = N_a/N_0$), as a function of P/P_0 , yields only one curve, referred to as a characteristic. In the case of a given solid, the characteristic curves of different adsorbates can be fitted upon each other by means of using a specific parameter (β) called affinity whose value is dependent upon the nature of the adsorbate. The value of an energy E_0 characterizing the structure of the solid and related to the width L of the pores existing on its surface is a measure of the adsorbent influence that is given with

$$L = \frac{10.8}{(E_0 - 11.4)}. \quad (17)$$

In 1947, Dubinin et al. [23, 24] put forward an equation allowing the description of the organic molecule adsorption on the activated carbons. Then, in 1971, Dubinin and Astakhov [25] expanded it and made it applicable to the other solids including the zeolite by adding an exponent η that characterizes the solid's heterogeneity given with

$$\begin{aligned} N_a &= N_0 \times \exp \left[- \left[\frac{(-\Delta G)}{\beta \times E_0} \right]^\eta \right] \\ &= N_0 \times \exp (-B \times (-\Delta G)^\eta). \end{aligned} \quad (18)$$

We must repeat that E_0 and B are characteristic quantities of the studied solid.

3. Measurement Method and Interpretation

3.1. Experimental Data and Analysis

3.1.1. Utilization of the Polarization Measurements. We reproduced the same hydration conditions and then placed a Na-mordenite sample, held for three hours at a treatment temperature (TT) at equilibrium, in a measuring cell of an impedance-meter (NOVOCONTROL). Then we observed the variations in the imaginary part of the dielectric permittivity (ϵ_r'') in relation to the angular frequency (ω) of the applied electric field (\vec{E}) and to the temperature (T) imposed on the sample. First of all, we ensure that the number of water molecules fastened on the sample does not increase by means of an external action whereby it is kept under an atmosphere in equilibrium with its hydration rate and that with the use of a device operating with a flow of perfectly dry argon. Thus we know that, under these conditions, a process wherein water moves can partake only if the sample undergoes an increase in temperature. Then, we imposed on it a temperature series, each of which was inferior to TT-10, for determining the activation energy of the polarization phenomenon. Complying with these requirements, we measured the imaginary part of the permittivity (ϵ_r''), according to the angular frequency (ω) of the applied electric field. As shown in Figure 3, we obtained a series of curves by drawing the variations in ϵ_r'' as a function of $\log(\omega/2\pi)$, at TT = 373 K and T varying from 323 K to 263 K.

Referring to the curves, we localized $\log(\omega_m/2\pi)$ corresponding to the abscissa of the maximum of ϵ_r'' . Based

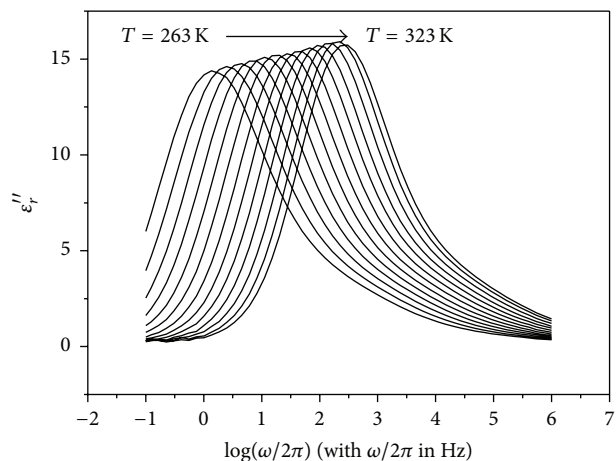


FIGURE 3: Loss factor ϵ_r'' in Na-mordenite of 5.5:1 Si/Al ratio (previously hydrated at the treatment temperature (TT)), as a function of $\log(\omega/2\pi)$ at each temperature T such that $T < TT - 10$ K.

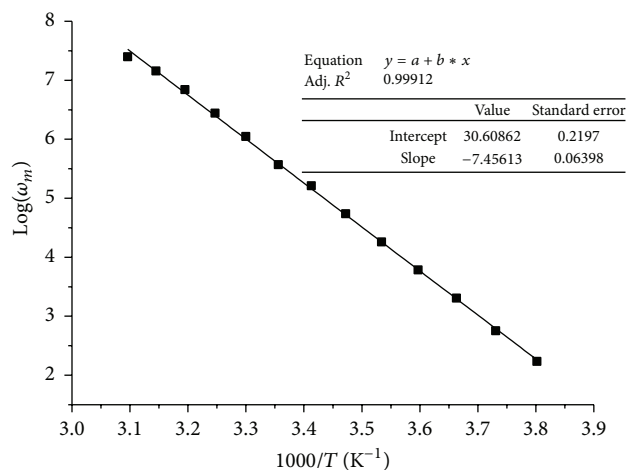


FIGURE 4: Using a Na-mordenite sample of 5.5:1 Si/Al ratio previously hydrated at the treatment temperature TT = 373 K, to ascertain experimentally the relationship $\text{Log}(\omega_m) = \text{Log}(1/\tau_0) - \Delta E_{\text{hop}}/(k \times T)$.

on (3), we know that this point (ϵ_r'' peak maximum) is characterized by the relationship $\omega_m \times \tau = 1$, whereof one derives straightforwardly $\tau = 1/\omega_m$, for each measuring temperature T . Then, one plots the values of $\text{Log}(1/\tau) = \text{Log}(\omega_m)$ thus obtained as a function of $1000/T$, where T is the temperature that was maintained constant throughout the determination of the curve: $\epsilon_r'' = f(\log(\omega/2\pi))$.

Then, one makes sure that the relationship (5) can be used while drawing the representative curve of $\text{Log}(1/\tau) = f(1000/T)$, and checking, as illustrated in Figure 4, that one actually obtains a straight line whose slope allows ΔE_{hop} to be determined from (6) [26–28].

The value of the activation energy (ΔE_{hop}) calculated from the slope of the straight line drawn, as shown in Figure 4, is $\Delta E_{\text{hop}} = 0.64$ eV for TT = 373 K. Thereafter we repeated the method that has just been described for

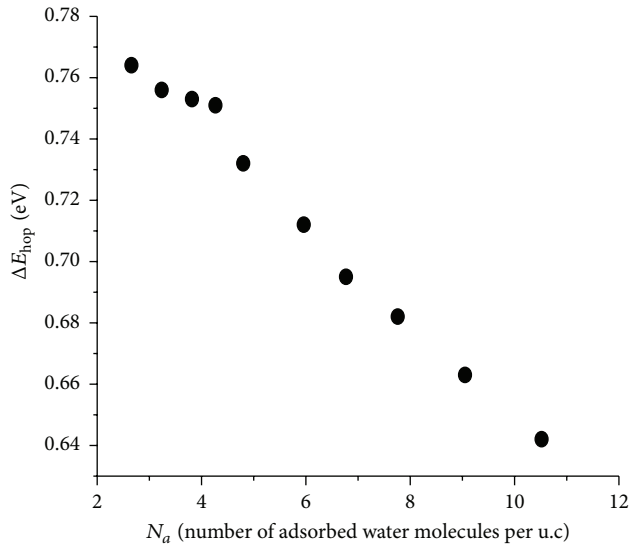
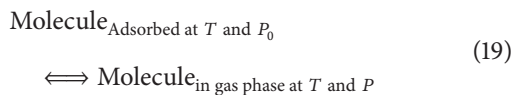


FIGURE 5: Change in the jumping energy (ΔE_{hop}) in a Na-mordenite of 5.5:1 Si/Al ratio as a function of the number (N_a) of adsorbed water molecules per unit cell (u.c).

determining the variations in the value of ΔE_{hop} , when the Na-mordenite sample of 5.5:1 Si/Al ratio is submitted to the treatment temperatures (TT) ranging from 333 K to 467 K. The output of the measurements by differential thermal analysis (DTA) we previously performed is given with Figure 5.

Thus we showed that each treatment temperature of the Na-mordenite of 5.5:1 Si/Al ratio corresponds to an amount of adsorbed water molecules per unit cell that we already denoted by N_a . Figure 5 illustrates the graph of the value of ΔE_{hop} as a function of the number (N_a) of adsorbed water molecules per unit cell of Na-mordenite of 5.5:1 Si/Al ratio.

3.2. Discussion. The adsorbed water molecules fastened on the Na-mordenite are in equilibrium with those in vapour phase, in contact with the solid. The laws obeyed by the mechanism of this equilibrium can be studied when regarding it as a pseudo reaction given with



The laws of thermodynamics of the equilibrium states enable one to write

$$-\Delta G = R \times T \times \text{Log} \left[\frac{P}{P_0} \right]. \quad (20)$$

Many authors including Dubinin et al. [29–35] assimilated the energy which sustains the mechanism fixing the molecules adsorbed on the surface to the opposite of Gibbs free energy change ($-\Delta G$) of the pseudo reaction. To interpret the observed behaviour, it is necessary to provide an estimate of the interaction energy between the adsorbed water molecules and the exchanged cations on the solid surface.

3.2.1. Making Use of a Lennard-Jones Potential to Describe the Interaction between a Compensation Cation and the Adsorbed Water Molecules. We assume that each interaction energy involved in the adsorption phenomena can be described by a Lennard-Jones potential [36–38]. By disregarding the term of repulsion whose influence is negligible in an adsorption process, we can write the relationship already suggested by Hasley, Hill, and Frenkel [39–41]:

$$u = \sum_j \left[\frac{\kappa}{r_j} \right]^n, \quad (21)$$

where u is the interaction energy between an adsorbed water molecule and the surface, r_j is the distance between the adsorbed molecule and an atom on the surface that interacts with it, κ is a constant, and n is an empirical exponent.

Then one considers the stage of the adsorption process where the number of the adsorbed water molecules is lower than that which makes it possible for the monolayer to be formed, that is to say less than 10 adsorbed water molecules per unit cell of Na-mordenite. Previous works have shown that these water molecules are distributed on the solid surface to form a latticework [42–44]. Denoting by r_{ww} the distance between two water molecules, by r_{kw} the distance between a sodium cation and its closest neighbouring water molecules, by N_a the number of adsorbed water molecules per unit cell of Na-mordenite, and by A_σ the solid's total surface accessible to the water molecules, one can write the two following equations:

$$A_\sigma = \alpha \times N_a \times r_{ww}^2, \quad (22)$$

$$r_{kw} = \beta \times r_{ww}, \quad (23)$$

where α and β are parameters that describe the lattice geometry. By combining (22) and (23), one derives

$$r_{kw} = \beta \times \sqrt{\frac{A_\sigma}{\alpha \times N_a}}. \quad (24)$$

Substituting the values of r_{kw} , obtained from (24), into (21), one can sum up the energies of a cation interaction with the adsorbed water molecules which are its closest neighbours. Thus one obtains an estimate of the variation in the energy (ΔE_{hop}) caused by the first adsorbed water molecules, implying that $N_a \leq 10$. We incorporated the expression of r_{kw} (24) into (21), and we obtained after due calculations the following expression of the variations in the jumping energy (ΔE_{hop}) under the effect of the N_a water molecule adsorption:

$$\Delta E_{\text{hop}}(N_a) = \Delta E_{\text{hop}}^0 - N_a \times \left[\frac{\kappa \times \sqrt{\alpha \times N_0}}{\beta \times \sqrt{A_\sigma}} \right]^n. \quad (25)$$

For greater convenience, we rearranged this equation as

$$\Delta E_{\text{hop}}(N_a) = \Delta E_{\text{hop}}^0 - B \times N_a. \quad (26)$$

In expression (26), ΔE_{hop}^0 stands for the cation extraction energy from its site under the conditions where the Na-mordenite sample is fully hydrated and B is a coefficient

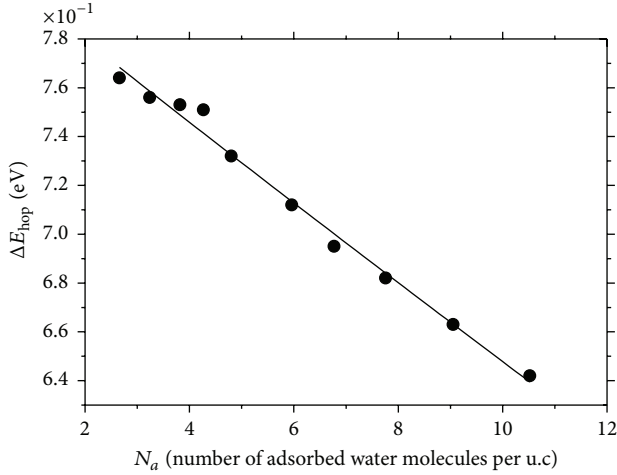


FIGURE 6: Fit between the curve schematizing the equation $\Delta E_{\text{hop}}(N_a) = \Delta E_{\text{hop}}^0 - B \times N_a$ and the plot of the experimental values of $\Delta E_{\text{hop}}(N_a)$ as a function of the number (N_a) of adsorbed water molecules per unit cell (u.c) of a Na-mordenite of 5.5 : 1 Si/Al ratio.

of variation. Then we used (26), and try to find out the change in the value of ΔE_{hop} according to the number (N_a) of adsorbed water molecules per unit cell of Na-mordenite of 5.5 : 1 Si/Al ratio. The result is shown in Figure 6 whereon one sees that (26) allows the observed adsorption behaviour to be interpreted properly.

This well fit between the curves enables us to determine the following values:

$$\begin{aligned} \Delta E_{\text{hop}}^0 &= 0.81 \text{ eV}, \\ B &= 0.0164 \text{ eV} \cdot \text{molécule}^{-1}. \end{aligned} \quad (27)$$

3.2.2. Making Use of Dubinin, Raduskevich, and Kaganer's Empirical Approach to Describe the Interaction between a Compensation Cation and the Adsorbed Water Molecules. The second aspect of the interpretation of the observed behaviours, based on the experimentally determined values of $\Delta E_{\text{hop}}(N_a)$ we plotted as a function of the number (N_a) of the adsorbed water molecules per unit cell of Na-mordenite of 5.5 : 1 Si/Al ratio, involves using the empirical approach suggested by Dubinin, Raduskevich, and Kaganer [29–32]. Indeed, these authors proposed an equation relating the ratio (N_a/N_0) and the energy that is involved in the process of the molecule fixation on the surface. The equation is written as follows:

$$\text{Log} \left[\frac{N_a}{N_0} \right] = -D_{\text{Dub}} \times u^2. \quad (28)$$

Assume that

$$u = R \times T \times \text{Log} \left[\frac{P}{P_0} \right]. \quad (29)$$

By using reasoning similar to that we developed in the previous section, we derive the following equation aiming at recovering the change in the value of ΔE_{hop} as a function of

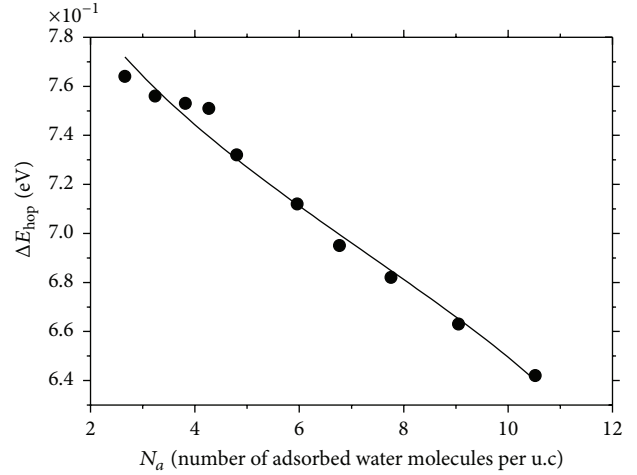


FIGURE 7: Comparison between the experimental plot of the variations in $\Delta E_{\text{hop}}(N_a)$ and the curve schematizing the equation $\Delta E_{\text{hop}}(N_a) = \Delta E_{\text{hop}}^T + \sqrt{([\text{Log}[N_0/N_a])/D_{\text{Dub}}]}$, elicited from the empirical approach of Dubinin.

the number (N_a) of water molecules adsorbed per unit cell of Na-mordenite of 5.5 : 1 Si/Al ratio:

$$\Delta E_{\text{hop}}(N_a) = \Delta E_{\text{hop}}^T + \sqrt{\left[\frac{\text{Log} [N_0/N_a]}{D_{\text{Dub}}} \right]}. \quad (30)$$

In that equation, ΔE_{hop}^T denotes the extraction energy of the compensation sodium cation from its site, under the conditions where the Na-mordenite surface is coated with a water molecule monolayer. It is shown in Figure 7 that the plot of the values of $\Delta E_{\text{hop}}(N_a)$ experimentally determined follows closely the shape of the curve schematizing $\Delta E_{\text{hop}}(N_a) = \Delta E_{\text{hop}}^T + \sqrt{([\text{Log}[N_0/N_a])/D_{\text{Dub}}]}$. Making that curve fit suitably upon the experimental plot then provides the following parameters:

$$\begin{aligned} \Delta E_{\text{hop}}^T &= 0.58 \text{ eV}, \\ D_{\text{Dub}} &= 41.3223 \text{ eV}^{-2} \end{aligned} \quad (31)$$

and $N_0 = 12.17$ water molecules per unit cell of Na-mordenite.

4. Conclusion

In this work, we carried out dielectric relaxation measurements to investigate experimentally the change in the jumping energy of the sodium cations in a Na-mordenite of 5.5 : 1 Si/Al ratio, according to the degree of advancement of the water molecule adsorption. We also suggested two types of interpretations to account for the behaviours we observed:

- (1) The first one issuing from the theory of Frenkel, Halsey, and Hill makes it possible to give an exact representation of the results we got experimentally. It allows determining the extraction energy of the sodium cations in a dehydrated zeolite.

- (2) The second one, based on the empirical approach suggested by Dubinin, Raduskevich, and Kaganer, also leads to a very satisfactory representation of the experimental results. An adequate handling of them provides an estimate of the extraction energy of the sodium cations in a zeolite when its surface is coated with a monolayer of adsorbing molecules and also an estimate of the number of the molecules that form the monolayer when the concerned molecules are those of water.

This paper suggests a new experimental approach that gives original information on elemental processes involved in the adsorption phenomenon enabling one to account quantitatively and in detail for the interactions between the solid surface, the compensating cations, and the molecules adsorbed onto the aluminosilicates characterized by the presence of pores wherein the exchangeable cations are trapped.

Conflict of Interests

The author declares that there is no conflict of interests regarding the publication of this paper.

Acknowledgments

The author would like very much to thank Professor J. C. Giuntini (Honorary Professor at University of Montpellier 2, France) and Professor F. Henn (Professor at University of Montpellier 2, France) for the Dielectric Relaxation Spectroscopy (DRS) facility and for their support.

References

- [1] W. J. Mortier, *Compilation of Extraframework Sites in Zeolites*, Butterworth, Guildford, UK, 1982.
- [2] E. Durand, *Electrostatique I: Les Distributions*, Masson, Paris, France, 1964.
- [3] P. Baudoux, *Précis D'électricité Fondamentale*, Presses Universitaires de Bruxelles, Eyrolles, Paris, France, 1970.
- [4] P. Debye, "Hochfrequenzverluste und molekulstruktur," *Physikalische Zeitschrift*, vol. 35, p. 101, 1934.
- [5] K. S. Cole and R. H. Cole, "Dispersion and absorption in dielectrics I. Alternating current characteristics," *The Journal of Chemical Physics*, vol. 9, no. 4, pp. 341–351, 1941.
- [6] C. J. F. Bottcher, *Theory of Electrical Polarisation*, Elsevier, Amsterdam, The Netherlands, 1973.
- [7] I. Prigogine and V. Mathot, "Application of the cell method to the statistical thermodynamics of solutions," *The Journal of Chemical Physics*, vol. 20, no. 1, pp. 49–57, 1952.
- [8] I. Prigogine and L. Saraga, "Sur la tension superficielle et le modèle cellulaire de l'état liquide," *The Journal of Chemical Physics*, vol. 195, pp. 399–407, 1952.
- [9] R. H. Fowler and E. A. Guggenheim, *Statistical Thermodynamics*, Cambridge University Press, Cambridge, UK, 1965.
- [10] F. Buet, J. C. Giuntini, F. Henn, and J. V. Zanchetta, "Microscopic considerations of the calculation of the polarization conductivity in ionically conducting glasses," *Philosophical Magazine Part B*, vol. 66, no. 1, pp. 77–88, 1992.
- [11] W. H. Meir and D. H. Olson, "Atlas of zeolite structure type," *Zeolites*, vol. 17, p. 152, 1996.
- [12] J. L. Schlenker, J. J. Pluth, and J. V. Smith, "Positions of cations and molecules in zeolites with the mordenite-type framework: VIII Dehydrated sodium-exchanged mordenite," *Materials Research Bulletin*, vol. 14, no. 6, pp. 751–758, 1979.
- [13] P. F. Barbara, T. J. Meyer, and M. A. Ratner, "Contemporary issues in electron transfer research," *The Journal of Physical Chemistry*, vol. 100, no. 31, pp. 13148–13168, 1996.
- [14] I. Langmuir, "The constitution and fundamental properties of solids and liquids. Part I. Solids," *The Journal of the American Chemical Society*, vol. 38, no. 2, pp. 2221–2295, 1916.
- [15] I. Langmuir, "The adsorption of gases on plane surfaces of glass, mica and platinum," *Journal of the American Chemical Society*, vol. 40, no. 9, pp. 1361–1403, 1918.
- [16] S. Brunauer, P. H. Emmett, and E. Teller, "Adsorption of gases in multimolecular layers," *Journal of the American Chemical Society*, vol. 60, no. 2, pp. 309–319, 1938.
- [17] M. Polanyi, "On adsorption from the standpoint of the third law of thermodynamics," *Verhandlungen der Deutschen Physikalischen Gesellschaft*, vol. 16, pp. 1012–1016, 1914.
- [18] M. Polanyi, "Adsorption of gases by a solid non-volatile adsorbent," *Verhandlungen der Deutschen Physikalischen Gesellschaft*, vol. 18, pp. 55–80, 1916.
- [19] M. Polanyi, "On adsorption and the origin of adsorption forces," *Zeitschrift für Elektrochemie*, vol. 26, pp. 370–374, 1920.
- [20] M. Polanyi, "Adsorption from solutions of substances of limited solubility," *Zeitschrift für Physik*, vol. 2, pp. 111–116, 1920.
- [21] L. Berenyi, "Proof of Polanyi's theory of adsorption," *Zeitschrift für Physikalische Chemie*, vol. 94, pp. 628–662, 1920.
- [22] L. Berenyi, "Modern adsorption calculations," *Zeitschrift für Physikalische Chemie*, vol. 105, pp. 55–72, 1923.
- [23] M. M. Dubinin, E. D. Zaverina, and L. V. Radushkevich, "Sorption and structure of active carbons. I. Adsorption of organic vapors," *Zhurnal Fizicheskoi Khimii*, vol. 21, pp. 1351–1362, 1947.
- [24] M. M. Dubinin, "Fundamentals of the theory of adsorption in micropores of carbon adsorbents: characteristics of their adsorption properties and microporous structures," *Carbon*, vol. 27, no. 3, pp. 457–467, 1989.
- [25] M. M. Dubinin and V. A. Astakhov, "Development of the concepts of volume filling of micropores in the adsorption of gases and vapors by microporous adsorbents," *Izvestiya Akademii Nauk SSSR*, vol. 11, p. 5, 1971.
- [26] S. Devautour, J. Vanderschueren, J. C. Giuntini, F. Henn, J. V. Zanchetta, and J. L. Ginoux, "Na⁺/mordenite interaction energy by thermally stimulated depolarization current," *The Journal of Physical Chemistry B*, vol. 102, no. 19, pp. 3749–3753, 1998.
- [27] J. C. Giuntini, G. Maurin, S. Devautour, F. Henn, and J. V. Zanchetta, "Experimental evidence of polarization effects on exchangeable cations trapped in zeolites," *Journal of Chemical Physics*, vol. 113, no. 11, pp. 4498–4500, 2000.
- [28] J. C. Giuntini, V. Mouton, J. V. Zanchetta, J. M. Douillard, J. Niezette, and J. Vanderschueren, "A simple general relationship between the dielectric losses measured on divided solids and adsorption thermodynamic," *Langmuir*, vol. 13, no. 5, pp. 1016–1019, 1997.
- [29] M. M. Dubinin and I. V. Radushkevich, "Equation of the characteristic curve of activated charcoal," *Proceedings of the Academy of Sciences of the USSR, Physical Chemistry Section*, vol. 55, pp. 331–337, 1947.

- [30] M. G. Kaganer, "A method for the determination of specific surfaces from the adsorption of gases," *Proceeding of the USSR Academy of Sciences*, vol. 116, pp. 603–605, 1957.
- [31] M. M. Dubinin and V. A. Astakhov, "Description of adsorption equilibria of vapors on zeolites over wide ranges of temperature and pressure," in *Molecular Sieve Zeolites-II*, vol. 102 of *Advances in Chemistry*, pp. 69–85, American Chemical Society, 1970.
- [32] J. P. Hobson and R. A. Armstrong, "A study of physical adsorption at very low pressures using ultrahigh vacuum techniques," *Journal of Physical Chemistry*, vol. 67, no. 10, pp. 2000–2008, 1963.
- [33] J. P. Hobson, "First adsorbed layer of Helium at 4.2°K," *Canadian Journal of Physics*, vol. 37, pp. 300–312, 1959.
- [34] N. Endow and R. A. Pasternak, "Physisorption of Xe and Kr on glass and molybdenum," *Journal of Vacuum Science & Technology*, vol. 3, pp. 196–201, 1966.
- [35] D. M. Young and A. D. Crowel, *Physical Adsorption of Gases*, Butterworths and Co, London, UK, 1962.
- [36] J. M. Cases, I. Bérend, G. Besson et al., "Mechanism of adsorption and desorption of water vapor by homoionic montmorillonite. 1. The sodium-exchanged form," *Langmuir*, vol. 8, no. 11, pp. 2730–2739, 1992.
- [37] I. Bérend, J.-M. Cases, M. François et al., "Mechanism of adsorption and desorption of water vapor by homoionic montmorillonites: 2. The Li⁺, Na⁺, K⁺, Rb⁺ and the Cs⁺ exchanged form," *Clays and Clay Minerals*, vol. 43, no. 3, pp. 324–336, 1995.
- [38] J. M. Cases, M. François, J. P. Uriot, L. J. Michot, I. Bérend, and F. Thomas, "Mechanism of adsorption and desorption of water vapor by homoionic montmorillonite: 3. The Mg²⁺, Ca²⁺, Sr²⁺ and Ba²⁺ exchanged forms," *Clays and Clay Minerals*, vol. 45, no. 1, pp. 8–22, 1997.
- [39] G. Halsey, "Physical adsorption on non-uniform surfaces," *The Journal of Chemical Physics*, vol. 16, no. 10, pp. 931–937, 1948.
- [40] T. L. Hill, "Theory of physical adsorption," *Advances in Catalysis*, vol. 4, pp. 211–258, 1952.
- [41] J. Frenkel, *Kinetic Theory of Liquids*, Clarendon Press, Oxford, UK, 1946.
- [42] J. D. Russel, V. C. Farmer, and B. Velde, "Replacement of OH by OD in layer silicates, and identification of the vibrations of these groups in infra-red spectra," *Mineralogical Magazine*, vol. 37, no. 292, pp. 869–879, 1970.
- [43] J. Mamy, *Recherches sur l'hydratation de la Montmorillonite: propriétés diélectriques et structure du film d'eau [Ph.D. thesis]*, Paris, France, 1968.
- [44] G. J. Rosasco and J. J. Blaha, "Raman microprobe spectra and vibrational mode assignments of talc," *Applied Spectroscopy*, vol. 34, no. 2, pp. 140–144, 1980.

Review Article

Novel Mesoporous Silica Materials with Hierarchically Ordered Nanochannel: Synthesis with the Assistance of Straight-Chain Alkanes and Application

Haidong Zhang¹ and Xiaohong Li²

¹Engineering Research Centre for Wasted Oil Recovery Technology of Ministry of Education, Key Laboratory of Catalysis Science and Technology of Chongqing Education Commission, Chongqing Technology and Business University, Chongqing 400067, China

²Shanghai Key Lab of Green Chemistry and Chemical Processes, School of Chemistry and Molecular Engineering, East China Normal University, Shanghai 200062, China

Correspondence should be addressed to Haidong Zhang; haidongzhang@ctbu.edu.cn and Xiaohong Li; xhli@chem.ecnu.edu.cn

Received 2 October 2015; Accepted 22 December 2015

Academic Editor: Khaldoun Bachari

Copyright © 2016 H. Zhang and X. Li. This is an open access article distributed under the Creative Commons Attribution License, which permits unrestricted use, distribution, and reproduction in any medium, provided the original work is properly cited.

The straight-chain alkane-assisted synthesis of hierarchical mesoporous silica materials (MSM) results in variable mesostructures and morphologies due to remarkably different self-assembly routes of template agent from those without the assistance of straight-chain alkanes. The textural properties, particularly pore size, channel structure, morphology, and hierarchical structure of those MSM make them demonstrate peculiar effects in the immobilization of homogeneous catalysts.

Dedicated to Professor Yi-Meng Wang

1. Introduction

In the past two decades, ordered MSM have received much attention due to their tunable mesostructure, systematically tailored pore architecture, and their applications in adsorption, separation, catalysis, drug delivery, photonic, and nano-sized semiconductors [1–8]. The preparation of MSM is based on the use of structure-directing agents, which are normally organic molecules or supramolecules of surfactants and polymers, for example, EO₂₀PO₇₀EO₂₀ (Pluronic P123) for SBA-15 type MSM [9, 10], Pluronic F127 for SBA-16 type MSM [11], cetyltrimethylammonium bromide (C₁₆H₃₃N(CH₃)₃-Br, CTAB) for MCM-41 [3–5, 12] and MCM-48 [13, 14] types MSM, and biodegradable polyethylene oxide (PEO) surfactants for MSU-X type MSM [15–18]. Besides these supramolecules and polymers, some other materials like resin [19] and DNA [20] can also be used to prepare MSM. Particularly, the SBA-15 type MSM have attracted extraordinarily high

attention because of their large pore size ranging from 4.6 to 30 nm, uniform ordered mesoporous channels, high specific surface area, connectivity of the mesoporous channels, and higher hydrothermal stability than some other MSM [1, 9, 10, 21, 22].

In the preparation of MSM, the methods to tune the porosity, pore morphology, size distribution, and the hierarchical morphology of these materials are of particular interests. According to current knowledge, cooperative assembly between template molecules and silica precursors is generally involved to form mesostructured organic/inorganic composites during the preparation of MSM. The mesostructure can be maintained after removal of template. In other words, the formation of the ordered mesopores, specific morphology, and textural characteristics of final products is decided by the nanostructure of the self-assembled hybrid micelles of organic template molecules and inorganic framework species. The factors including hydrolysis and condensation of silicate

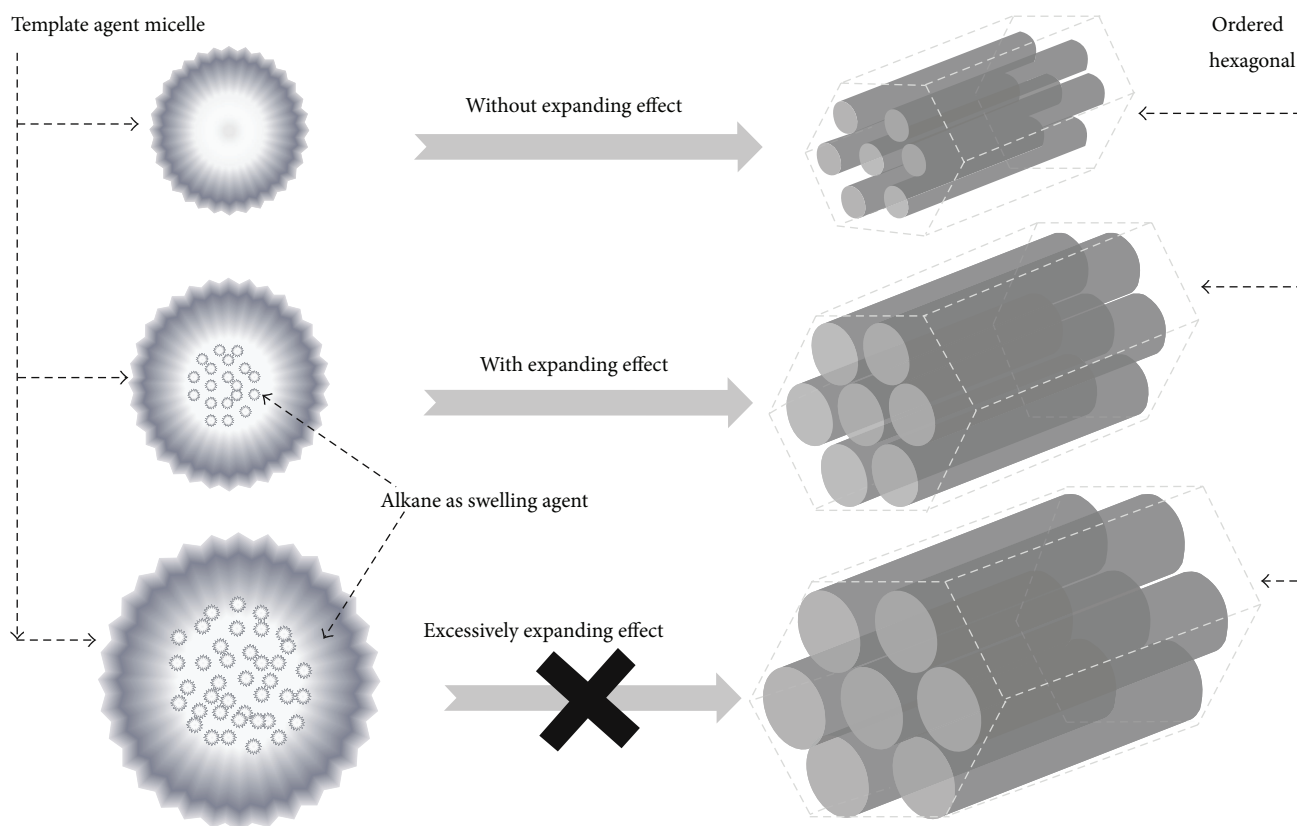


FIGURE 1: Tuning the pore size of ordered MSM with alkanes as swelling agents.

species, the shape of micelles, inorganic salts, organic swelling agents, cosolvents, and cosurfactants are found to affect the morphology of final products [21, 23–27].

One important finding in this field is that the addition of some pore expanders, for example, alkanes and aromatics, into the synthetic mixtures can greatly change the mesostructure and specific morphology of final products [28]. These pore expanders, for example, 1,3,5-trimethylbenzene (TMB) [9, 10, 29–32], ethylbenzene [33], decane [31, 34–36], hexane [37–39], heptane [30, 37], nonane [37], 1,3,5-triisopropylbenzene (TIPB)/cyclohexane [40–42], octane [43], and *N,N*-dimethylhexadecylamine [44], act as swelling agents and lead to enlarged micelle size of templates and subsequently enlarged pore size as illustrated in Figure 1. In novel gemini surfactant system, decane was also employed to tune the pore size and mesostructure of MSM [45]. However, the pore expanding agents typically result in a decrease in mesostructure ordering and even a dramatic change in the type of mesostructure (e.g., from hexagonally ordered SBA-15 to mesocellular foam) while they readily increase the pore size and volume of micelle-templated materials [28]. In some cases, those swelling agents can remarkably change the particle morphology of obtained ordered MSM. While those micelle expanders, which show the excessively strong and thus poorly controlled swelling behavior, were used, it is hardly to simply enlarge the pore size without any changes in morphology, ordering, and type of mesostructure.

In this minireview paper, we focus on the effect of the addition of straight-chain alkanes in the syntheses processes of ordered MSM on their textural characteristics and specific morphology. The applications of these mesoporous silica materials prepared with the assistance of straight-chain alkanes in the fields such as catalysis, separation, and drug delivery are also presented.

2. Straight-Chain Alkane-Assisted Synthesis of Mesoporous Silica

2.1. Synthesis without Phase Separation

2.1.1. Pore Expanding Effect of Alkanes. The employment of various organic molecules as swelling agents to expand the pore size of mesoporous silica materials has a history almost as long as that of MSM themselves [3, 46]. In most cases, TMB was used as a competent swelling agent for the pore expansion of two major families of MSM, MCM-41 [3, 46] and SBA-15 [9, 10], due to the hydrophobic interactions of its aromatic structure with template molecules. With the assistance of inorganic salt, TMB and P123 could be employed to synthesize highly ordered face-centered cubic (fcc) LP-FDU-12 MSM with large pores (up to 27 nm) and unit cells (up to 44 nm) at low temperatures [47].

Ulagappan and Rao used straight-chain alkanes (C_nH_{2n+2} , $n = 5$ to 20) as swelling agents in the pore expansion of

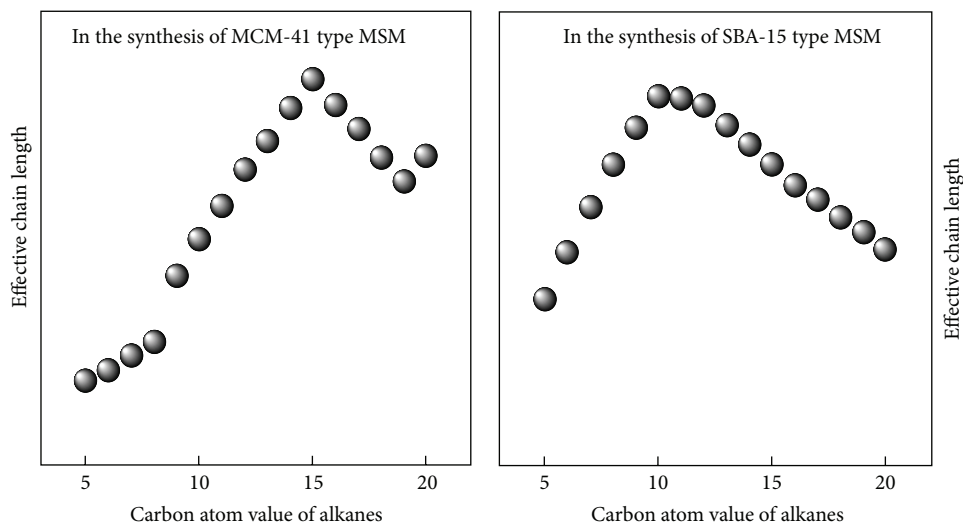


FIGURE 2: Effective chain length of n -alkanes as swelling agent [34, 37, 43, 48, 50, 51, 55, 56].

the MSM templated by CTAB [48]. They found that the alkanes with $n = 9$ to 15 showed best behavior towards the pore expansion in mesoporous silicas, where the increase in d_{100} is close to the theoretic chain length of those alkanes. They suggested that a core of alkanes with $n = 9$ to 15 is surrounded by a layer of surfactant CTAB, with a one-to-one alignment of the alkane chain and the surfactant tail. In case of the alkanes with $n = 5$ to 8, small increases in the d_{100} value were observed, compared to the entire chain length of the alkanes. Differently, the alkanes with $n = 5$ to 8 may be dispersed between the tails of the surfactant molecules, and thus the entire chain length of the alkanes is not involved in enlarging the size of the surfactant micelles. Higher alkanes with $n > 15$ also cannot result in significant pore expansion, suggesting that these chains may not be rigid enough and thus contribute less to pore expanding than those with n from 9 to 15. Conversely, in the synthesis of SBA-15 type MSM, a decrease in the alkane chain length from 12 to 6 carbon atoms led to a unit-cell size enlargement from 13 to 16–17 nm and pore diameter increasing from 12 to 16 nm [37, 51]. This is consistent with the findings of Nagarajan; that is, the uptake of linear alkanes by micelles of Pluronic copolymers was rather small and it increases as alkanes chain length decreases [54].

Jana et al. investigated the pore expanding effect of some linear alkanes including octane, nonane, decane, tridecane, hexadecane, and eicosane in the synthesis of SBA-15 type materials [50]. They used a triblock copolymer [poly(ethylene glycol)₂₀-poly(propylene glycol)₇₀-poly(ethylene glycol)₂₀] (Dai-ichi Kogyo Seiyaku, Japan) as the substitute for P123. Being different to some other studies [9, 10], they did not add the triblock copolymer into HCl solution but into deionized water to form a template-H₂O solution, followed by the addition of TEOS and HCl, step by step. They found that the use of octane and nonane could only lead to the formation of disordered MCF but the use of decane, tridecane, hexadecane, and eicosane could result in ordered hexagonal mesostructure of SBA-15 type MSM. The pore size of obtained

MSM is increased to 22.7 nm in the presence of octane (C₈H₁₈), whereas it is increased to 8.4, 8.5, 8.8, 10.1, and 14.0 nm in the presence of hexadecane (C₁₆H₃₄), tridecane (C₁₃H₂₈), eicosane (C₂₀H₄₂), decane (C₁₀H₂₂), and nonane (C₉H₂₀), respectively. This generally reflects that longer chain length of alkane leads to smaller pore diameter of resultant SBA-15 materials, but such trend is not linear and the reason for this gradual decrease had not been discussed. Actually, their finding is materially consistent with that discovered by Ulagappan and Rao [48] in the synthesis of MCM-41 type MSM and that discovered by Sun et al. [37] and Zhang et al. [51] in the synthesis of SBA-15 type MSM.

These findings suggest that the effective chain length of n -alkane should be considered while employed as swelling agent in the synthesis of MSM (see Figure 2) [34, 37, 43, 48, 50, 51, 55, 56]. In the synthesis of SBA-15 type mesoporous silicas with P123 as template agent, the effective chain length almost increases linearly with increasing n value and thus the corresponding expanding effect also increases linearly for those n -alkanes (C _{n} H_{2 n +2}) with $n = 5$ to 9. The effective chain length of the n -alkanes with $n = 10$ to 15 does not increase but decrease with n value and longer alkane leads to smaller pore diameter. In the synthesis of MCM-41 type MSM using CTAB as template, the effective chain length increases linearly with n value for those n -alkanes (C _{n} H_{2 n +2}) with $n = 9$ to 15 and C15H32 shows the highest effective chain length. In the synthesis of Ti-HMS molecular sieve with n -hexane and n -octane as pore expanders [57], it was also found that the pore diameter of Ti-HMS increased with the increase in the dosage of alkanes and the number of carbon atoms in alkane molecules.

2.1.2. Effect of Alkanes on Morphology. The alkanes used as swelling agent in the synthesis of MSM can lead to not only the expanded pore diameter but also the lowering of the degree of structural ordering and further change of the structure type [28]. In the studies of Ulagappan and Rao on

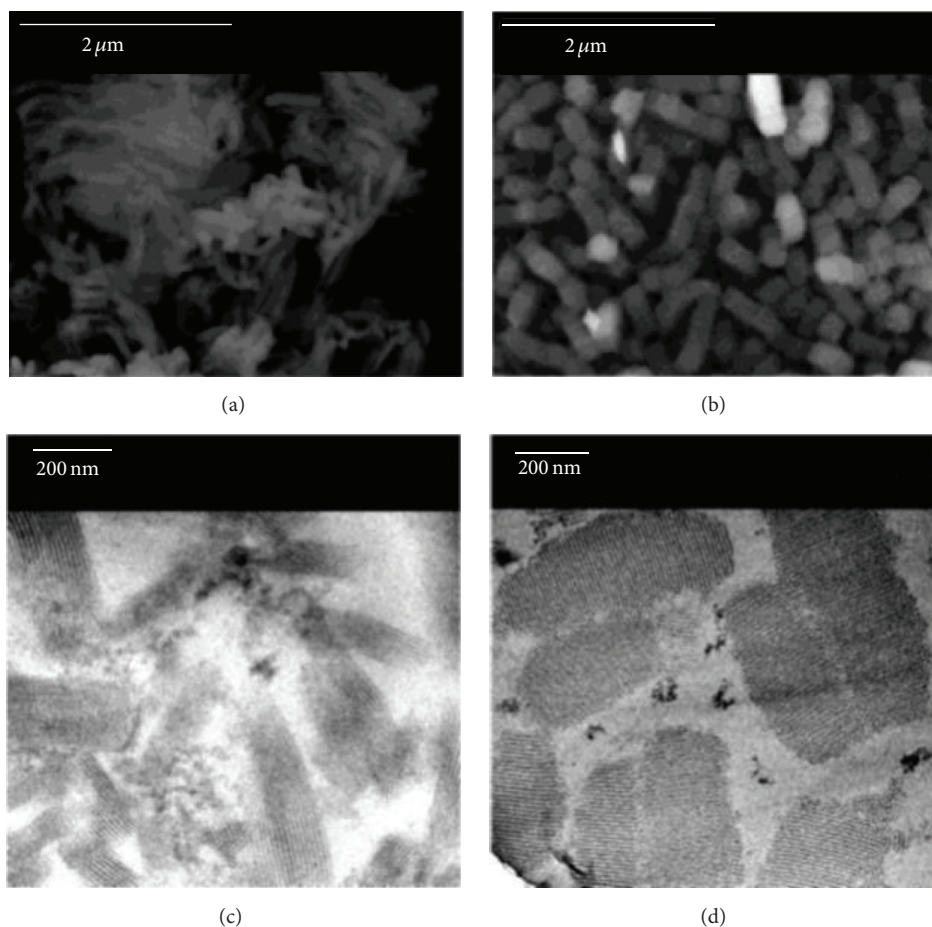


FIGURE 3: SEM images (a-b) and TEM images (c-d) of mesoporous silica SBA-15 synthesized at different weight ratios of decane to P123 in the presence of NH_4F : (a) and (c) 0.4 : 1; (b) and (d) 5.8 : 1. Reprinted with permission from [34]. Copyright (2004) American Chemical Society.

the effect of different *n*-alkanes on the synthesis of MCM-41 type MSM, the disordering or variability of mesostructure was observed with the addition of *n*-alkanes [48]. Jana et al. also found that the use of decane, tridecane, hexadecane, and eicosane could result in ordered hexagonal mesostructure of SBA-15 type MSM but the use of octane and nonane could not [50].

Zhang et al. reported for the first time the use of *n*-decane as the swelling agent in the preparation of a novel type of mesoporous SBA-15 material with unconventional short channels running along the short axis of particles [34]. They used large amount of *n*-decane (with a typical weight ratio of decane to P123 at 5.8 : 1) as cosolvent to synthesize unusual SBA-15 material with cuboid-like morphology and large pore size. The average pore size of this SBA-15 material is around 12.1 nm, which is remarkably larger than that of classic SBA-15 materials, due to the foreseeable expanding effect of *n*-decane [9, 10]. More interestingly, the channel length of this SBA-15 material is decided by the size of these cubo-like particles, which are about 500 nm long and 200 nm wide (see Figure 3). The ratio of *n*-decane to P123 was suggested to be the key point that affects the mesostructure of final products. Low ratio of decane to P123 at 0.4 : 1 showed unapparent

effect on the morphology of the obtained SBA-15 material, which is fiber-like and similar to the classic SBA-15 materials. While the decane/P123 ratio increases to 5.8 : 1, the change of morphology from fiber-like to cubo-like takes place. Further increase of decane/P123 ratio to 7.6 : 1 leads to no further expanding of pore size and its effect on morphology and mesostructure of nanochannels was not mentioned.

TMB/P123 weight ratio should be kept less than 0.3 : 1 to obtain hexagonally ordered SBA-15 materials while TMB is used as a swelling agent [29]. The TMB/P123 weight ratio higher than 0.3 : 1 will lead to disordered mesocellular foam (MCF). Although Zhang et al. mentioned that the amount of *n*-decane used in their preparation was probably enough to form microemulsion, no phase transition was observed when their synthesis process was carried out in a homogeneous mixture of P123- H_2O -decane. They suggested a side-on mechanism (see Figure 4) of condensation between short silicate-doped micelles, similar to the mechanism suggested by Ulagappan and Rao [48]. In such condensation mechanism, *n*-decane in the micelles of P123 acts as swelling agent and then expands the pore diameter. However, the driving force to speculate formation of such novel cubo-like morphology was still indistinct.

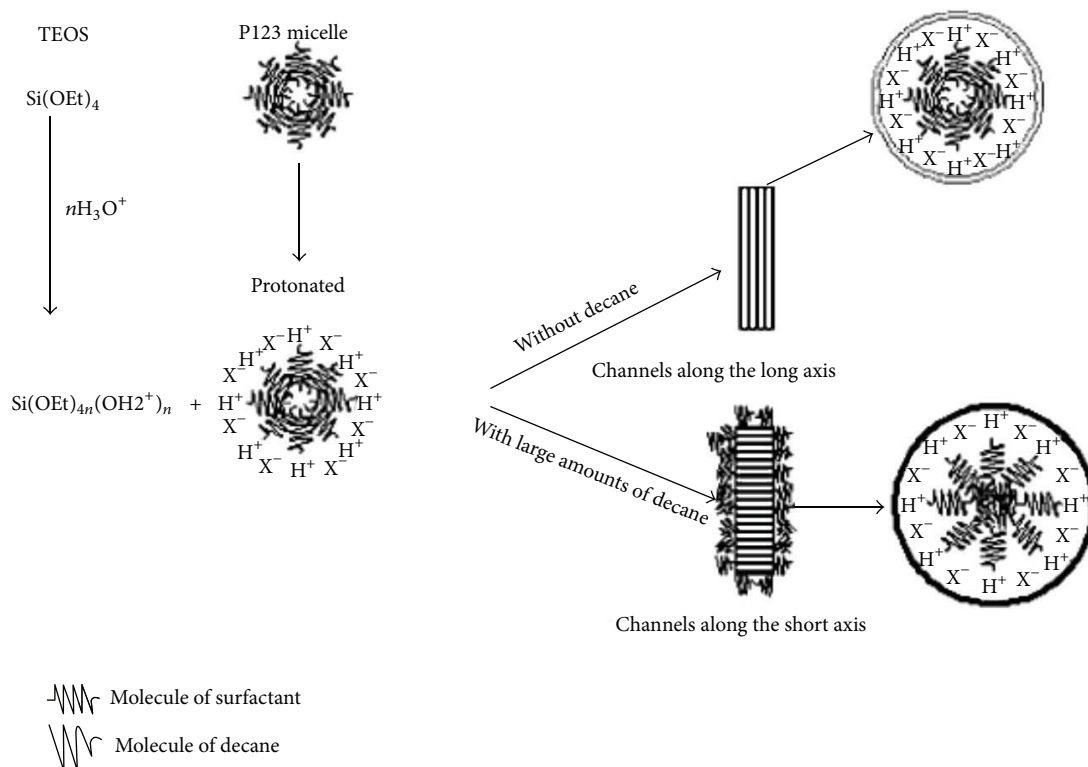


FIGURE 4: Schematic representation of the bifunctional roles of large amounts of decane. Reprinted with permission from [34]. Copyright (2004) American Chemical Society.

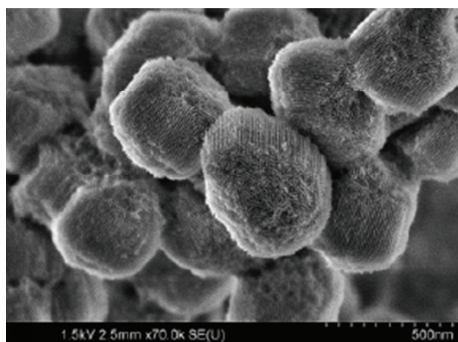


FIGURE 5: HRSEM image of the SBA-15 mesoporous silica resulting from the use of decane. Reprinted with permission from [51]. Copyright (2006) American Chemical Society.

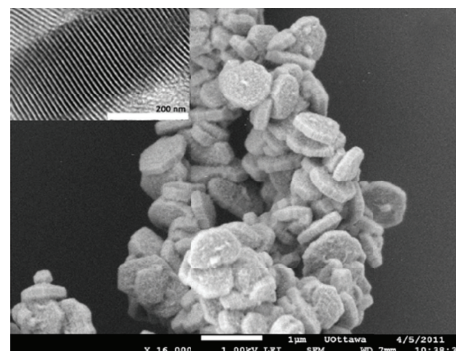


FIGURE 6: SEM image of the platelet-like SBA-15 mesoporous silica resulting from the use of decane. Reprinted with permission from [61]. Copyright (2011) American Chemical Society.

Actually, the TEM image of this SBA-15 with short channels looks more like the cross section [51] of a platelet-like [58, 59] or a short rod-like [60] SBA-15 materials, as short nanochannels (100–300 nm long) could run parallel to the thickness of the nanostructured hexagonal platelet-like or rod-like particles. The high-resolution TEM (HRTEM) image of such SBA-15 sample prepared with a decane/P123 ratio at 5.8:1 intensifies such hypothesis [34]. The further studies on the effect of *n*-decane indicated that such abovementioned short channel SBA-15 silica might also be a tower/platelet-like SBA-15 silica (see Figure 5) [51]. Additionally, the repetition of

the same synthetic process by other researchers indicated that this synthetic system leads to platelet-like SBA-15 type silica (see Figure 6) [61].

Low decane/P123 ratio can also distinctly affect the morphology and ordering of resultant product, reflecting the perturbation effect of *n*-decane on the self-assembly of P123 micelles [34]. Although the pore size related to decane/P123 ratio at 0.4:1 was not provided, the obtained fiber-like SBA-15 materials was remarkably shorter and thinner than classic SBA-15 materials. This is agreed with the findings of Ulagappan and Rao [48].

Secondly, the addition of NH_4F was considered as a crucial factor for the formation of highly ordered hexagonal mesoporous structure, while only disordered MSM can be obtained without the addition of NH_4F [34]. F^- , as a mineralizing agent, is commonly used in the synthesis of zeolite and some mesoporous materials. Fluoride not only accelerates hydrolysis and polymerization of silica species, but also increases the solubility of certain tri- and tetravalent elements through complexation, allowing well mineralization as well as substantial ordering and significant improvement in mesostructure and macromorphology in aqueous acid media.

Sun et al. [37, 43, 56] and Zhang et al. [51] systematically studied the effect of the addition of some different straight-chain alkanes ($n\text{-C}_n\text{H}_{2n+2}$) on the mesostructure and morphology control of MSM, with carbon number $n = 5$ (pentane), 6 (hexane), 7 (heptane), 8 (octane), 9 (nonane), 10 (decane), 11 (undecane), and 12 (dodecane). Two major modifications to the syntheses were made [37, 43, 51, 56], comparing with the abovementioned synthesis of SBA-15 type mesoporous silica with the assistance of decane [34]. The first one is the way to add alkanes into reaction mixture. In the report [34], decane was firstly added into a clear solution of P123-HCl- H_2O , followed by the addition of NH_4F and tetramethoxyorthosilane (TMOS) in sequence. In their follow-up studies, hexane [37, 51, 55], heptane [37, 55, 56], octane [51, 55, 56], nonane [37, 51, 55, 56], decane [51, 55, 56], undecane [55], and dodecane [51, 55, 56], alkanes, and TEOS were premixed and then added into the clear solution of P123 in HCl. The second modification was the concentration of HCl solution used in the synthesis, which was increased from 1.07 M [34] to 1.20–1.30 M [37, 43, 51, 56]. Noticeably, the molar ratios of template to alkanes in the studies of Sun et al. [37, 43, 56], Sun et al. [56], and Ulagappan and Rao [48] were distinctly different. Ulagappan and Rao kept the molar ratio of template to alkane at 1 : 1 since this ratio was optimal for obtaining the maximum possible pore size with a given alkane just as in the case of TMB [46]. Sun et al. [37, 55, 56] and Zhang et al. [51] took the molar ratio of template to alkane ranging from 134 : 1 to 755 : 1. These synthesis processes were all based on the cooperation of straight-chain alkanes and micelles of P123 in homogeneous phase. It was strange that the formation of any microemulsion/emulsion had not been observed during these synthesis processes [34, 37, 43, 51, 56], because the formation of O/W microemulsion/emulsion is reasonable or even inevitable with such high molar ratio of surfactant to alkane [62–66].

Because of the two major modifications mentioned above, no such novel short channels as those parallel channels running along the short axis [34] can be observed in the synthesis processes assisted by the straight-chain alkanes with relatively short chain length [37]. Hexane (C_6H_{14}), heptane (C_7H_{14}), and nonane (C_9H_{20}) were used as swelling agents in the synthesis of highly ordered SBA-15 materials with the help of NH_4F and exhibited an increasing ability to expand the pore size of SBA-15 silica with a decrease in chain length of these three alkanes [37]. The largest pore size (15.7 nm) of SBA-15 silica was achieved with the addition of hexane, which has the shortest chain length among these three alkanes.

The specific area of the obtained SBA-15 silica is inversely proportional to pore size. Shorter chain length of alkane results in lower specific area and larger pore size. Notably, the effect of hexane, heptane, and nonane on the pore size of SBA-15 type mesoporous silica is opposed to that found in the synthesis of MCM-41 type mesoporous silica with CTAB [48].

In addition, the initial reaction temperature of hydrolysis was found to be a key point to form hexagonally ordered mesostructure. For each alkane among hexane, heptane, and nonane, a critical temperature was found to lead to the phase transition from hexagonally ordered mesostructure to disordered MCF type mesostructure [37]. Such critical temperature was found to be 17°C, 22°C, and 27°C for hexane, heptane, and nonane, respectively. The initial reaction temperature of hydrolysis must be lower than these critical ones to form highly hexagonally ordered mesostructure. Similar request of low reaction temperature was also found in the synthesis of SBA-15 type mesoporous silica with 1,3,5-triisopropylbenzene (TIPB) as a micelle expander [58]. Cao and Kruk used *n*-hexane as swelling agent and low temperature (15°C) of initial synthesis condition, similar to that of Sun et al. [37], to obtain highly ordered SBA-15 silica materials with pore diameters ranging from 12 to 18 nm [67]. Sun et al. studied the effect of chain length of straight-chain alkanes ($n = 6\text{--}12$) on the pore enlargement [55]. With or without alkane addition, the phase of surfactant micelle evolves in a way of amorphous \rightarrow hexagonal \rightarrow vesicle-like/hexagonal \rightarrow vesicle-like \rightarrow vesicle-like/foam-like \rightarrow foam-like with increasing temperature of initial synthesis. The phase-transformation temperature is linearly proportional to carbon number, where the optimized temperature of initial synthesis for achieving highly hexagonally ordered mesostructure increases with chain length of alkanes. Notably, the presence of vesicle-like mesostructure indicates the formation of *n*-alkane-P123- H_3O^+ microemulsion system in this study.

Different mesostructure of MSM can be varied by careful control over the phase behavior of water-alkane-surfactant synthetic mixture. The effect of alkane/surfactant ratio and TEOS/P123 ratio on the phase evolution in water-alkane-surfactant mixture was synergistically studied by Sun et al. [56] and Zhang et al. [51]. With the decane/P123 molar ratio increasing from 134 : 1 to 755 : 1, the obtained SBA-15 materials evolve from chain-like arrays of independent particles to loosely stacked independent particles and finally to a lamina-like aggregate of independent particles. All these independent particles of SBA-15 materials are highly ordered with a 2D hexagonal symmetry (p6mm) and exhibit the morphology similar to that of tower-like SBA-15 [49]. The proposed formation route [51] of these SBA-15 materials is a reprint of the one proposed for the formation of tower-like SBA-15 materials [49].

The effect of different TEOS/P123 molar ratio with a fixed decane/P123 molar ratio at 235 was also investigated [51]. With increasing TEOS/P123 molar ratio from 48 to 110, the obtained SBA-15 materials show 2D hexagonal symmetry (p6mm) but the morphology varies from fiber-like bundle (TEOS/P123 = 48 : 1) to loosely stacked independent particles (TEOS/P123 = 60 : 1), platelet-like particles (TEOS/P123 = 77 : 1), and free-standing films (TEOS/P123 = 110 : 1). Notably,

while TEOS/P123 molar ratio reaches 110 : 1, the yield of such free-standing films was around 50%, and some aggregated irregular particles were also observed besides these independent films. Similarly, a decrease in the ordering of MSM can also occur while the alkane/P123 molar ratio reaches a high value [68]. In the synthesis of SBA-15 with addition of heptane, the obtained material shows the morphology that consisted of both silica sheets and coarse silica foam [68].

In the abovementioned synthesis of MSM with the addition of straight-chain alkanes, highly ordered mesostructure with 2D hexagonal symmetry ($p6mm$), is common. However, one exception with the use of octane as swelling agent was also reported [43]. The octane-P123-water synthetic system results in novel silica particles in size of 100–200 nm long and 50–80 nm wide. Each particle contains some silica nanotubes arranged parallel in the way close to the minimum requirement for hexagonal structures. The pore size of such silica particles is around 13 nm due to the swelling effect of octane in P123 micelles. No possible route of the formation of such mesoporous silica material was proposed.

Hexane, octane, decane, dodecane, and hexadecane were used as pore-expanding agents in the synthetic system of alkan-ethanol-CTAB-water- NH_4OH [69]. The pore size can range from 2.5 to 6.0 nm, while decane was found to be the most effective pore expander [69]. Due to very low concentration of alkane in this synthetic system, different straight-chain alkanes did not result in much different morphology of obtained mesoporous silica materials. All these mesoporous silica materials consist of independent nanoparticles in the size of the range from 40 nm to 100 nm with irregular shape. The addition of alkane also results in some loss of the order of mesoporous silica materials.

2.2. Synthesis with the Separation of Alkane-Rich and Water-Rich Phases. In the alkane-assisted synthesis of mesoporous silica materials, the pore size and morphology of obtained silica materials follow the amount of alkane. Generally, the pore size increases with amount of alkane until a saturation value, beyond which further increasing amount of alkane can hardly affect the pore size. When the amount alkane is lower than the saturation value in surfactant micelles, the alkane mainly acts as swelling agents. The formation of emulsion or microemulsion will be most possible if the amount of alkane is higher than its saturation value in surfactant micelles [63, 70–79] and then leads to the hierarchical structures in micrometer or nanometer scale. Then, the droplets of alkane-surfactant-water microemulsion will lead to great change of morphology. Johansson et al. used *n*-heptane as prepared large pore SBA-15 and found that the sheets of obtained SBA-15 are fragments of the spheres with a diameter more than 20 μm and a sheet thickness of ~ 400 nm, reflecting the existence of emulsion droplets during synthesis and the channel length of SBA-15 around 400 nm [80, 81]. The same group also employed the same strategy to prepare SBA-16 with expanded mesopores in the walls of the hollow spheres with a diameter of 10 to 30 μm [82]. The hexagonally ordered pore structure can be maintained only for very low TMB/P123 molar ratio but a MCF mesoporous silica will be obtained upon increasing TMB/P123 ratio [70, 71]. When TIPB was

used as swelling agent, the obtained silica material changes from hexagonally ordered structure for low TIPB/P123 ratio to a vesicle-like structure for high TIPB/P123 ratio [83].

The formation of microemulsion can be avoided by adding alkanes after silica source and the formation of embryonic mesoporous silica [84]. In the synthetic processes reported by Sun et al. [37, 43, 55, 56] and Zhang et al. [51] (see Section 2.1.2), alkanes were premixed with silica source and then added into reaction mixture with one exception, in which decane was added into P123-HCl solution before the addition of TEOS [34]. The formation of microemulsion can be possibly depressed in these cases [37, 43, 51, 55, 56]. However, the separation of alkane-rich phase and water-rich phase is inevitable when the amount of alkane is much higher than its solubilization capacity (saturation value) in surfactant micelles. Such separation of oil-phase and water-phase will inevitably result in irregular silica particles and the loss of highly ordered mesostructure.

Zhang et al. synthesized SBA-15 type mesoporous silica with *n*-decane as swelling agent in consideration of the fact that the excess amount of *n*-decane results in a separation of alkane-rich and water-rich layers after the addition of *n*-decane into P123- H_2O solution [52]. The amount (the typical decane/P123 molar ratio was 310) of added *n*-decane was much higher than its saturation value in P123 micelles [54]. Consequently, a clear separation of decane-P123-water mixture to form an upper alkane-rich layer and a water-rich layer can be observed after stopping stirring (Figure 7(e)). A clear water-rich layer can be obtained after the removal of the upper alkane-rich layer (Figure 7(i)). Then, the silica source TEOS was added in the remaining water-rich layer to complete the synthesis of MSM. In such a synthetic process, highly ordered SBA-15 type mesoporous silica materials can be obtained with the help of NH_4F . As we can see in Figure 7, different straight-chain alkanes such as *n*-hexane, *n*-heptane, *n*-octane, *n*-nonane, *n*-decane, *n*-undecane, *n*-dodecane, and *n*-bioctyl lead to the same phenomenon if they were put into the synthesis of MSM in a P123- H_2O system. These different straight-chain alkanes can lead the MSM materials with different pore structures and morphologies [52, 53]. If the separation of such alkane-P123-water mixtures or the removal of upper alkane-rich layer is omitted, only smashed hollow silica spheres in scattered scales can be achieved. This is different from the results achieved by Sun et al. [37, 43, 55, 56], Tian et al. [85], and Zhang et al. [34, 51], who did not observe any phase separation of alkane-P123- H_2O mixture to form upper alkane-rich layer and water-rich layer like that in Figure 7.

With the decane/P123 molar ratio ranging from 310 to 119, hexagonally ordered SBA-15 type mesoporous silica can be obtained with a TEOS/P123 molar ratio of 41.4. The decane/P123 ratio at 119 needs an increased TEOS/P123 ratio at 59.6 to ensure the formation of hexagonally ordered SBA-15 type mesoporous silica. The pore size of the obtained mesoporous silica materials is around 12.2 nm, which is obviously larger than that of conventional SBA-15 type silica but smaller than that reported by Zhang et al. and Sun et al. using *n*-decane as swelling agent [34, 55, 56]. The changes of decane/P123 ratio and TEOS/P123 ratio just make the pore



FIGURE 7: Phase separation of alkane-P123-H₂O mixture to form upper alkane-rich layer and water-rich layer: (a) *n*-hexane; (b) *n*-heptane; (c) *n*-octane; (d) *n*-nonane; (e) *n*-decane; (f) *n*-undecane; (g) *n*-dodecane; (h) *n*-bioctyl; (i) the upper alkane-rich layer removed heptane-P123-H₂O mixture.

size of final products vary in a narrow range, reflecting that the solubilized decane in P123 micelles that had reached its saturation value.

The TEM images indicate that these SBA-15 type silica particles have hexagonally ordered nanochannels about 400 nm long. These hexagonally ordered nanochannels are along the direction vertical so that the particles grow.

Additionally, the alternating protuberant and hollow parts are partially a replica of these hexagonally ordered channels along the direction where those particles grow. The 3D tomography scan (Figure 8) indicates that the morphology of the obtained mesoporous silica is hierarchical 3D cocoon-like pouches with the wall constructed by hexagonally ordered nanochannels, which are characterized by their μm

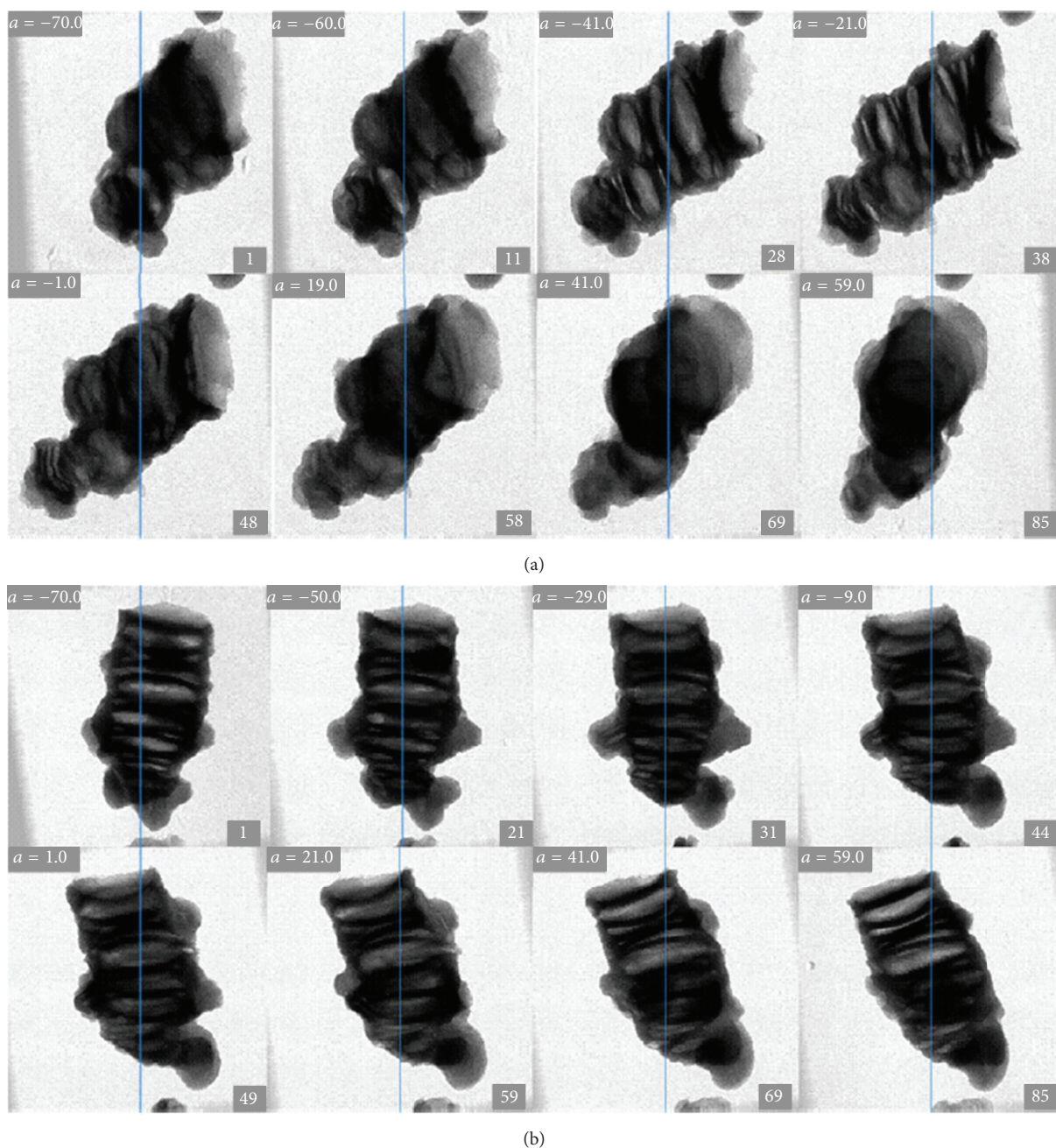


FIGURE 8: A sequence of TEM images obtained in 3-dimensional tomography scans along the axis (a) perpendicular and (b) parallel to the long axis of a particle of the material prepared at a decane/P123 molar ratio of 310 and a TEOS/P123 molar ratio of 41.4. Reprinted with permission from [52]. Copyright (2012) Elsevier.

symmetry of SBA-15 type mesoporous silica. Then, the channel length of these particles is decided by the size of these 3D cocoon-like pouches and is around 200–400 nm. One side of these cocoon-like pouches is open, implying possible application of this material in drug delivery, separation, adsorption, nanoreactor, and so forth [86].

The mechanism for the formation of this cocoon-like pouches was suggested to be an oil-in-water (O/W) emulsion assisted process [52]. In such oil-in-water emulsion assisted process, the residual *n*-decane in the water-rich layer plays

two roles. The first one is to act as the swelling agent leading to enlarged pore size of obtained mesoporous silica. Meanwhile, the residual *n*-decane in the water-rich layer enables the formation of O/W emulsion. The droplets of such O/W emulsion present in the synthetic system and the crystallites of embryonic silica particle prefer to attach to the outside of these droplets. The attachment of these crystallites to O/W emulsion droplets is energetically more favorable to other crystallites in an end-to-end way. However, the O/W emulsion droplets can aggregate in the hydrolysis process and

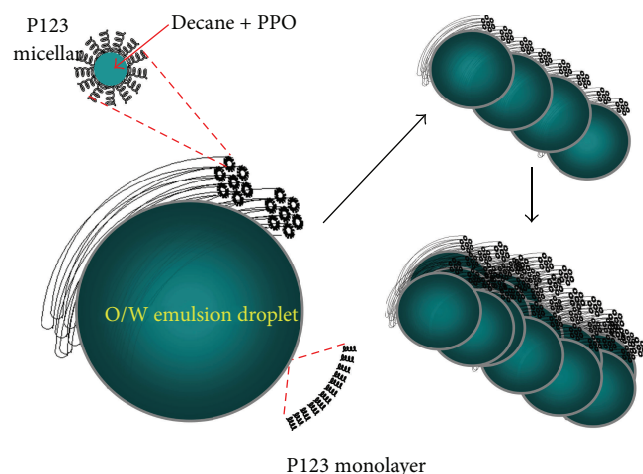


FIGURE 9: Schematic illustration of the motif of O/W emulsion assisted process. Reprinted with permission from [52]. Copyright (2012) Elsevier.

hydrothermal process and then build in cocoon-like pouches, whose walls are constructed by highly ordered hexagonal channels of SBA-15 type silica materials. If stirring is stopped as soon as the white precipitation appears after the addition of TEOS [52, 87–89], neither hexagonally ordered mesostructure nor cocoon-like morphology but onion-like or cracked onion-like silica spheres with some parallel nanochannels along them were obtained [52], reflecting the formation of O/W emulsion in this synthetic system. These onion-like silica spheres are composed of aggregated nanochannels 100–200 nm long, which is very close to the channel length of these cocoon-like pouches. These onion-like silica spheres are embryonic patterns of final products. According to this mechanism, the channel length of obtained MSM is decided by the diameter of O/W emulsion droplets. This mechanism (see Figure 9) is also reflected by the other synthesis of MSM with emulsion templating and characterized by the hierarchical hollow spherical morphologies of obtained MSM [68, 80–82, 90, 91].

In Figure 7, the *n*-hexane-P123-water and *n*-dodecane-P123-water systems also show the phase separation to form upper alkane-rich layer and water-rich layer below. With the removal of upper alkane-rich layer prior to the addition of TEOS, only *n*-decane-P123-water system can result in the formation of hexagonally ordered MSM [53]. The *n*-hexane-P123-water system leads to the formation of MCF material, which has typical MCF morphology and mesostructure as that of the MCF materials prepared with TMB [9] or TIPB [41, 42, 58, 67]. However, the pore size of such MCF material prepared with *n*-hexane is around 10 nm, much different from that of the MCF materials prepared with TMB or TIPB. The small pore size of the MCF material should be due to the smaller molecular size of *n*-hexane than that of TMB or TIPB. The *n*-dodecane-P123-water system results in a nanosized fiber-like MSM, which is composed of silica nanotube bundles. These nanotube bundles contain just several nanotube channels arranged parallel in one unit. The pore sizes of the

MSM prepared with *n*-hexane, *n*-decane, and *n*-dodecane vary from 10 nm (*n*-hexane) to 11 nm (*n*-dodecane) and 12 nm (*n*-decane), indicating that the swelling effects of these straight-chain alkanes are comparable although the chain length and molecule size of them are remarkably different.

In the syntheses assisted by *n*-hexane, *n*-decane, and *n*-dodecane, the molecular ratios of alkane/P123 and TEOS/P123 were all calculated by the amount of alkane, and P123 and TEOS were added into the system [52, 53]. The removed upper alkane-rich layer also contains P123 and water in addition to alkane and thus the ratios of alkane/P123 in the residual water-rich layers are different from the original ones.

The pore expanding effect of decane in the synthesis of MSM templated by other nonionic gemini surfactant (E900Myr) under neutral pH was also studied [45]. Upon addition of decane the hexagonal structure was kept as far the concentration of oil remained lower than 10 wt%. If the hydrothermal treatment was carried out at low temperature of 50°C, a slight increase of the mesopore diameter was observed in the presence of decane. Increasing the temperature up to 80°C, the mean pore diameter decreases, in contrary to pore expanding upon the addition of decane. At the same time, better mesopore homogeneity and a larger wall thickness can be obtained. At high decane concentration, the oil-in-water emulsions formed by E900Myr/decane/water system could be used as template for the formation of hierarchical porous silica materials, which is quite different from the effect of increasing alkane/P123 molar ratio discovered by Sun et al. [37, 43, 55, 56] and Zhang et al. [34, 51]. Notably, the amount of ethanol can determine the pore size and the construction of pore structure while the concentration of NH₄OH can directly influence and control the condensation rate of silica source and leads to different mesostructures.

3. The Application of the Mesoporous Silica Synthesized with Straight-Chain Alkanes

Since the invention of MSM such as MCM-41 and SBA-15, their application in abundant fields has been widely proposed and developed due to the potentiality to achieve a so-called nanoeffect in their nanochannels [75, 92–94]. Janssen et al. used 3D-TEM to study the shape of SBA-15 and found that the conventional SBA-15 MSM is composed of long and curved mesopores, which is not favorable to its application in many fields [95]. TMB [9, 10, 29–32], TIPB, and cyclohexane [28, 40–42, 96] were used by many scientists as pore expanders to achieve big pore size but these swelling agents can also remarkably change the mesostructures and morphologies of obtained MSM materials. More importantly, these branch-chain alkanes like TMB and TIPB normally exhibit very good pore expanding effect due to their relatively big molecular size, but this also means that they can hardly lead to a mesopore in a medium size. The use of TMB or TIPB as swelling agent can lead to a mesocellular foam silica (MCFs) with pore size as big as 30–50 nm but cannot lead to a MCFs with pore size as narrow as 10 nm [10, 29–31, 97]. The use of *n*-hexane as swelling agent with a phase separation of hexane-P123-H₂O mixture and the removal of upper hexane-rich layer results in a MCFs material with mesopores as

big as only 10 nm [53]. The straight-chain alkenes assisted synthetic systems make it possible to develop unconventional mesoporous silica materials with the characteristics like enlarged pore size, short channel length, and hierarchically constructed mesostructure and then remarkably enhance the application of mesoporous silica materials in different fields.

3.1. Adsorption and Separation. In chromatographic separation, using MSM as stationary phases, pore size is requested to be larger than 4 nm to expand their application in the chromatographic separation of biomolecules and aromatic molecules. The SBA-15 type MSM prepared using a synthetic system of decane-P123-water-TEOS exhibits a pore size of 12 nm as well as an average particle size of 400 nm [85]. The C18 derivative of this unconventional SBA-15 type MSM was packed into 50 μm capillary for the application of capillary electrochromatography (CEC). Such material was found to be effective packing material for CEC application in either normal-phase or reverse-phase mode. In the normal-phase mode, high efficiency can be achieved for the separation of polar solutes due to the submicrometer particle size. In reverse-phase mode, high-speed separation of neutral and basic compounds can be achieved in 60 s.

Using the abovementioned pore-expanded MSM as support materials [69, 98], a model enzyme (Lysozyme) was introduced into the tunable nanopores of these nanoparticles. It was found that the pore-expanded silica shows larger adsorption capacity than the conventional mesoporous silica with pore size of 2.5 nm. The channel length of these pore-expanded mesoporous silica nanoparticles is less than 100 nm and these materials exhibit good potential to be a suitable carrier for enzyme delivery in the future [69]. The SBA-15 type material with an enlarged pore size of 12.0 nm shows higher adsorption capacity of lysozyme of 420.8 mg g^{-1} , in contrast to 63.8 mg g^{-1} for a MCM-41 type material with a pore size of 2.05 nm and 191.3 mg g^{-1} for a conventional SBA-15 type material with a pore size of 8.45 nm [99]. The reason for the high adsorption capacity of the SBA-15 materials is that the size of lysozyme is larger than MCM-41 pores but well suits the pore size of SBA-15 materials. A SBA-15 material was synthesized with the assistance of octane and employed for adsorption of biomolecules and showed the highest maximum adsorption capacity of bovine serum albumin (BSA) and lysozyme (LYS) [100].

The platelet-like SBA-15 type silica prepared with *n*-decane was modified by amine and employed in the adsorption of CO_2 [61, 101]. Besides the pore size and pore volume, the channel length of mesoporous silica plays a significant role in the performance of supported polyethylenimine (PEI) for CO_2 adsorption. The short channel SBA-15 silica prepared with *n*-decane was found to be a much better support for PEI and CO_2 uptake at low temperature due to diminished diffusion. In the adsorption of acid dyes, the short channeling pores of the amino-functionalized SBA-15 platelets facilitated the diffusion of dye molecules inside the pores and prevented the aggregation of dye molecules from the blocking of the pores [102]. However, the adsorption capacity is dependent on the amount of amino-loading and surface area

of the SBA-15 materials. Another thing that needs to be noticed is that the adsorption of volatile organic compounds (VOCs) such as toluene and benzene with MSM materials is probably not favored by short channel but long nanochannel of conventional fiber-like SBA-15 [103].

3.2. Hard Template. The mesoporous silica materials obtained in the straight-chain assisted system can be used as hard templates for the preparation of other mesoporous materials [104, 105]. The assistance of *n*-hexane leads to formation of a macromesoporous silica material, which was used as the hard template for the preparation of hierarchically ordered macromesoporous carbon materials [106].

3.3. Catalysis. The MSM materials obtained in straight-chain alkanes assisted synthesis can offer short-length mesopores, which can lead to easy mass transfer in both biomolecule absorption and the facile assembly of metal nanocomposites within their pore channels [107, 108].

The abovementioned SBA-15 type mesoporous silica [52, 53] prepared with the assistance of *n*-decane was employed as the support material of immobilized chiral Mn(salen) catalyst for the heterogeneous asymmetric epoxidation of unfunctionalized olefins [109]. Motion restriction and confinement effect in the nanochannels of support materials can affect the cis/trans ratio and enantioselectivity of obtained chiral epoxides. In the nanochannels of mesoporous silica with tunable pore dimension and channel length, motion restriction and confinement effect can be tuned and thus the product distribution of heterogeneous asymmetric epoxidation can be adjusted sequentially.

Decane and dodecane were used as swelling agents to prepare the SBA-15 type mesoporous silica materials with enlarged pore size (around 11 nm) and short channel length (300–500 nm) [110]. The impact of channel length on metal dispersion and the catalytic performance of Ru-Co/SBA-15 catalysts in Fischer-Tropsch synthesis had been investigated. The long channel length (up to 10 μm) and corresponding long channel-residence time for conventional SBA-15 promote the formation of highly aggregated rod-like CO_3O_4 particles. The short channel SBA-15 silicas were found to be able to greatly enhance the dispersion of metal active species. The high dispersion of metal active species leads to a higher Co-time-yield under realistic Fischer-Tropsch conditions. At 55% CO conversion level, the selectivity to desired C5+ fraction progressively increases when the channel length of the SBA-15 support is gradually shortened. The design of Fischer-Tropsch catalysts on the short channel SBA-15 silica with large pore size was suggested to be a successful strategy toward improved catalytic activity and C5+ hydrocarbon selectivity.

In the oxidative removal of 4,6-dimethyldibenzothiophene (4,6-DMDBT), Sun et al. found that the catalytic performance of Ti-HMS molecular sieve can be remarkably enhanced while its pore size was expanded from 2.3 nm to 3.7 nm with the addition of *n*-hexane or *n*-octane in its preparation [57]. However, the effect of the addition *n*-hexane or *n*-octane on the morphology of obtained Ti-HMS material was absent.

TABLE 1: Straight-chain alkanes as swelling agents in the preparation of MSM.

Carbon atoms (<i>n</i>) of alkanes (C _{<i>n</i>} H _{2<i>n</i>+2})	Surfactant	Molar ratio of silica precursor to surfactant	Parameters of synthesis		Temperature of hydrolysis (°C)	Solvent	Pore size (nm)	XRD pattern and TEM image	Morphology	Salt	Ref.
			Molar ratio of alkane to surfactant	Molar ratio of alkane to surfactant							
5~8	CTAB	6.25	1	1	nd	NaOH	4.2~5.1	oh	nd	—	[48]
9~15							6.2~7.4				
>15							6.4~7.0				
10 ^a	P123	59.2	237	237	40	HCl ^d	12.1	oh	Platelet-like	NH ₄ F ^c	[34]
6 ^b	P123	59.6	240	240	<17 ^g	HCl ^e	15.7	oh	Short fiber-like	NH ₄ F	[37]
7 ^b					<22 ^g		15.0				
9 ^b					<27 ^g		13.4				
6 ^b	P123	62.5	239.3	239.3	15	HCl ^e	12~18	oh	nd	NH ₄ F	[49]
8, 9 ⁱ	Triblock copolymer ^h	60	0~298	0~298	35	HCl ^f	10.3~14.1	dm	nd	NH ₄ F	[50]
10, 13, 16, 20 ⁱ							8.4~10.1	oh	nd		
8 ^b	P123	48	235	235	25	HCl ^e	13	2dp	Nanotube bundles	NH ₄ F	[43]
10 ^b	P123	48	134	134	30	HCl ^e	12	2dp	Nano-fibers	NH ₄ F	
					40		50	dv	Multilamellar vesicles		
					60		35	dm	MCF		
6 ^b	P123	60	235	235	15 ± 2	HCl ^j	15.7	oh	Bunch-like	NH ₄ F	[51]
7 ^b					20 ± 2		15.0		Dripstone-like		
8 ^b					25 ± 2		nd	oh	Rod-like		
9 ^b					27 ± 2		13.4	oh	Flat-like		
10 ^b					35 ± 2		12.0	oh	Kernel-like		
12 ^b					40 ± 2		12.0	oh	Column-like		
10 ^b			135	135	35 ± 2		nd	oh	Chain-like		
10 ^b			755	755			nd	oh	Monolith-like		
10 ^b		48	235	235			nd	oh	Fiber-like		
10 ^b		77					nd	oh	Platelet-like		
10 ^b		110					nd	oh	Film-like		
10 ^{a,j}	P123	41.4~59.6 ^l	119~310 ^l	119~310 ^l	40	HCl ^d	~12.2	oh	Cocoon-like	NH ₄ F	[52, 53]
6 ^{a,j}	P123	41.4 ^l	390 ^l	390 ^l	40	HCl ^k	10	dm	MCF	NH ₄ F	[53]
12 ^{a,j}			197.5 ^l	197.5 ^l			11	2dp	Nanotube bundles		

oh: ordered hexagonal; dm: disordered MCF; 2dp: 2-dimensionally parallel; dv: disordered vesicles; nd: not demonstrated. ^a Alkane was added into P123-H₂O/HCl solution before the addition of silica precursor. ^b Alkane and silica precursor were premixed and then added into P123-HCl solution. ^c Only disordered MCF could be obtained without NH₄F. ^d 1.07 M. ^e 1.30 M. ^f 0.43 M. ^g 1.20 M. ^h 1.1 M. ⁱ Disordered mesostructure will arise if the hydrolysis temperature is higher than the critical value for each alkane. ^j [Poly(ethylene glycol)₂₀-poly(propylene glycol)₇₀-poly(ethylene glycol)₂₀] (Dat-ichi Kogyo Seiyaku, Japan). ^k Surfactant was added into deionized water to form a surfactant-H₂O solution, followed by the addition of TEOS and HCl, step by step. ^l A clear separation of decane-P123-water mixture leads to upper alkane-rich layer and water-rich layer. The upper decane-rich layer was removed and then TEOS was added. ^m The molecular ratios of alkane/P123 and TEOS/P123 were all calculated by the amount of alkane, P123, and TEOS added into the system.

A SBA-15 material prepared with the assistance of *n*-decane demonstrates appropriate channel size (14.0 nm) and best capacity of lipase. The immobilized catalyst with this SBA-15 material shows much higher activity and sustainability of activity than the immobilized catalysts with a MCM-41 material (channel size 1.8 nm) and a MCF material (channel size 28.0 nm) as support materials in the transformation of unrefined wasted cooking oil to biodiesel [111].

n-Hexane was used as swelling agent for the preparation of variable pore diameter SBA-15 materials and [39]. The SBA-15 supported catalyst with pore diameter of 10 nm sufficient mass transfer of reactant liquids and gases through the catalyst's pores while still maintaining a high surface area necessary for metal dispersion.

4. Conclusions

It is possible to tune the mesostructure and morphology of MSM by controlling the type and amount of surfactant and silica source and other synthesis parameters, that is, temperature, inorganic mineralizing agent, and the way to introduce the swelling agent into reaction mixture. Acting as swelling agents, straight-chain alkanes (C_nH_{2n+2} , $n = 5$ to 20) have been widely used in the synthetic systems of C_nH_{2n+2} -surfactant-water-SiO₂ (see Table 1), which play a critical role in fabrication of MSM with tunable pore diameter, channel length, and specific morphology. The MSM prepared with the assistance of straight-chain alkanes is characterized by enlarged pore diameter, short channel length, and hierarchically constructed mesostructure. Their application indicates that the exploitation of these unconventional mesoporous silica materials is a prospectively successful strategy in the fields, for example, catalysis, adsorption, separation, and nanomaterial preparation.

Conflict of Interests

The authors declare that there is no conflict of interests regarding the publication of this paper.

Acknowledgments

The authors are grateful for National Natural Science Foundation of China (Grants nos. U1362105 and 21273076), Chongqing Research Program of Basic Research and Frontier Technology (nos. cstc2013jcyjA50007 and cstc2015shms-ztxz20001), Chongqing Science Research Project (KJ130729), and Key Laboratory of Catalysis Science and Technology of Chongqing Education Commission (1456031).

References

- [1] Y. Wan and D. Y. Zhao, "On the controllable soft-templating approach to mesoporous silicates," *Chemical Reviews*, vol. 107, no. 7, pp. 2821–2860, 2007.
- [2] J. S. Beck, J. C. Vartuli, G. J. Kennedy, C. T. Kresge, W. J. Roth, and S. E. Schramm, "Molecular or supramolecular templating: defining the role of surfactant chemistry in the formation of microporous and mesoporous molecular sieves," *Chemistry of Materials*, vol. 6, no. 10, pp. 1816–1821, 1994.
- [3] J. S. Beck, J. C. Vartuli, W. J. Roth et al., "A new family of mesoporous molecular sieves prepared with liquid crystal templates," *Journal of the American Chemical Society*, vol. 114, no. 27, pp. 10834–10843, 1992.
- [4] C. T. Kresge, M. E. Leonowicz, W. J. Roth, J. C. Vartuli, and J. S. Beck, "Ordered mesoporous molecular sieves synthesized by a liquid-crystal template mechanism," *Nature*, vol. 359, no. 6397, pp. 710–712, 1992.
- [5] J. C. Vartuli, K. D. Schmitt, C. T. Kresge et al., "Effect of surfactant silica molar ratios on the formation of mesoporous molecular-sieves-inorganic mimicry of surfactant liquid-crystal phase and mechanistic implications," *Chemistry of Materials*, vol. 6, pp. 2317–2326, 1994.
- [6] W. J. Roth and J. C. Vartuli, "Synthesis of mesoporous molecular sieves," in *Zeolites and Ordered Mesoporous Materials: Progress and Prospects*, J. Cejka and H. VanBekum, Eds., vol. 157 of *Studies in Surface Science and Catalysis*, pp. 91–110, Elsevier Science Bv, Amsterdam, The Netherlands, 2005.
- [7] J. S. Beck and J. C. Vartuli, "Recent advances in the synthesis, characterization and applications of mesoporous molecular sieves," *Current Opinion in Solid State and Materials Science*, vol. 1, no. 1, pp. 76–87, 1996.
- [8] Q. S. Huo, D. I. Margolese, U. Ciesla et al., "Generalized synthesis of periodic surfactant inorganic composite-materials," *Nature*, vol. 368, no. 6469, pp. 317–321, 1994.
- [9] D. Y. Zhao, Q. S. Huo, J. L. Feng, B. F. Chmelka, and G. D. Stucky, "Nonionic triblock and star diblock copolymer and oligomeric surfactant syntheses of highly ordered, hydrothermally stable, mesoporous silica structures," *Journal of the American Chemical Society*, vol. 120, no. 24, pp. 6024–6036, 1998.
- [10] D. Y. Zhao, J. L. Feng, Q. S. Huo et al., "Triblock copolymer syntheses of mesoporous silica with periodic 50 to 300 angstrom pores," *Science*, vol. 279, no. 5350, pp. 548–552, 1998.
- [11] F. Kleitz, T. Czuryzskiewicz, L. A. Solovyov, and M. Lindén, "X-ray structural modeling and gas adsorption analysis of cage-like SBA-16 silica mesophases prepared in a F127/butanol/H₂O system," *Chemistry of Materials*, vol. 18, no. 21, pp. 5070–5079, 2006.
- [12] J. C. Vartuli, K. D. Schmitt, C. T. Kresge et al., "Development of a formation mechanism for M41S materials," *Studies in Surface Science and Catalysis*, vol. 84, pp. 53–60, 1994.
- [13] A. A. Romero, M. D. Alba, W. Z. Zhou, and J. Klinowski, "Synthesis and characterization of the mesoporous silicate molecular sieve MCM-48," *Journal of Physical Chemistry B*, vol. 101, no. 27, pp. 5294–5300, 1997.
- [14] M. W. Anderson, "Simplified description of MCM-48," *Zeolites*, vol. 19, no. 4, pp. 220–227, 1997.
- [15] S. A. Bagshaw, E. Prouzet, and T. J. Pinnavaia, "Templating of mesoporous molecular sieves by nonionic polyethylene oxide surfactants," *Science*, vol. 269, no. 5228, pp. 1242–1244, 1995.
- [16] H. D. Zhang, L. Zhang, Z. C. Feng et al., "Selective oxidation of methane to formaldehyde over MSU-2-supported Sb-V mixed oxide catalyst," *Chinese Journal of Catalysis*, vol. 26, no. 7, pp. 542–544, 2005.
- [17] C. Boissiere, A. Larbot, A. van der Lee, P. J. Kooyman, and E. Prouzet, "A new synthesis of mesoporous MSU-X silica controlled by a two-step pathway," *Chemistry of Materials*, vol. 12, no. 10, pp. 2902–2913, 2000.
- [18] S. A. Bagshaw, "Modification of [M]-MSU-X mesoporous silicate pore morphology by post-synthesis treatment," *Chemical Communications*, no. 3, pp. 271–272, 1999.

- [19] A. B. Chen, Y. F. Yu, H. J. Lv, Y. Zhang, T. T. Xing, and Y. H. Yu, "Synthesis of hollow mesoporous silica spheres and carambola-like silica materials with a novel resin sphere as template," *Materials Letters*, vol. 135, pp. 43–46, 2014.
- [20] B. Liu, L. Han, and S. A. Che, "Formation of enantiomeric impeller-like helical architectures by DNA self-assembly and silica mineralization," *Angewandte Chemie: International Edition*, vol. 51, no. 4, pp. 923–927, 2012.
- [21] D. Y. Zhao, J. Y. Sun, Q. Z. Li, and G. D. Stucky, "Morphological control of highly ordered mesoporous silica SBA-15," *Chemistry of Materials*, vol. 12, no. 2, pp. 275–279, 2000.
- [22] A. S. M. Chong and X. S. Zhao, "Functionalization of SBA-15 with APTES and characterization of functionalized materials," *Journal of Physical Chemistry B*, vol. 107, no. 46, pp. 12650–12657, 2003.
- [23] H. B. S. Chan, P. M. Budd, and T. D. Naylor, "Control of mesostructured silica particle morphology," *Journal of Materials Chemistry*, vol. 11, no. 3, pp. 951–957, 2001.
- [24] B. Z. Li, X. F. Pei, S. B. Wang et al., "Formation of hollow mesoporous silica nanoworm with two holes at the terminals," *Nanotechnology*, vol. 21, no. 2, Article ID 025601, 2010.
- [25] Y. L. Chen, Y. X. Chen, Y. Li et al., "Preparation of ethylene-silica hollow spheres with a single-layer mesopores using a chiral amphiphile," *Journal of Nanoscience and Nanotechnology*, vol. 11, no. 5, pp. 4073–4078, 2011.
- [26] Y. L. Chen, Y. Li, W. Zhuang et al., "Formation of silica nanotubes with spring-like pore channels in the walls," *Materials Chemistry and Physics*, vol. 127, no. 3, pp. 426–432, 2011.
- [27] S. Yang, X. Zhou, P. Yuan et al., "Siliceous nanopods from a compromised dual-templating approach," *Angewandte Chemie—International Edition*, vol. 46, no. 45, pp. 8579–8582, 2007.
- [28] M. Kruk, "Access to ultralarge-pore ordered mesoporous materials through selection of surfactant/swelling-agent micellar templates," *Accounts of Chemical Research*, vol. 45, no. 10, pp. 1678–1687, 2012.
- [29] P. Schmidt-Winkel, J. W. W. Lukens, D. Y. Zhao, P. D. Yang, B. F. Chmelka, and G. D. Stucky, "Mesocellular siliceous foams with uniformly sized cells and windows," *Journal of the American Chemical Society*, vol. 121, no. 1, pp. 254–255, 1999.
- [30] J. J. Ma, Q. M. Liu, D. D. Chen, S. Wen, and T. H. Wang, "Synthesis and characterization of pore-expanded mesoporous silica materials," *Micro & Nano Letters*, vol. 10, no. 2, pp. 140–144, 2015.
- [31] J. L. Blin and B. L. Su, "Tailoring pore size of ordered mesoporous silicas using one or two organic auxiliaries as expanders," *Langmuir*, vol. 18, no. 13, pp. 5303–5308, 2002.
- [32] C. L. Xin, N. Zhao, H. J. Zhan, F. K. Xiao, W. Wei, and Y. H. Sun, "Phase transition of silica in the TMB-P123-H₂O-TEOS quadru-component system: a feasible route to different mesostructured materials," *Journal of Colloid and Interface Science*, vol. 433, pp. 176–182, 2014.
- [33] L. Huang and M. Kruk, "Synthesis of ultra-large-pore FDU-12 silica using ethylbenzene as micelle expander," *Journal of Colloid and Interface Science*, vol. 365, no. 1, pp. 137–142, 2012.
- [34] H. Zhang, J. M. Sun, D. Ma et al., "Unusual mesoporous SBA-15 with parallel channels running along the short axis," *Journal of the American Chemical Society*, vol. 126, no. 24, pp. 7440–7441, 2004.
- [35] S. M. Egger, K. R. Hurley, A. Datt, G. Swindlehurst, and C. L. Haynes, "Ultraporous mesostructured silica nanoparticles," *Chemistry of Materials*, vol. 27, no. 9, pp. 3193–3196, 2015.
- [36] J. L. Blin, C. Otjacques, G. Herrier, and B.-L. Su, "Pore size engineering of mesoporous silicas using decane as expander," *Langmuir*, vol. 16, no. 9, pp. 4229–4236, 2000.
- [37] J. M. Sun, H. Zhang, D. Ma et al., "Alkanes-assisted low temperature formation of highly ordered SBA-15 with large cylindrical mesopores," *Chemical Communications*, no. 42, pp. 5343–5345, 2005.
- [38] W. J. Shan, W. Wang, and H. Q. Ru, "Siliceous mesocellular foams modified via a partitioned cooperative self-assembly process using hexane as pore swelling agent," *Journal of Non-Crystalline Solids*, vol. 425, pp. 183–189, 2015.
- [39] P. E. Boahene, K. K. Soni, A. K. Dalai, and J. Adjaye, "Application of different pore diameter SBA-15 supports for heavy gas oil hydrotreatment using FeW catalyst," *Applied Catalysis A: General*, vol. 402, no. 1–2, pp. 31–40, 2011.
- [40] Y. Y. Li and M. Kruk, "Single-micelle-templated synthesis of hollow silica nanospheres with tunable pore structures," *RSC Advances*, vol. 5, no. 85, pp. 69870–69877, 2015.
- [41] L. Cao and M. Kruk, "Short synthesis of ordered silicas with very large mesopores," *RSC Advances*, vol. 4, no. 1, pp. 331–339, 2014.
- [42] L. Cao and M. Kruk, "Synthesis of large-pore SBA-15 silica from tetramethyl orthosilicate using triisopropylbenzene as micelle expander," *Colloids and Surfaces A: Physicochemical and Engineering Aspects*, vol. 357, no. 1–3, pp. 91–96, 2010.
- [43] J. M. Sun, H. Zhang, R. J. Tian et al., "Ultrafast enzyme immobilization over large-pore nanoscale mesoporous silica particles," *Chemical Communications*, no. 12, pp. 1322–1324, 2006.
- [44] A. Sayari, Y. Yang, M. Kruk, and M. Jaroniec, "Expanding the pore size of MCM-41 silicas: use of amines as expanders in direct synthesis and postsynthesis procedures," *Journal of Physical Chemistry B*, vol. 103, no. 18, pp. 3651–3658, 1999.
- [45] A. May-Masnou, A. Pasc, M. J. Stébé, J. M. Gutiérrez, M. Porras, and J. L. Blin, "Solubilization of decane into gemini surfactant with a modified Jeffamine backbone: design of hierarchical porous silica," *Microporous & Mesoporous Materials*, vol. 169, pp. 235–241, 2013.
- [46] Q. S. Huo, D. I. Margolese, U. Ciesla et al., "Organization of organic molecules with inorganic molecular species into nanocomposite biphasic arrays," *Chemistry of Materials*, vol. 6, no. 8, pp. 1176–1191, 1994.
- [47] J. Fan, C. Z. Yu, J. Lei et al., "Low-temperature strategy to synthesize highly ordered mesoporous silicas with very large pores," *Journal of the American Chemical Society*, vol. 127, no. 31, pp. 10794–10795, 2005.
- [48] N. Ulagappan and C. N. R. Rao, "Evidence for supramolecular organization of alkane and surfactant molecules in the process of forming mesoporous silica," *Chemical Communications*, no. 24, pp. 2759–2760, 1996.
- [49] M. Kruk and L. Cao, "Pore size tailoring in large-pore SBA-15 silica synthesized in the presence of hexane," *Langmuir*, vol. 23, no. 13, pp. 7247–7254, 2007.
- [50] S. K. Jana, R. Nishida, K. Shindo, T. Kugita, and S. Namba, "Pore size control of mesoporous molecular sieves using different organic auxiliary chemicals," *Microporous and Mesoporous Materials*, vol. 68, no. 1–3, pp. 133–142, 2004.
- [51] H. Zhang, J. M. Sun, D. Ma, G. Weinberg, D. S. Su, and X. K. Bao, "Engineered complex emulsion system: toward modulating the pore length and morphological architecture of mesoporous silicas," *Journal of Physical Chemistry B*, vol. 110, no. 51, pp. 25908–25915, 2006.

- [52] H. D. Zhang, Y.-M. Wang, K. Lü et al., "Hierarchical fabrication of silica cocoon with hexagonally ordered channel constructed wall via an emulsion-assisted process," *Microporous and Mesoporous Materials*, vol. 150, no. 1, pp. 90–95, 2012.
- [53] H. D. Zhang and Y. Shen, "Straight chain alkane-assisted synthesis of mesoporous silica," *Materials Letters*, vol. 75, pp. 183–185, 2012.
- [54] R. Nagarajan, "Solubilization of hydrocarbons and resulting aggregate shape transitions in aqueous solutions of Pluronic (PEO-PPO-PEO) block copolymers," *Colloids and Surfaces B: Biointerfaces*, vol. 16, no. 1–4, pp. 55–72, 1999.
- [55] J. M. Sun, D. Ma, H. Zhang et al., "Organic molecule-modulated phase evolution of inorganic mesostructures," *Langmuir*, vol. 24, no. 6, pp. 2372–2380, 2008.
- [56] J. M. Sun, D. Ma, H. Zhang et al., "Phase evolution in the alkane-PI23-water-TEOS quadru-component system: a feasible route to different complex mesostructured materials," *Journal of Materials Chemistry*, vol. 16, no. 16, pp. 1507–1510, 2006.
- [57] D. W. Sun, G. Li, C. Z. Jin, L. X. Zhao, and X. S. Wang, "Effect of straight chain alkanes on the synthesis of Ti-HMS molecular sieve," *Chinese Journal of Catalysis*, vol. 28, pp. 479–483, 2007.
- [58] L. Cao and M. Kruk, "Facile method to synthesize platelet SBA-15 silica with highly ordered large mesopores," *Journal of Colloid and Interface Science*, vol. 361, no. 2, pp. 472–476, 2011.
- [59] Sujandi, S.-E. Park, D.-S. Han, S.-C. Han, M.-J. Jin, and T. Ohsuna, "Amino-functionalized SBA-15 type mesoporous silica having nanostructured hexagonal platelet morphology," *Chemical Communications*, no. 39, pp. 4131–4133, 2006.
- [60] K. Kosuge, T. Sato, N. Kikukawa, and M. Takemori, "Morphological control of rod-and fiberlike SBA-15 type mesoporous silica using water-soluble sodium silicate," *Chemistry of Materials*, vol. 16, no. 5, pp. 899–905, 2004.
- [61] A. Heydari-Gorji, Y. Yang, and A. Sayari, "Effect of the pore length on CO₂ adsorption over amine-modified mesoporous silicas," *Energy and Fuels*, vol. 25, no. 9, pp. 4206–4210, 2011.
- [62] K. Shinoda and S. Friberg, "Microemulsions: colloidal aspects," *Advances in Colloid and Interface Science*, vol. 4, no. 4, pp. 281–300, 1975.
- [63] A. Kabalnov, B. Lindman, U. Olsson, L. Piculell, K. Thuresson, and H. Wennerström, "Microemulsions in amphiphilic and polymer-surfactant systems," *Colloid and Polymer Science*, vol. 274, no. 4, pp. 297–308, 1996.
- [64] P. D. I. Fletcher and K. Suhling, "Interactions between weakly charged oil-in-water microemulsion droplets," *Langmuir*, vol. 14, no. 15, pp. 4065–4069, 1998.
- [65] M. J. Lawrence and G. D. Rees, "Microemulsion-based media as novel drug delivery systems," *Advanced Drug Delivery Reviews*, vol. 45, no. 1, pp. 89–121, 2000.
- [66] M. Kobašljija and D. T. McQuade, "Polyurea microcapsules from oil-in-oil emulsions via interfacial polymerization," *Macromolecules*, vol. 39, no. 19, pp. 6371–6375, 2006.
- [67] Y.-Y. Fahn, A.-C. Su, and P. Shen, "Towerlike SBA-15: base and (10)-specific coalescence of a silicate-encased hexagonal mesophase tailored by nonionic triblock copolymers," *Langmuir*, vol. 21, no. 1, pp. 431–436, 2005.
- [68] E. M. Johansson, J. M. Córdoba, and M. Odén, "The effects on pore size and particle morphology of heptane additions to the synthesis of mesoporous silica SBA-15," *Microporous and Mesoporous Materials*, vol. 133, no. 1–3, pp. 66–74, 2010.
- [69] K.-C. Kao and C.-Y. Mou, "Pore-expanded mesoporous silica nanoparticles with alkanes/ethanol as pore expanding agent," *Microporous and Mesoporous Materials*, vol. 169, pp. 7–15, 2013.
- [70] P. Schmidt-Winkel, C. J. Glinka, and G. D. Stucky, "Microemulsion templates for mesoporous silica," *Langmuir*, vol. 16, no. 2, pp. 356–361, 2000.
- [71] J. S. Lettow, Y. J. Han, P. Schmidt-Winkel et al., "Hexagonal to mesocellular foam phase transition in polymer-templated mesoporous silicas," *Langmuir*, vol. 16, no. 22, pp. 8291–8295, 2000.
- [72] P. Schmidt-Winkel, W. W. Lukens Jr., P. D. Yang et al., "Microemulsion templating of siliceous mesostructured cellular foams with well-defined ultralarge mesopores," *Chemistry of Materials*, vol. 12, no. 3, pp. 686–696, 2000.
- [73] S. Schacht, Q. Huo, I. G. Voigt-Martin, G. D. Stucky, and F. Schüth, "Oil-water interface templating of mesoporous macro-scale structures," *Science*, vol. 273, no. 5276, pp. 768–771, 1996.
- [74] M. H. Wang, Z. K. Sun, Q. Yue et al., "An interface-directed coassembly approach to synthesize uniform large-pore mesoporous silica spheres," *Journal of the American Chemical Society*, vol. 136, no. 5, pp. 1884–1892, 2014.
- [75] M. Moritz and M. Geszke-Moritz, "Mesoporous materials as multifunctional tools in biosciences: principles and applications," *Materials Science and Engineering C*, vol. 49, pp. 114–151, 2015.
- [76] S.-H. Wu, Y. Hung, and C.-Y. Mou, "Compartmentalized hollow silica nanospheres templated from nanoemulsions," *Chemistry of Materials*, vol. 25, no. 3, pp. 352–364, 2013.
- [77] A. Lind, J. Andersson, S. Karlsson, M. Lindén, and J. B. Rosenholm, "Solubilization of benzene derivatives in silicate-surfactant systems," *Colloids and Surfaces A: Physicochemical and Engineering Aspects*, vol. 183, pp. 415–422, 2001.
- [78] M. Lindén, P. Ågren, S. Karlsson, P. Bussain, and H. Amenitsch, "Solubilization of oil in silicate-surfactant mesostructures," *Langmuir*, vol. 16, no. 13, pp. 5831–5836, 2000.
- [79] C. Oh, Y.-G. Lee, J.-H. Park, and S.-G. Oh, "Synthesis of silica microspheroids for templates in W/O reverse emulsion," *Colloids and Surfaces A: Physicochemical and Engineering Aspects*, vol. 269, no. 1–3, pp. 112–118, 2005.
- [80] E. M. Johansson, J. M. Córdoba, and M. Odén, "Synthesis and characterization of large mesoporous silica SBA-15 sheets with ordered accessible 18 nm pores," *Materials Letters*, vol. 63, no. 24–25, pp. 2129–2131, 2009.
- [81] E. M. Johansson, M. A. Ballem, J. M. Córdoba, and M. Odén, "Rapid synthesis of SBA-15 rods with variable lengths, widths, and tunable large pores," *Langmuir*, vol. 27, no. 8, pp. 4994–4999, 2011.
- [82] M. A. Ballem, E. M. Johansson, J. M. Córdoba, and M. Odén, "Synthesis of hollow silica spheres SBA-16 with large-pore diameter," *Materials Letters*, vol. 65, no. 7, pp. 1066–1068, 2011.
- [83] G. W. Zhou, Y. J. Chen, J. H. Yang, and S. H. J. Yang, "From cylindrical-channel mesoporous silica to vesicle-like silica with well-defined multilamella shells and large inter-shell mesopores," *Journal of Materials Chemistry*, vol. 17, no. 27, pp. 2839–2844, 2007.
- [84] T. Lu, X. D. Yao, G. Q. M. Lu, and Y. H. He, "Controlled evolution from multilamellar vesicles to hexagonal mesostructures through the addition of 1,3,5-trimethylbenzene," *Journal of Colloid and Interface Science*, vol. 336, no. 1, pp. 368–373, 2009.
- [85] R. J. Tian, J. M. Sun, H. Zhang et al., "Large-pore mesoporous SBA-15 silica particles with submicrometer size as stationary phases for high-speed CEC separation," *Electrophoresis*, vol. 27, no. 4, pp. 742–748, 2006.

- [86] Y. F. Zhu and J. L. Shi, "A mesoporous core-shell structure for pH-controlled storage and release of water-soluble drug," *Microporous and Mesoporous Materials*, vol. 103, no. 1-3, pp. 243-249, 2007.
- [87] D. C. Roux, J.-F. Berret, G. Porte, E. Peuvrel-Disdier, and P. Lindner, "Shear-induced orientations and textures of nematic wormlike micelles," *Macromolecules*, vol. 28, no. 5, pp. 1681-1687, 1995.
- [88] H. W. Hillhouse, T. Okudo, J. W. van Egmond, and M. Tsapatsis, "Preparation of supported mesoporous silica layers in a continuous flow cell," *Chemistry of Materials*, vol. 9, no. 7, pp. 1505-1507, 1997.
- [89] B. Tan, H.-J. Lehmler, S. M. Vyas, B. L. Knutson, and S. E. Rankin, "Fluorinated-surfactant-templated synthesis of hollow silica particles with a single layer of mesopores in their shells," *Advanced Materials*, vol. 17, no. 19, pp. 2368-2371, 2005.
- [90] C. I. Zoldesi, C. A. Van Walree, and A. Imhof, "Deformable hollow hybrid silica/siloxane colloids by emulsion templating," *Langmuir*, vol. 22, no. 9, pp. 4343-4352, 2006.
- [91] M. Fujiwara, K. Shiokawa, I. Sakakura, and Y. Nakahara, "Silica hollow spheres with nano-macroholes like diatomaceous earth," *Nano Letters*, vol. 6, no. 12, pp. 2925-2928, 2006.
- [92] A. Corma, "From microporous to mesoporous molecular sieve materials and their use in catalysis," *Chemical Reviews*, vol. 97, no. 6, pp. 2373-2419, 1997.
- [93] A. T. Bell, "The impact of nanoscience on heterogeneous catalysis," *Science*, vol. 299, no. 5613, pp. 1688-1691, 2003.
- [94] N. Ž. Knežević and J.-O. Durand, "Large pore mesoporous silica nanomaterials for application in delivery of biomolecules," *Nanoscale*, vol. 7, no. 6, pp. 2199-2209, 2015.
- [95] A. H. Janssen, P. van der Voort, A. J. Koster, and K. P. de Jong, "A 3D-TEM study of the shape of mesopores in SBA-15 and modified SBA-15 materials," *Chemical Communications*, vol. 15, pp. 1632-1633, 2002.
- [96] L. Cao, T. Man, and M. Kruk, "Synthesis of ultra-large-pore SBA-15 silica with two-dimensional hexagonal structure using triisopropylbenzene as micelle expander," *Chemistry of Materials*, vol. 21, no. 6, pp. 1144-1153, 2009.
- [97] T. P. B. Nguyen, J.-W. Lee, W. G. Shim, and H. Moon, "Synthesis of functionalized SBA-15 with ordered large pore size and its adsorption properties of BSA," *Microporous and Mesoporous Materials*, vol. 110, no. 2-3, pp. 560-569, 2008.
- [98] D. I. Fried, F. J. Brieler, and M. Fröba, "Designing inorganic porous materials for enzyme adsorption and applications in biocatalysis," *ChemCatChem*, vol. 5, no. 4, pp. 862-884, 2013.
- [99] R. J. Tian, H. Zhang, M. L. Ye et al., "Selective extraction of peptides from human plasma by highly ordered mesoporous silica particles for peptidome analysis," *Angewandte Chemie—International Edition*, vol. 46, no. 6, pp. 962-965, 2007.
- [100] S. M. L. dos Santos, K. A. B. Nogueira, M. D. S. Gama, J. D. F. Lima, I. J. da Silva Jr., and D. C. S. de Azevedo, "Synthesis and characterization of ordered mesoporous silica (SBA-15 and SBA-16) for adsorption of biomolecules," *Microporous and Mesoporous Materials*, vol. 180, pp. 284-292, 2013.
- [101] L. Y. Zhou, J. Fan, G. K. Cui et al., "Highly efficient and reversible CO₂ adsorption by amine-grafted platelet SBA-15 with expanded pore diameters and short mesochannels," *Green Chemistry*, vol. 16, no. 8, pp. 4009-4016, 2014.
- [102] J. Lee, C. Chen, and S. Cheng, "Adsorption of acid dyes by functionalized SBA-15 mesoporous silica of different pore lengths," *Journal of the Chinese Chemical Society*, vol. 62, no. 6, pp. 483-494, 2015.
- [103] K. Kosuge, S. Kubo, N. Kikukawa, and M. Takemori, "Effect of pore structure in mesoporous silicas on VOC dynamic adsorption/desorption performance," *Langmuir*, vol. 23, no. 6, pp. 3095-3102, 2007.
- [104] Y. T. Gong, Z. Z. Wei, J. Wang, P. F. Zhang, H. R. Li, and Y. Wang, "Design and fabrication of hierarchically porous carbon with a template-free method," *Scientific Reports*, vol. 4, article 6349, 2014.
- [105] Z. X. Yan, H. Meng, L. Shi, Z. H. Li, and P. K. Shen, "Synthesis of mesoporous hollow carbon hemispheres as highly efficient Pd electrocatalyst support for ethanol oxidation," *Electrochemistry Communications*, vol. 12, no. 5, pp. 689-692, 2010.
- [106] J. M. Sun, D. Ma, H. Zhang, X. H. Bao, G. Weinberg, and D. S. Su, "Macro-mesoporous silicas complex and the carbon replica," *Microporous and Mesoporous Materials*, vol. 100, no. 1-3, pp. 356-360, 2007.
- [107] J. M. Sun and X. H. Bao, "Textural manipulation of mesoporous materials for hosting of metallic nanocatalysts," *Chemistry—A European Journal*, vol. 14, no. 25, pp. 7478-7488, 2008.
- [108] E. Serrano, N. Linares, J. Garcia-Martinez, and J. R. Berenguer, "SolGel coordination chemistry: building catalysts from the bottom-up," *ChemCatChem*, vol. 5, no. 4, pp. 844-860, 2013.
- [109] H. D. Zhang, Y.-M. Wang, L. Zhang et al., "Enantioselective epoxidation of β -methylstyrene catalyzed by immobilized Mn(salen) catalysts in different mesoporous silica supports," *Journal of Catalysis*, vol. 256, no. 2, pp. 226-236, 2008.
- [110] G. Prieto, A. Martínez, R. Murciano, and M. A. Arribas, "Cobalt supported on morphologically tailored SBA-15 mesostructures: the impact of pore length on metal dispersion and catalytic activity in the Fischer-Tropsch synthesis," *Applied Catalysis A: General*, vol. 367, no. 1-2, pp. 149-159, 2009.
- [111] H. D. Zhang, Y. Zou, Y. Shen et al., "Dominated effect analysis of the channel size of silica support materials on the catalytic performance of immobilized lipase catalysts in the transformation of unrefined waste cooking oil to biodiesel," *BioEnergy Research*, vol. 7, no. 4, pp. 1541-1549, 2014.

Research Article

Effect of Mo-Doped Mesoporous Al-SSP Catalysts for the Catalytic Dehydration of Ethanol to Ethylene

Titinan Chanchuey, Chaowat Autthanit, and Bunjerd Jongsomjit

Center of Excellence on Catalysis and Catalytic Reaction Engineering, Department of Chemical Engineering, Faculty of Engineering, Chulalongkorn University, Bangkok 10330, Thailand

Correspondence should be addressed to Bunjerd Jongsomjit; bunjerd.j@chula.ac.th

Received 14 September 2015; Revised 14 December 2015; Accepted 3 January 2016

Academic Editor: Juan M. Coronado

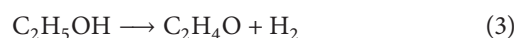
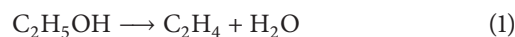
Copyright © 2016 Titinan Chanchuey et al. This is an open access article distributed under the Creative Commons Attribution License, which permits unrestricted use, distribution, and reproduction in any medium, provided the original work is properly cited.

The catalytic dehydration of ethanol to ethylene over the mesoporous Al-SSP and Mo-doped Al-SSP catalysts was investigated. The Al-SSP catalyst was first synthesized by the modified sol-gel method and then doped with Mo by impregnation to obtain 1% Mo/Al-SSP and 5% Mo/Al-SSP catalysts (1 and 5 wt% of Mo). The final catalysts were characterized using various techniques such as XRD, N_2 physisorption, SEM/EDX, TEM, and NH_3 -TPD. The catalytic activity for all catalysts in gas-phase ethanol dehydration reaction was determined at temperature range of 200°C to 400°C. It was found that the most crucial factor influencing the catalytic activities appears to be the acidity. The acid property of catalysts depended on the amount of Mo loading. Increased Mo loading in Al-SSP resulted in increased weak acid sites, which enhanced the catalytic activity. Besides acidity, the high concentration of Al at surface of catalyst is also essential to obtain high activity. Based on the results, the most suitable catalyst in this study is 1% Mo/Al-SSP catalyst, which can produce ethylene yield of ca. 90% at 300°C with slight amounts of diethyl ether (DEE) and acetaldehyde.

1. Introduction

Ethylene is an important feedstock for organic chemistry industry used in the preparation of polyethylene, ethylene oxide, vinyl chloride (from ethylene dichloride), and styrene (from ethyl benzene) [1]. Conventionally, it has been commercially produced by the thermal cracking of liquefied petroleum gas (LPG) or naphtha. According to the report by Kniel et al. [2], this method continues to dominate the industry today. True [3] reported the top ethylene producing complexes by capacity in tons per year, which are all steam cracking plants. In addition, Iles and Martin [4] reported the capacities of the Braskem and Solvay Indupa regarding ethanol to ethylene plants, while Voegle [5] reported the capacity of the Dow Chemical plant, which is currently under construction [3–5]. Compared to the conventional process, the catalytic dehydration of ethanol to ethylene is attractive because it requires lower temperature (less than 600°C) [6] and it is cleaner technology. Moreover, ethanol can be produced from renewable sources including nonedible source such as molasses. At present, SynDol catalyst based on $MgO-Al_2O_3/SiO_2$ developed by Halcon SD has been employed

commercially, achieving 99% of ethanol conversion and 95.83% of ethylene yield at 450°C [7]. Equate Petrochemical Company's plant (Kuwait) [3] achieved 99.7% of ethylene selectivity and 100% of ethanol conversion using nanoscale HZSM-5 as the catalyst. It is known that the acid catalysts used in ethanol dehydration normally consist of silica and alumina-based catalysts. Upon the catalytic dehydration of ethanol, ethylene and diethyl ether (DEE) can be obtained using a solid acid catalyst as follows:



The first reaction (1) has already been applied at the industrial level in the 1960s using aluminas as the catalysts [8]. The second reaction (2) occurs on the same catalysts under low temperature at moderate ethanol conversion, allowing very high selectivity and significant yields (>70%). In addition, acetaldehyde can be obtained by dehydrogenation of ethanol as seen in the third reaction (3). There are many works in

the literature related to the ethanol dehydration reaction over solid acid catalysts such as γ -alumina, zeolite, and silica-alumina [9, 10]. There are also research articles directed at obtaining molybdenum oxide over solid acid catalysts in various reactions, which require acid site for active site such as $\text{MoO}_3/\text{Al}_2\text{O}_3\text{-SiO}_2$ in light olefin metathesis or partial oxidation [11, 12] and $\text{MoO}_3/\text{Al}_2\text{O}_3$ in hydrodesulfurization of thiophene [13]. However, there are only a few works focused on molybdenum oxide for ethanol dehydration reaction. In continuation of our interest in using alumina and silica catalysts, the SiO_2 is suitable as a support due to its high surface area, uniform pore size, excellent mechanical strength, and thermal stability such as hexagonal mesoporous silica, that is, spherical silica particle (SSP) [14]. Alumina is a good support due to its high metal dispersion ability and excellent mechanical properties. Moreover, the metal oxide promotes acidity in catalyst, and then this is interesting. The molybdenum oxide can enhance acidity in the catalyst. Thus, it is interesting to use molybdenum oxide with the silica-alumina acid catalysts.

In this study, the mesoporous SSP was synthesized and modified with alumina to obtain Al-SSP catalyst. Then, Mo was doped onto the Al-SSP catalysts. The relevant characterization techniques such as XRD, SEM, EDX, TEM, and NH_3 -TPD were carried out to reveal the physical and chemical properties of catalysts. The ethanol dehydration reaction of catalysts was performed to determine the catalytic activity and product selectivity.

2. Materials and Methods

2.1. Materials. The chemicals used for preparation of the catalysts were tetraethyl orthosilicate (TEOS) (98%, Aldrich), cetyltrimethylammonium bromide (CTAB) (Aldrich), aluminium isopropoxide 98% [$\text{Al}(\text{OP}^i)_3$] (Aldrich), ammonia 30% (Panreac), isopropanol (Merck), and ammonium heptamolybdate-tetrahydrate (Merck). Gases employed were He (99.99%, Air Liquide), H_2 (99.999%, Air Liquide), N_2 (99.9999%, Air Liquide), synthetic air (99.99%, Air Liquide), and Ar (99.9%, Air Liquide).

2.2. Preparation of Catalysts

2.2.1. Synthesis of Al-SSP. First, the spherical silica particle (SSP) was synthesized following the method described by Janlamool et al. [14] with the mixture of 1 TEOS : 0.3 CTAB : 11 NH_3 : 58 Ethanol : 144 H_2O (molar ratio). The resulting suspension was stirred at room temperature for 2 h. After that, the white precipitate was separated from solvent by centrifuge. Then, the sample was dried at 110°C overnight and calcined in air at 550°C for 6 h to obtain the SSP support. In order to prepare Al-SSP, the SSP was added into the solution of aluminium isopropoxide in isopropanol (to obtain 60 wt% of Al). The mixture was stirred for 1 h at room temperature. Then, it was added into ammonia solution for hydrolysis. Then, the mixture was stirred at room temperature for 20 h. The Al-SSP catalyst was dried at 110°C for 24 h. The dried sample was calcined in air at 650°C for 2 h [15]. The surface

area of Al-SSP catalyst obtained was $443\text{ m}^2/\text{g}$ using N_2 physisorption technique.

2.2.2. Synthesis of Mo/Al-SSP. Mo/Al-SSP catalysts were prepared by impregnation of Mo precursor onto the Al-SSP obtained above. First, the desired amount of ammonium heptamolybdate-tetrahydrate was dissolved in DI water. Secondly, this solution was added into the Al-SSP. The Mo/Al-SSP catalyst was dried at 110°C for 4 h and calcined in air at 550°C for 4 h. The Mo-doped Al-SSP catalyst was denoted as X Mo/Al-SSP, where X (1 and 5 wt%) indicates the wt% of molybdenum.

2.3. Characterization of Catalysts. The bulk phase of catalyst was determined by SIEMENS D500 X-ray diffractometer (XRD), using CuK_α radiation with Ni filter in the 2θ range of $10\text{--}90$ degrees having the resolution of 0.02° .

The surface area and average pore volume of prepared catalysts were determined by N_2 -physisorption using Micromeritics Chemisorb 2750 Pulse instrument. Measurement was performed at -196°C and calculated according to the Brunauer, Emmet, and Teller (BET) isotherm equation.

The morphology and elemental distribution over the catalysts surface were determined by scanning electron microscope (SEM) and energy X-ray spectroscopy (EDX). The SEM model was JEOL mode JSM-5800LV and Link Isis series 300 program was performed for EDX.

The molybdenum particle dispersion of all catalysts was observed by using JEOL-JEM 200CX transmission electron microscope (TEM) operated at 200 kV.

The acidity of catalysts was estimated by temperature-programmed desorption of ammonia (NH_3 -TPD) using Micromeritics Chemisorb 2750 pulse chemisorption system. The catalyst sample was pretreated at 400°C in a flow of helium. The sample was saturated with 15% NH_3/He at 120°C for 1 h. After saturation, the physisorbed ammonia was desorbed in a helium gas flow. Then, the sample was heated from 40 to 800°C at a heating rate of $10^\circ\text{C}/\text{min}$. The amount of ammonia in effluent was measured via the thermal conductivity detector (TCD) as a function of temperature [16].

2.4. Ethanol Dehydration Reaction. Activity and product distribution via gas-phase ethanol dehydration reaction of catalysts were determined using a fixed-bed microreactor (I.D. = 7 mm and length = 0.33 m, made from a borosilicate glass tube). A glass reactor was placed into a temperature-programmed tubular furnace. All experiments were performed under atmospheric pressure and in the temperature range of 200 to 400°C using a feed composition consisting of 99.95% of ethanol. In this experiment, about 0.05 g of catalyst obtained from Sections 2.2.1 and 2.2.2 was charged into the middle zone of reactor tube and pure ethanol as feed was stored in vaporizer. Prior to testing, the catalyst was activated at 200°C for 1 h under argon. Ethanol was conveyed into reactor by argon gas flow rate of 50 mL/min. The reaction was carried out at each temperature for 1 h [17]. The reaction products were analyzed by gas chromatography using the

TABLE 1: Textural properties of the catalysts.

Catalysts	Surface area (m ² /g)	Average pore diameter (nm)	Average pore volume (cm ³ /g)
Al-SSP	443.6	5.9	0.81
1% Mo/Al-SSP	357.7	7.2	0.59
5% Mo/Al-SSP	492.4	3.9	0.58

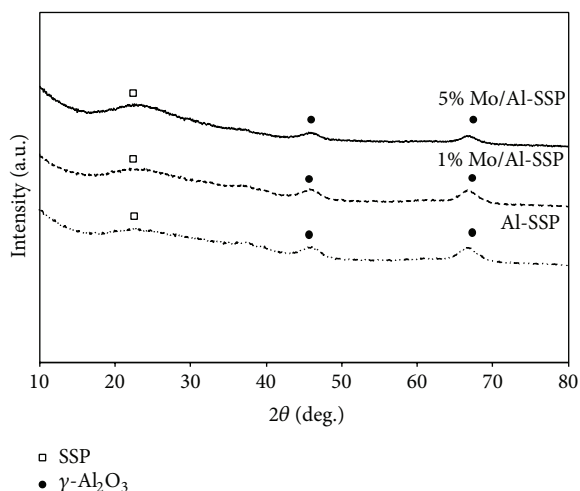


FIGURE 1: XRD patterns of all catalysts.

flame ionization detector (FID), Shimadzu GC14B equipping with DB-5 capillary column.

3. Results and Discussion

3.1. Characteristics of Catalyst. The Al-SSP, 1% Mo/Al-SSP, and 5% Mo/Al-SSP catalysts were characterized using various techniques. To identify the crystalline structure of the catalysts after Mo doping, the X-ray diffraction was performed. As shown in Figure 1, it can be observed that the Al-SSP catalyst exhibited the XRD peaks at 21–24° (broad) indicating the presence of amorphous structure of silica. Besides, the more sharp peaks around 45 and 67° were also observed for this sample indicating the presence of γ -Al₂O₃ crystallite [18]. However, after doping 1 and 5 wt% of Mo in Al-SSP, both Mo-doped Al-SSP catalysts still exhibited the similar XRD patterns as seen for those of Al-SSP. This revealed that the crystalline structure of the catalysts did not change with Mo doping. In addition, the Mo species cannot be detected because they are present in the highly dispersed form (the crystallite size is less than 3 nm).

The textural properties and nitrogen adsorption/desorption isotherms of the catalysts are summarized in Table 1 and Figure 2. According to the IUPAC classification, both support and catalysts exhibit Type IV isotherms, which are typical of mesoporous materials. For Al-SSP and 1% Mo/Al-SSP, the sample presented hysteresis loop of Type H1, occurring at higher relative pressure ($P/P_0 = 0.7$ to 0.9) compared to 5% Mo/Al-SSP catalyst. It indicates larger mesopores and broad pore size distribution with cylindrical

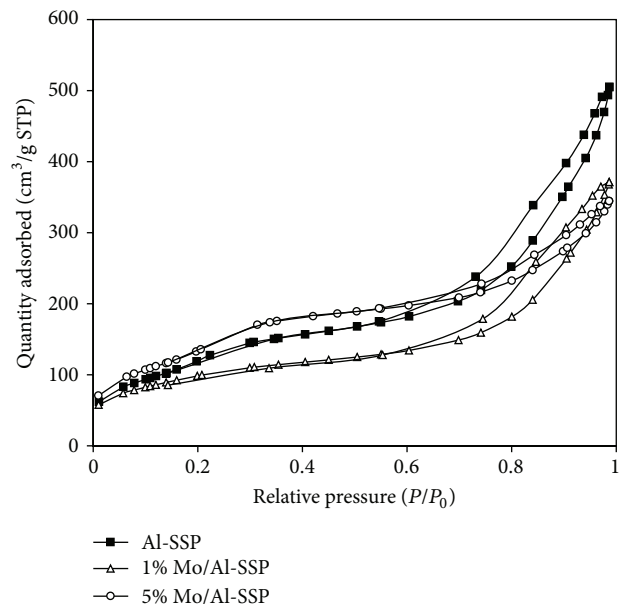


FIGURE 2: Nitrogen adsorption/desorption isotherms of all catalysts.

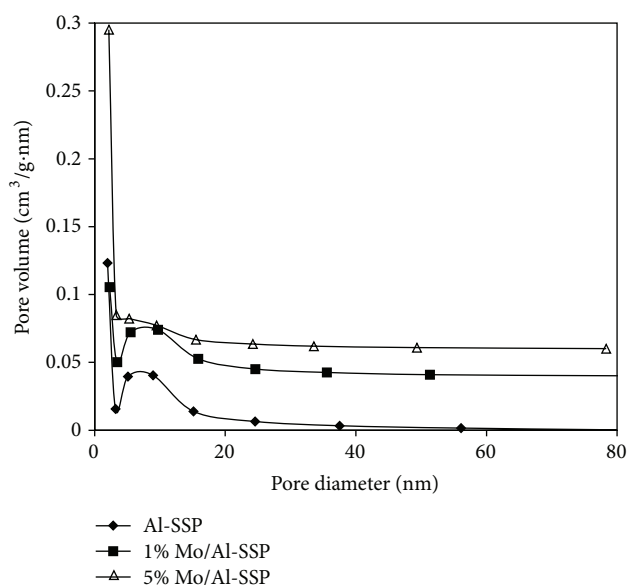


FIGURE 3: BJH pore size distribution of all catalysts.

shapes. The observation is consistent with the value of surface area and sample porosity as shown in Table 1, in which the pore volume of Al-SSP, 1% Mo/Al-SSP, and 5% Mo/Al-SSP was 0.81, 0.59, and 0.58 cm³/g, respectively. The incorporation of molybdenum into Al-SSP decreases the surface area, mainly due to the blockage of pore. Moreover, the pores of this catalyst were blocked, suggesting that the Mo at higher loading (>1 wt%) was not well dispersed in the supports. However, the surface area of 5 wt% Mo did not follow this trend. This may be because the Mo was located on the external surfaces indicating that Mo was not incorporated into the channels of Al-SSP leading to an increase in surface area. The pore size distribution (PSD) calculated by BJH method is shown in Figure 3. For all catalysts, the samples

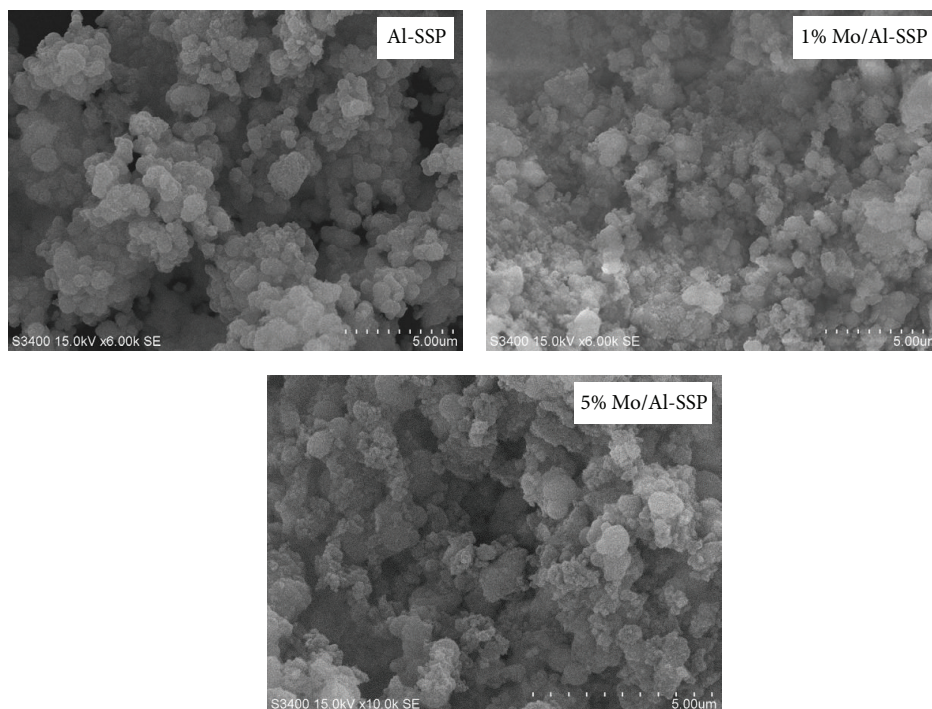


FIGURE 4: The SEM micrographs of all catalysts.

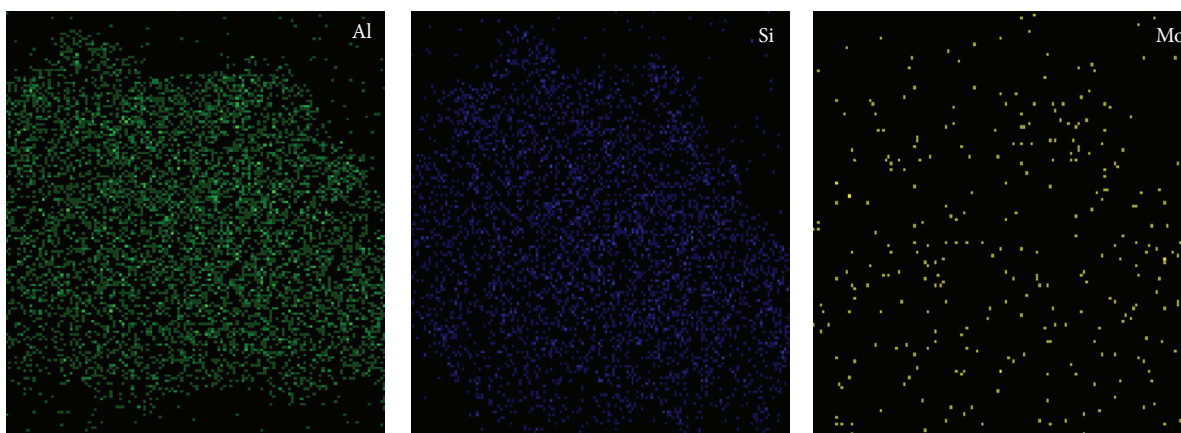


FIGURE 5: The typical EDX mapping of 1% Mo/Al-SSP catalyst.

have a narrow pore size distribution with an average pore diameter around 3.9–7.2 nm, confirming that the pore size distribution is in the mesoporous range. It can be seen that the calculated pore size distribution was in good agreement with N_2 isotherm as mentioned above.

The morphology of the catalysts was determined using SEM as shown in Figure 4. The morphology of the Al-SSP catalyst was apparently spheroidal with agglomeration of particles having the average particle size around 0.5 microns. After doping the Al-SSP with Mo, it can be seen that there was no significant change in the morphology of catalysts.

The dispersive X-ray spectroscopy (EDX) was also performed to determine the elemental distribution in the catalyst granule. All elements such as Al, Si, O, and Mo can be detected using the EDX mapping mode. Hence, the location of the specified element can be illustrated by the dots. The dense of dots is related to the amount of element present. The typical EDX mapping of 1% Mo/Al-SSP catalyst is shown in Figure 5. In this figure, the distribution of Al, Si, and Mo was observed. The density of Al and Si was strongly observed because Al and Si are the main components of Al-SSP catalyst. After Mo doping, the well distribution of Mo was evident. This result

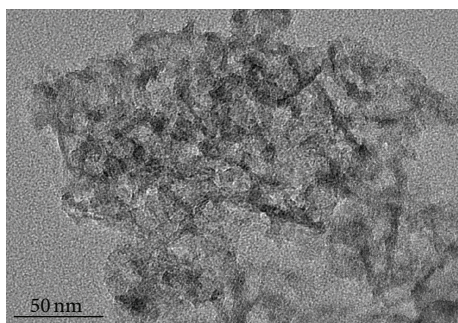


FIGURE 6: The typical TEM image of 1% Mo/Al-SSP catalyst.

TABLE 2: The amount of each element near the surface of catalyst granule obtained from EDX.

Catalysts	Amount of weight on surface (wt%)			
	Al	Si	O	Mo
Al-SSP	40.6	7.5	51.9	0
1% Mo/Al-SSP	27.2	18.5	49.9	4.4
5% Mo/Al-SSP	13.4	29.3	49.5	7.8

is in accordance with that obtained from XRD, where the Mo species are present in the highly dispersed form, which cannot be detected by the XRD measurement.

Besides the EDX mapping, the amount of each element near the surface of catalyst granule can be determined quantitatively. The results are summarized in Table 2. The key elements to be considered are Al and Mo. It can be seen that mostly Al species (Al = 27.2%) in 1% Mo/Al-SSP catalyst were located at the catalyst surface compared to that in 5% Mo/Al-SSP catalyst (Al = 13.4%). For both Mo-doped Al-SSP catalysts, Mo species were also located at the catalyst surface since the amounts of Mo obtained from EDX were larger than those of Mo loading. The location of Al species could play an important role on the catalytic activity as well.

In order to investigate the dispersion of Mo species, the transmission electron microscope (TEM) image was obtained as shown in Figure 6. It is known that gamma alumina is present as wrinkled sheets located throughout the SSP. As seen from the figure, the dark patches represent the Mo species being dispersed in the alumina wrinkled sheets. It was found that the dispersion of Mo species observed from TEM was corresponding to the very small crystallite size (less than 3 nm) of Mo species obtained from the XRD measurement as mentioned above.

The acid properties of catalysts are crucial to determine the catalytic activity and product distribution via ethanol dehydration reaction. Hence, the NH_3 temperature-programmed desorption (NH_3 -TPD) was performed. Table 3 shows the surface acidity of all catalysts in this study. The assignment of desorption peaks between 175 and 300°C is weak acid sites and the desorption peaks occurring above 300°C refer to medium-strong acid sites [19]. It indicates that the Al-SSP catalyst exhibits the lowest amount of weak acid

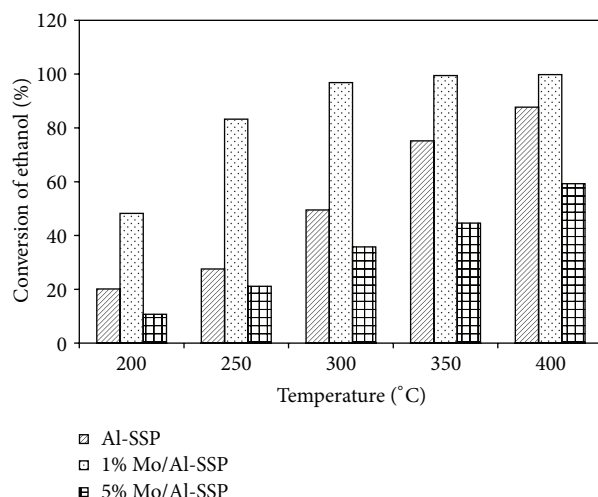


FIGURE 7: Ethanol conversion at different temperatures of all catalysts.

TABLE 3: The surface acidity of all catalysts from NH_3 -TPD.

Catalysts	Number of acid sites (mmole/g. cat)		
	Weak acid sites	Medium-strong acid sites	Total acid site
Al-SSP	0.25	1.45	1.70
1% Mo/Al-SSP	0.33	1.37	1.70
5% Mo/Al-SSP	0.78	1.11	1.99

site, whereas the 5% Mo/Al-SSP contains the largest weak and total acid sites. It can be observed that the Mo doping can alter the acidity of Al-SSP catalyst. Adding more amount of Mo apparently resulted in increased significant amount of weak acid site as seen in Table 3. It should be noted that the amount of weak acid site is probably more related to the Brønsted acid site, whereas Lewis acid site is more related to the amount of strong acid site [20]. In ethanol dehydration reaction, the Brønsted acid site is preferred.

3.2. Ethanol Dehydration Reaction. In order to measure the catalytic activity and product distribution, ethanol dehydration reaction was performed over all catalysts at atmospheric pressure with temperature ranging from 200 to 400°C. The results of ethanol conversion for all catalysts are shown in Figure 7. For all catalysts, increased temperature apparently resulted in an increase in ethanol conversion. However, among all catalysts, the 1% Mo/Al-SSP exhibits the highest conversion (ca. 100% conversion at 350°C). It can be observed that the ethanol conversion obtained from 5% Mo/Al-SSP catalyst is the lowest, although this catalyst has the highest amount of weak and total acid sites (Table 3). It should be noted that the amount of Al at catalyst surface for this sample is the lowest based on the EDX result (Table 2). Hence, this is probably the main reason for the 5% Mo/Al-SSP catalyst to yield the lowest conversion.

TABLE 4: Product yield obtained from ethanol dehydration at 300°C.

Catalysts	Yield of products (wt%)		
	Ethylene	Diethyl ether	Acetaldehyde
Al-SSP	49.07	0.00	0.44
1% Mo/Al-SSP	90.11	0.68	6.06
5% Mo/Al-SSP	29.25	1.09	5.45

Considering the product distribution, the selectivity of ethylene is related to the reaction temperature as also reported by Zhang et al. [21]. Ethylene selectivity is shown in Figure 8. For Al-SSP catalyst, ethylene selectivity was the highest even at low temperature, while it gradually increased for the Mo-doped Al-SSP catalysts with increased temperature. It is suggested that the Mo doping could result in decreased ethylene selectivity, especially at lower temperature. However, the effect of Mo doping is less pronounced at higher temperature.

It should be noted that, during ethanol dehydration, byproducts such as diethyl ether (DEE) and acetaldehyde were also obtained. The selectivity of byproduct is shown in Figure 9. At lower temperature (ca. 200 to 300°C), DEE was significantly produced via dehydration of ethanol. At temperature above 350°C, there was no DEE obtained due to its decomposition to ethylene at high temperature. Acetaldehyde is also produced by dehydrogenation of ethanol as a side reaction. As seen from the figure, increased temperature resulted in a slight decrease in selectivity of acetaldehyde, which was also reported by Nair et al. [22].

In order to compare the catalyst performance, the ethylene yield (product of conversion and selectivity) along with other byproducts obtained from ethanol dehydration at 300°C is calculated as shown in Table 4. It was found that the 1% Mo/Al-SSP catalyst rendered the highest ethylene yield with slight amounts of DEE and acetaldehyde. This is attributed to increased weak acid sites and large amount of Al present at the catalyst surface with 1 wt% of Mo doping onto Al-SSP catalyst.

Table 5 shows a comparison of the catalytic ability for ethanol dehydration to ethylene over various catalysts reported so far. It was obvious that 1% Mo/Al-SSP is competitive among other typical and modified catalysts. Finally, it should be emphasized that, apart from their interesting intrinsic activity, the Mo/Al-SSP tested in this study was highly stable, thus making them have potential for industrial applications.

4. Summary

Ethanol dehydration reaction from the temperature range of 200 to 400°C over Al-SSP, 1% Mo/Al-SSP, and 5% Mo/Al-SSP catalysts was investigated. It appears that the 1% Mo/Al-SSP catalyst exhibited the highest ethanol conversion and ethylene yield of ca. 90% (at 300°C). This can be attributed to the increased acidity and proper amount of Al at catalyst surface with Mo doping. However, too large amount of Mo

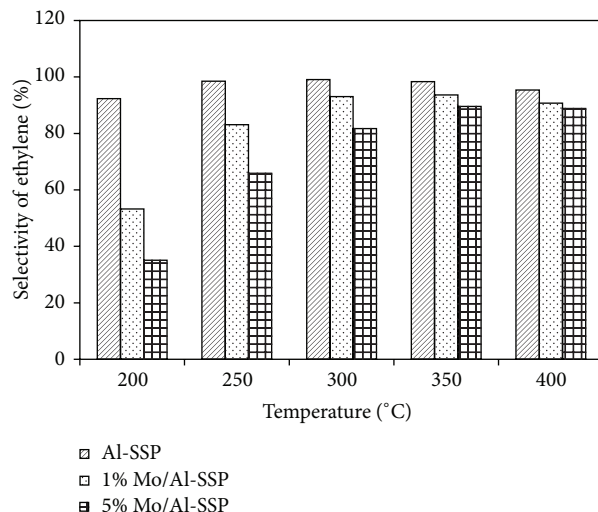


FIGURE 8: Ethylene selectivity at different temperatures of all catalysts.

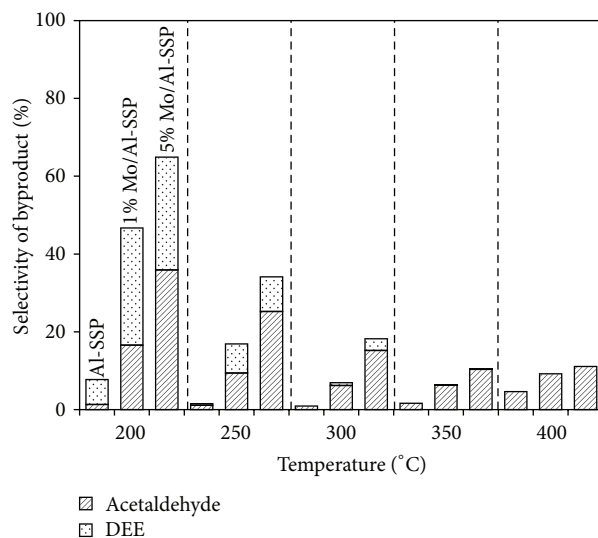


FIGURE 9: The selectivity of byproducts at different temperatures of all catalysts.

doping (i.e., 5 wt%) apparently resulted in decreased amount of Al at catalyst surface leading to low ethanol conversion.

Conflict of Interests

The authors declare that there is no conflict of interests regarding the publication of this paper.

Acknowledgments

The authors thank the Thailand Research Fund (BRG5780009 and IRG5780014), National Research University Project, Ratchadaphiseksomphot Endowment Fund (2015) of Chulalongkorn University (CU-58-027-AM), and the National

TABLE 5: A comparison of catalysts for ethylene synthesis and their catalytic ability.

Catalysts	Surface area (m ² /g)	Amount of catalyst	Reaction temperature (°C)	Space velocity (h ⁻¹)	Ethylene yield (wt%)	Ref.
1% Mo/Al-SSP	357.7	0.05 g	300	WHSV 8.4	90.11	This work
Al-SV	215	0.05 g	250–300	WHSV 8.4	53–100	[17]
MoO ₂	6	0.15 g	300	* n.a.	19.4	[23, 24]
0.5% La-2% P-HZSM-5	194	0.50 g	200–300	WHSV 2.0	10.2–99.9	[25]
TiO ₂ /γ-Al ₂ O ₃	187	1.15 mL	360–550	LHSV 26–104	91.99	[26]
Commercial Al ₂ O ₃	190	3.0 mL	450	LHSV 3.0	78.1	[21]

* n.a. = not applicable.

Research Council of Thailand (NRCT) for the financial support of this project.

References

- [1] D. Fan, D.-J. Dai, and H.-S. Wu, "Ethylene formation by catalytic dehydration of ethanol with industrial considerations," *Materials*, vol. 6, no. 1, pp. 101–115, 2013.
- [2] L. Kniel, O. Winter, and K. Stork, *Ethylene, Keystone to the Petrochemical Industry*, M. Dekker, New York, NY, USA, 1980.
- [3] W. R. True, "Global ethylene capacity continues to advance in 2011," December 2015, <http://www.ogj.com/articles/print/vol-110/issue-07/special-report-ethylene-report/global-ethylene-capacity.html>.
- [4] A. Iles and A. N. Martin, "Expanding bioplastics production: sustainable business innovation in the chemical industry," *Journal of Cleaner Production*, vol. 45, pp. 38–49, 2013.
- [5] E. Voegle, "Feeding the chemical market," *Ethanol Producer Magazine*, 2012, <http://www.ethanolproducer.com/articles/8617/feeding-the-chemical-market>.
- [6] T. K. Phung, L. Proietti Hernández, and G. Busca, "Conversion of ethanol over transition metal oxide catalysts: effect of tungsta addition on catalytic behaviour of titania and zirconia," *Applied Catalysis A: General*, vol. 489, pp. 180–187, 2014.
- [7] N. K. Kochar, R. Merims, and A. S. Padia, "Ethylene from ethanol," *Chemical Engineering Progress*, vol. 77, no. 6, pp. 66–70, 1981.
- [8] P. Imhof and J. C. van der Waal, *Catalytic Process Development for Renewable Materials*, Wiley-VCH, Weinheim, Germany, 2013.
- [9] I. Takahara, M. Saito, M. Inaba, and K. Murata, "Dehydration of ethanol into ethylene over solid acid catalysts," *Catalysis Letters*, vol. 105, no. 3–4, pp. 249–252, 2005.
- [10] J. Bedia, R. Barrionuevo, J. Rodríguez-Mirasol, and T. Cordero, "Ethanol dehydration to ethylene on acid carbon catalysts," *Applied Catalysis B: Environmental*, vol. 103, no. 3–4, pp. 302–310, 2011.
- [11] D. P. Debecker, B. Schimmoeller, M. Stoyanova et al., "Flame-made MoO₃/SiO₂-Al₂O₃ metathesis catalysts with highly dispersed and highly active molybdate species," *Journal of Catalysis*, vol. 277, no. 2, pp. 154–163, 2011.
- [12] D. P. Debecker, D. Hauwaert, M. Stoyanova, A. Barkschat, U. Rodemerck, and E. M. Gaigneaux, "Opposite effect of Al on the performances of MoO₃/SiO₂-Al₂O₃ catalysts in the metathesis and in the partial oxidation of propene," *Applied Catalysis A: General*, vol. 391, no. 1–2, pp. 78–85, 2011.
- [13] T. Kitano, S. Okazaki, T. Shishido, K. Teramura, and T. Tanaka, "Brønsted acid generation of alumina-supported molybdenum oxide calcined at high temperatures: characterization by acid-catalyzed reactions and spectroscopic methods," *Journal of Molecular Catalysis A: Chemical*, vol. 371, pp. 21–28, 2013.
- [14] J. Janlamool, P. Praserttham, and B. Jongsomjit, "Ti-Si composite oxide-supported cobalt catalysts for CO₂ hydrogenation," *Journal of Natural Gas Chemistry*, vol. 20, no. 5, pp. 558–564, 2011.
- [15] W. Phongsawat, B. Netiworaruksa, K. Suriye, S. Dokjampa, P. Praserttham, and J. Panpranot, "Role of support nature (γ-Al₂O₃ and SiO₂-Al₂O₃) on the performances of rhenium oxide catalysts in the metathesis of ethylene and 2-pentene," *Journal of Natural Gas Chemistry*, vol. 21, no. 2, pp. 158–164, 2012.
- [16] Z. Li, F. Meng, J. Ren, H. Zheng, and K. Xie, "Surface structure and catalytic performance of CuCl/SiO₂-Al₂O₃ catalysts for methanol oxidative carbonylation," *Chinese Journal of Catalysis*, vol. 29, no. 7, pp. 643–648, 2008.
- [17] M. Wannaborworn, P. Praserttham, and B. Jongsomjit, "A comparative study of solvothermal and sol-gel-derived nanocrystalline alumina catalysts for ethanol dehydration," *Journal of Nanomaterials*, vol. 2015, Article ID 519425, 11 pages, 2015.
- [18] F. F. Madeira, N. S. Gnep, P. Magnoux, S. Maury, and N. Cadran, "Ethanol transformation over HFAU, HBEA and HMFI zeolites presenting similar Bronsted acidity," *Applied Catalysis A: General*, vol. 367, no. 1–2, pp. 39–46, 2009.
- [19] J. Handzlik, J. Ogonowski, J. Stoch, M. Mikołajczyk, and P. Michorczyk, "Properties and metathesis activity of molybdena-alumina, molybdena-silica-alumina and molybdena-silica catalysts—a comparative study," *Applied Catalysis A: General*, vol. 312, no. 1–2, pp. 213–219, 2006.
- [20] J. A. Cecilia, C. García-Sancho, J. M. Mérida-Robles, J. Santamaría-González, R. Moreno-Tost, and P. Maireles-Torres, "V and V-P containing Zr-SBA-15 catalysts for dehydration of glycerol to acrolein," *Catalysis Today*, vol. 254, pp. 43–52, 2015.
- [21] X. Zhang, R. Wang, X. Yang, and F. Zhang, "Comparison of four catalysts in the catalytic dehydration of ethanol to ethylene," *Microporous and Mesoporous Materials*, vol. 116, no. 1–3, pp. 210–215, 2008.
- [22] H. Nair, J. E. Gatt, J. T. Miller, and C. D. Baertsch, "Mechanistic insights into the formation of acetaldehyde and diethyl ether from ethanol over supported VO_x, MoO_x, and WO_x catalysts," *Journal of Catalysis*, vol. 279, no. 1, pp. 144–154, 2011.

- [23] Y. Nakamura, T. Murayama, and W. Ueda, "Reduced vanadium and molybdenum oxides catalyze the equivalent formation of ethane and acetaldehyde from ethanol," *ChemCatChem*, vol. 6, no. 3, pp. 741–744, 2014.
- [24] Y. Nakamura, T. Murayama, and W. Ueda, "Hydrogen-transfer dehydration between alcohols over V_2O_3 and MoO_2 catalysts for the formation of corresponding alkanes and aldehydes," *Journal of Molecular Catalysis A: Chemical*, vol. 394, pp. 137–144, 2014.
- [25] N. Zhan, Y. Hu, H. Li, D. Yu, Y. Han, and H. Huang, "Lanthanum-phosphorous modified HZSM-5 catalysts in dehydration of ethanol to ethylene: a comparative analysis," *Catalysis Communications*, vol. 11, no. 7, pp. 633–637, 2010.
- [26] G. Chen, S. Li, F. Jiao, and Q. Yuan, "Catalytic dehydration of bioethanol to ethylene over $TiO_2/\gamma-Al_2O_3$ catalysts in microchannel reactors," *Catalysis Today*, vol. 125, no. 1-2, pp. 111–119, 2007.

Research Article

Preparation of Flower-Like Cu-WO₃ Nanostructures and Their Acetone Gas Sensing Performance

Hao Zhou, Dong-Yao Xu, Hai-Qing Zuo, Wei Liu, and Shuang Lin

School of Chemical & Environmental Engineering, China University of Mining and Technology (Beijing), Beijing 100083, China

Correspondence should be addressed to Dong-Yao Xu; xudongyao101@126.com

Received 7 September 2015; Revised 9 December 2015; Accepted 13 December 2015

Academic Editor: Amel Boudjema

Copyright © 2015 Hao Zhou et al. This is an open access article distributed under the Creative Commons Attribution License, which permits unrestricted use, distribution, and reproduction in any medium, provided the original work is properly cited.

Urchin-like Cu-W₁₈O₄₉ and flower-like Cu-WO₃ structures were successfully synthesized using a hydrothermal process followed by calcination. The synthesized products were characterized using XRD, SEM, and TEM. The results revealed that the as-prepared urchin-like and flower-like samples with monoclinic structures, which were approximately 1 μm and 1-2 μm, respectively, possessed microflower architecture assembled by the nanosheet. In addition, the gas sensing properties of monoclinic-structured Cu-WO₃ to acetone were measured using a static state gas sensing test system. The sensor based on the flower-like Cu-WO₃ nanostructures, which were calcined at 600°C, exhibited high sensitivity toward 10 ppm acetone at an optimum temperature of 110°C, and the maximum sensitivity reached 40, which was approximately four times higher than that of urchin-like WO₃ that was annealed at 300°C. The sensitivity was improved by increasing the acetone concentration. The detection limit was as low as 1 ppm. Using linear fit, the sensor was determined to be sufficiently sensitive to detect acetone in a detection range of 1 to 10 ppm even in the presence of interfering gases, which suggests that this type of sensor has excellent selectivity and has the potential for use in acetone gas sensors in the future.

1. Introduction

Tungsten oxide (WO₃) is a wide-band-gap ($E = 2.8$ eV) *n*-type semiconductor that has been widely used in gas detection sensors. In recent years, WO₃ has become the most promising semiconductor gas sensing material that has been used to detect NO_x, NH₃, CH₄, and H₂S [1–4]. This sensitive response toward gas, which is primarily due to variation in the resistance or optical properties caused by inner electrons, is highly dependent on the operating temperature. An increased operating temperature helps to improve the sensitivity of the WO₃ gas sensor to decrease the response and recovery time [5]. However, for single-component WO₃, some limitations, such as a high operating temperature and poor sensitivity, still exist which can prevent the extensive use of WO₃ based semiconductor gas sensors. Therefore, improvement in the sensor properties of these materials can be achieved by adding multicomponent materials (dopants), such as noble metals, transition metal oxides, and rare earth oxides. The introduction of dopants can be achieved in two primary ways. The first approach involves the introduction of impurity

atoms modified on oxide surface (surface modification) to produce active centers and interactions with test gas molecules, such as Ag, Au, and Pt [6]. The other approach involves the addition of foreign atoms into the crystal lattice of a semiconductor oxide (lattice doping), which results in generation of impurities within the semiconductor that alter in their electrical properties [7–9]. Currently, many methods have been employed for doping modifications including the impregnation method, the chemical vapor deposition method, the sputtering method, and the plasma method [10–12]. These methods have a high requirement for equipment and a high cost, and most of the doped metal elements can be washed away. Therefore, further improvement is necessary.

In this study, a hydrothermal method and subsequent calcination treatment had been utilized to synthesize urchin-like W₁₈O₄₉ and flower-like WO₃ structures with the addition of Cu(NO₃)₂ as a doping agent in the ethanol system. To simplify the reaction process, WC₁₆ was chosen as the tungsten source. The as-prepared samples were calcined at various temperatures, and their phase and morphology changes were characterized by X-ray diffraction analysis

(XRD), scanning electron microscopy (SEM), and transmission electron microscopy (TEM). Moreover, the gas sensing properties of monoclinic-structured Cu-WO₃ to acetone were measured using a static state system. In addition, the variation in the sensitivity as a function of the operating temperature and acetone concentration are discussed based on a gas-sensitive mechanism toward acetone. Finally, the selectivity to interfering gases was investigated. The purpose of this study was to extend the use of WO₃ based gas sensors for practical applications.

2. Materials and Methods

2.1. Chemicals. All of the chemical reagents were of analytic purity and used directly without further purification. WCl₆ was used as the tungsten source and purchased from the Aladdin Company. Ethanol (C₂H₅OH) and copper nitrate (Cu(NO₃)₂·3H₂O) were purchased from the Beijing Chemical Plant. Deionized water with a resistivity greater than approximately 7 Mohm was used for all of the experiments.

2.2. Experimental Process

2.2.1. Preparation of Flower-Like Cu-Doped WO₃. Flower-like copper-doped WO₃ was fabricated using a hydrothermal method. In a typical synthesis, 0.25 g of WCl₆ (as tungsten source) was dissolved in 60 mL of ethanol (C₂H₅OH, as solvent) followed by stirring until the solution was transparent and yellow. Subsequently, a suitable amount of copper nitrate (Cu(NO₃)₂·3H₂O, 3.0 wt%) was added to this solution under stirring. Then, the resulting solution was transferred to a 100 mL Teflon-lined stainless autoclave and heated at 180°C for 20 h in an electric oven. After cooling to room temperature, blue products were obtained by centrifugation and washed several times with deionized water and ethanol followed by drying at 60°C. Finally, the products were calcined in a muffle furnace with an air atmosphere at 300°C and 600°C for 2 h.

2.2.2. Gas Sensor Fabrication and Gas Sensing Performance Test. An appropriate amount of the as-prepared sample was mixed with a small amount of ethanol to form a paste. The paste was homogeneously coated onto a small alumina ceramic tube (obtained from Hui Sheng Electronic Technology Co., Ltd., Zhengzhou), and then, a Ni-Cr heating wire was inserted into the tube to form a gas sensor. The coated alumina ceramic tube was welded to a special hexagon pedestal with soldering to form the final sensor unit. To achieve stability, the fabricated sensor elements were aged in air for several days, and then, the gas sensing tests were performed. The corresponding transient response curve was developed [8, 13]. In this study, the sensor response value (*S*) was defined as follows: $S = R_a/R_g$, where *R_a* stands for the resistance of the gas sensors in air and *R_g* was the resistance of the gas sensors in the target gas.

2.3. Instrumentation. The morphology of the flower-like Cu-WO₃ samples was investigated using field-emission scanning

electron microscopy (SEM, Hitachi S-4500). The transmission electron microscopy (TEM) images were obtained on a JEOL JEM-2011. The crystal phase composition was determined using a RIGAKUD/MAX-Ra X-ray diffractometer with Cu Kα radiation ($\lambda = 0.15418$ nm). The XRD data were collected in a 2θ range of 10° to 80°. The gas sensing properties of the as-prepared flower-like structures were measured by a computer controlled WS-30A gas sensing measurement system (Hui Sheng Electronic Technology Co., Ltd., Zhengzhou).

3. Results and Discussion

3.1. Morphological Characterization of Flower-Like Cu-Doped WO₃. Figure 1 shows the XRD patterns of the Cu-WO₃ samples calcined at 300°C (a) and 600°C (b). As shown in Figure 1, the calcination temperatures have a significant influence on the crystal structure and growth. In the XRD pattern of the 3 wt% Cu-WO₃ sample calcined at 300°C (Figure 1(a)), all of the diffraction peaks can be easily indexed to the monoclinic W₁₈O₄₉ structure based on the standard diffraction peaks from JCPDS number 36-101 [6]. The two dominant peaks correspond to (010) and (020) lattice planes of Cu-WO₃. The diffraction peaks of the sample calcined at 300°C are consistent with those reported in the literature [14]. However, in the pattern for the sample annealed at 600°C, a monoclinic WO₃ structure formed due to recrystallization during heating. The main diffraction peaks are in good agreement with JCPDS number 72-0677 (lattice parameters: *a* = 7.306 Å, *b* = 7.540 Å, and *c* = 7.692 Å), which indicates that the monoclinic W₁₈O₄₉ structure was transferred to a monoclinic WO₃ structure during heating. To further investigate the morphology changes during the sintering process, the as-prepared samples have been studied using SEM and TEM, and the results are shown in Figure 2.

The SEM image in Figure 2(a) indicates that the Cu-WO₃ sample sintered at 300°C is approximately 1 μm in size and consists of an urchin-like structure. Similar morphologies have been reported by Xi et al. [6]. After calcination at 600°C, this structure is converted to a flower-like structure that is 1~2 μm in size and composed of many interconnected nanosheets, as shown in Figures 2(b) and 2(c). A coarse surface and a flower-like structure that was assembled from many approximately 100 nm thick nanosheets or nanosquares were observed. To elucidate the crystal structure changes, the as-synthesized samples were characterized by TEM. The TEM image indicates that the urchin-like morphology in Figure 2(a) becomes a nanosheet/nanosquare assembled flower-like morphology in Figure 2(d), which is consistent with the SEM result in Figure 2(c). Figure 2(e) shows a high-resolution transmission electron microscopy (HRTEM) image, and lattice fringes were observed with *d*-spacing of 0.389 nm, which is in agreement with the interplanar distances of (002) lattice planes of monoclinic WO₃ in the XRD data (Figure 1(b)) [15]. The corresponding selected area electron diffraction (SAED) pattern (Figure 2(f)) was recorded, and the results provided additional evidence of the single crystalline nature. After XRD analysis of

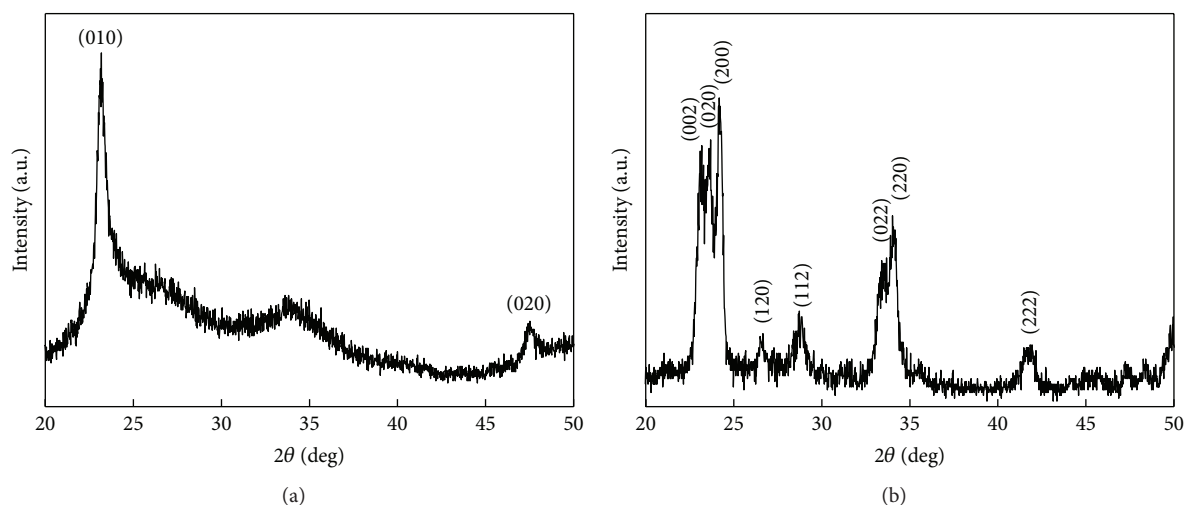


FIGURE 1: XRD pattern of the Cu-WO₃ samples calcined at different temperatures: (a) urchin-like Cu-doped W₁₈O₄₉ calcined at 300°C and (b) flower-like Cu-doped WO₃ calcined at 600°C.

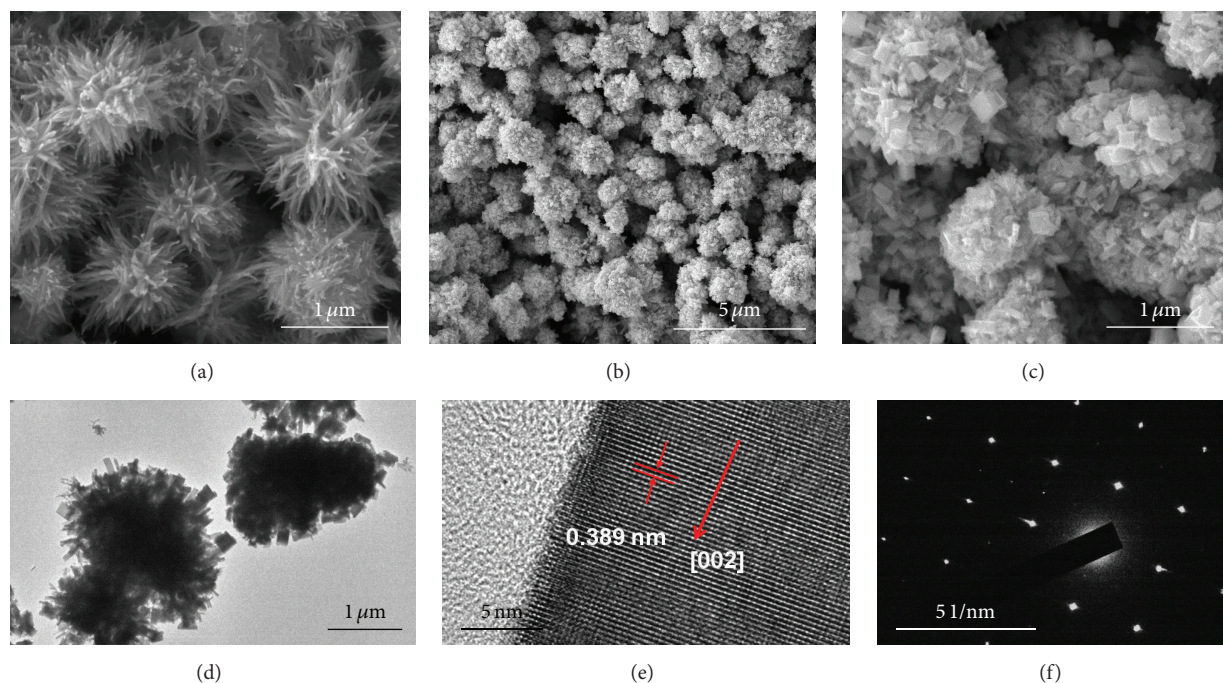


FIGURE 2: SEM images of Cu-doped tungsten oxide samples calcined at different temperatures. (a) SEM image of urchin-like Cu-doped W₁₈O₄₉ at 300°C. (b) SEM image of flower-like Cu-doped WO₃ at 600°C. (c) High-magnification image of (b). (d) TEM image of flower-like Cu-doped WO₃ at 600°C. (e) High-resolution TEM (HRTEM) image of the flower-like sample. (f) Selected area electron diffraction (SAED) pattern of the sample in (e).

the WO₃ sample doped with a small amount of copper, no characteristic peaks were observed. The Cu-WO₃ sample after calcination at 300°C, which has a monoclinic W₁₈O₄₉ structure in an urchin shape, has a strong surface effect due to a high specific surface area, oxygen vacancies, stacking faults, and other surface defects in the crystal structure [14]. In comparison to low-dimensional materials, the hierarchical micro/nanostructures that were self-assembled from low-dimensional nanomaterials provided a higher specific surface

area [16, 17], which is conducive to gas absorption and diffusion.

3.2. Gas Sensing Properties. The gas sensing performance of WO₃, which is a semiconductor metal oxide, is measured by the ratio of the resistance change of the sensor in air to that in the target gas. The sensitivity of the gas sensor is primarily affected by the operating temperature. Therefore, the gas sensing properties were investigated at different temperature

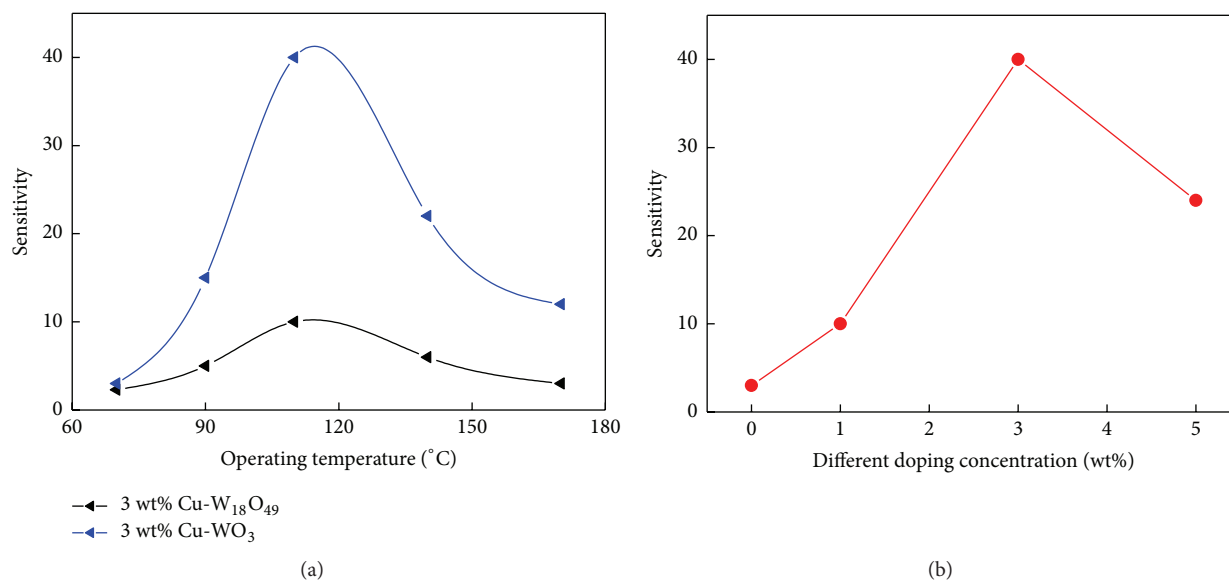


FIGURE 3: (a) Sensitivity of the Cu-doped W₁₈O₄₉ (black line) and WO₃ (blue line) sensor towards 10 ppm acetone under different operating conditions. (b) Different doping concentrations of copper in flower-like WO₃.

to determine the optimum operating conditions. We can also determine a suitable operational temperature range to improve the selectivity toward different target gases [18]. Figure 3(a) shows the sensitivity of the Cu-doped W₁₈O₄₉ and WO₃ gas sensors to 10 ppm acetone under different operating temperatures. The responses of the gas sensor increased continuously as the operating temperature increased, and a maximum was observed at 110°C followed by a decrease as the operating temperature further increased. A similar phenomenon was found in the urchin-like W₁₈O₄₉ sample. The maximum sensitivity reached 40 at an optimum working temperature of 110°C. Therefore, the operating temperature has an important influence on the sensitivity of the sensor, which is consistent with previous reports [5]. In general, when the operating temperature changes, the kinetics of adsorption and the chemical reactions occurring at the sensor surface are altered, leading to changes in the sensor sensitivity. However, if the temperature is further increased, the decrease in sensitivity after the maximum is considered to be primarily due to a decrease in the actual acetone concentration in the gas sensing region (vicinity of electrodes). The acetone molecules must migrate from the surface of the gas sensor to the gas sensing region inside. When the temperature is exceedingly high, the molecules tend to be consumed by oxidation during migration, and this tendency increased with increasing temperature. As shown in Figure 3(a), the sensor based on the flower-like Cu-WO₃ nanostructure (blue line) that was calcined at 600°C exhibited the highest sensitivity toward 10 ppm acetone at an optimum temperature of 110°C, and the sensitivity was 40, which is approximately four times higher than that of the urchin-like WO₃ (black) sample annealed at 300°C. This result is due to the sample after calcination at 600°C being more crystalline with suitable grain sizes during heating, which accounts for the excellent

sensitivity of the flower-like WO₃ sensor to acetone. In Figure 3(b), the different doping concentrations of copper in flower-like WO₃ are shown to determine the optimum doping concentration. The sensitivities of the 0 wt%, 1 wt%, and 5 wt% Cu-doped WO₃ samples were lower than that of the 3 wt% doped sample, suggesting that the optimum copper doping amount is 3 wt%.

In comparison to the WO₃ sensor without a doping agent [19], the acetone gas sensing properties of the Cu-doped WO₃ sensor were significantly improved. In general, the electrical conductivity can be altered by doping in an equivalent substance. This doped impurity, which is an electron receptor, provides electrons to the WO₃ conduction band and modifies the electronic structure of the metal oxides and carrier concentrations. In addition, the impurities have an important effect on the surface barrier of the materials [9]. As a result, the gas sensing properties of the materials can be enhanced. Moreover, a new phase of CuWO_{4-x} may be formed because Cu²⁺ (0.73 Å) can substitute for W⁶⁺ (0.62 Å) in the lattice cell of WO₃, which leads to a reduced electron concentration [20]. The direct exchange of electrons between the doped impurity and the gas sensing material can occur in the context of an electronic sensitization mechanism, resulting in changes in the material resistance. Therefore, the gas sensing performance will be improved. At the same time, doping can also change the defect equilibrium in the flower-like WO₃ structure, and crystal defects with high energy play an important role in oxygen and acetone adsorption on the surface of sensing materials as well as in the reactions of the gas molecules adsorbed on the material surface. Therefore, the obtained sample has a hierarchical structure consisting of a flower-like structure assembled from nanosheets or nanosquares (Figure 2(c) or Figure 2(d)) or an urchin-like structure with characteristics due to copper doping. All of

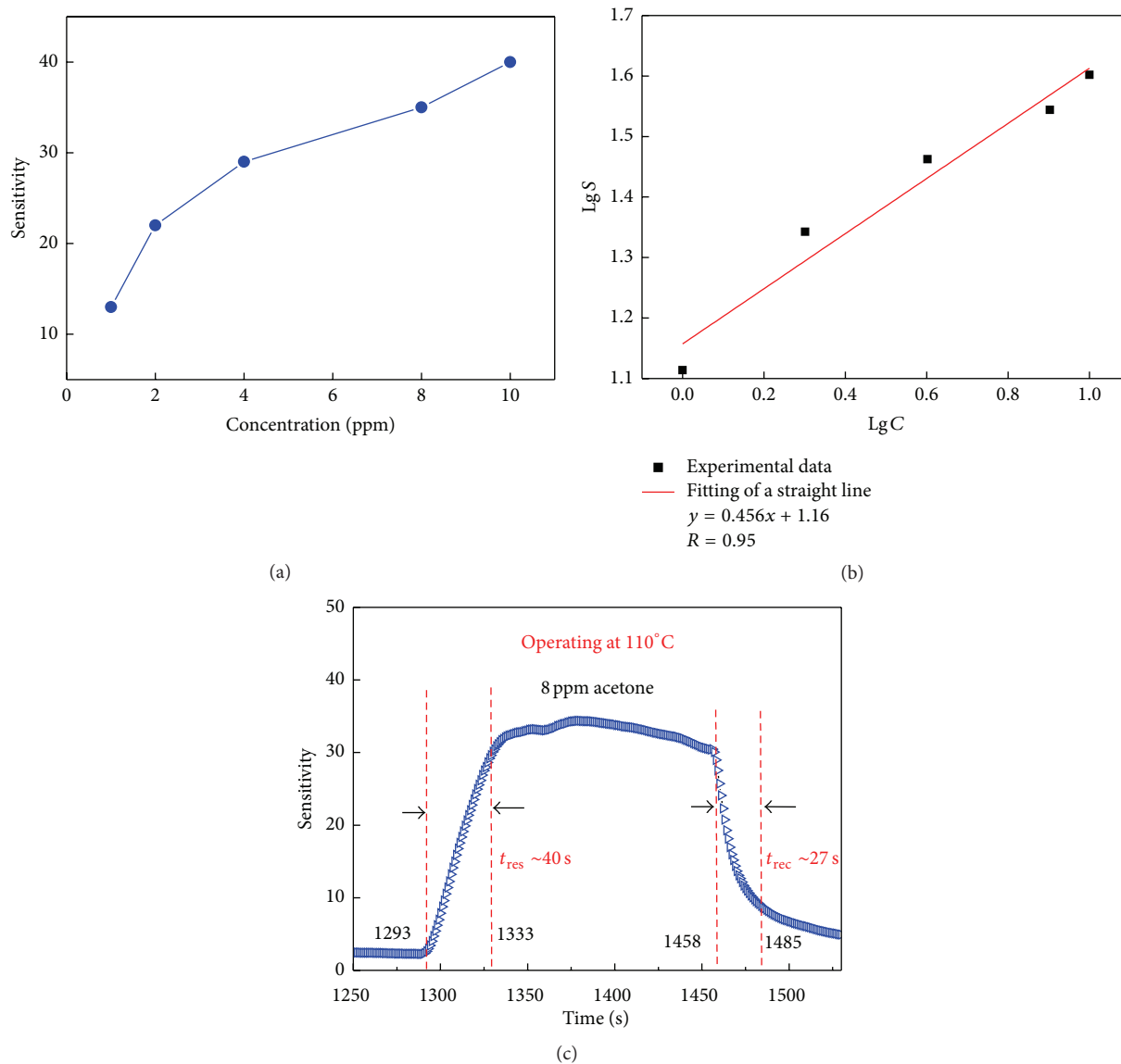


FIGURE 4: (a) Sensitivity of flower-shaped WO_3 to different concentrations of acetone at 110°C . (b) Logarithmic linear fitting of sensibility and concentration. (c) Response (t_{res}) and recovery (t_{rec}) time measured from the response-time data to 8 ppm acetone at an operating temperature of 110°C .

these factors are important for achieving a high response to the target gas. More detailed factors should be further investigated.

Figure 4 shows the sensitivity of the flower-like WO_3 based gas sensor to different acetone concentrations at 110°C . The sensitivity increased as the acetone concentration increased. According to previous studies [21], the sensitivity (S) of a semiconducting oxide gas-sensitive sensor can be empirically represented as $S = 1 + A_g(P_g)^b$, where A_g denotes the prefactor, P_g is the target gas partial pressure, which is directly proportional to its gas concentration, and b is the exponent on P_g . Accordingly, the logarithm of S can be linear as a function of the gas concentration (C). b may have some rational fraction value (typically 1 or 0.5) depending on the charge of the surface species and the stoichiometry

of the elementary reactions on the surface [13, 22]. Based on this theory, a logarithm was used to fit the experiment data (i.e., the sensitivity values corresponding to different acetone concentrations at an optimum working temperature of 110°C). Then, a linear relationship between $\text{Lg}S$ and $\text{Lg}C$ was established by linear fitting. The fit curve of $\text{Lg}(S)$ as a function of $\text{Lg}(C)$ is shown in the inset of Figure 4. The correlation coefficient (R) of the acetone sensor was 0.95 in the range of 1 to 10 ppm at an operating temperature of 110°C . The value of b towards acetone is approximately 0.456, which approaches the ideal value of 0.5. Therefore, little difference was observed between the measured value and the theoretical value. As shown in Figure 4(c), the response (t_{res}) and recovery (t_{rec}) times were approximately 40 s and 27 s, respectively, which was measured from the response-time

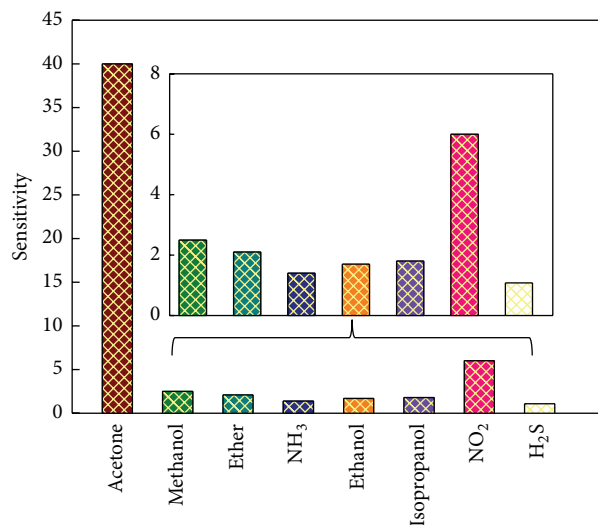


FIGURE 5: Responses of the flower-like Cu-WO₃ gas sensor to different gases at 110°C.

data to 8 ppm acetone at an operating temperature of 110°C. These data demonstrate that the gas sensors based on flower-like Cu-WO₃ are sufficiently sensitive to detect acetone in a range from 1 ppm to 10 ppm.

Practical applications require that gas sensing materials have a high sensitivity and quick response to the target gas. Therefore, the selectivity is regarded as the main factor for evaluating the gas sensing characteristics. Figure 5 shows the responses of a flower-like Cu-WO₃ gas sensor to 10 ppm acetone, methanol, ether, NH₃, ethanol, isopropanol, NO₂, and H₂S at 110°C, respectively. The response of the Cu-WO₃ gas sensor to 10 ppm acetone was 40, which is much larger than that to other interference gases. The response to the other seven target gases varies from 1.08 to 6. In addition, the ratio of the Cu-WO₃ sensor response of acetone to that of the other five target gases ranged from 6.6 to 37. Therefore, the flower-like Cu-WO₃ gas sensor has good selectivity to acetone at 110°C in the presence of the previously mentioned interfering gases.

4. Conclusions

In summary, monoclinic urchin-like and flower-like Cu-WO₃ structures were synthesized using a hydrothermal process followed by calcination. The crystallography and microstructure of the synthesized samples were characterized using XRD, SEM, and TEM. Then, the acetone sensing properties were investigated. The results indicate that the optimum operating temperature for the detection of acetone was 110°C. At this temperature, the response of the sensor based on flower-like Cu-WO₃ nanostructures that were calcined at 600°C was 40 when exposed to 10 ppm acetone, which is approximately four times higher than that of the urchin-like WO₃ sample annealed at 300°C. The sensitivity increased as the acetone concentration increased. The lowest detection limit was 1 ppm. The sensor was determined to be sufficiently sensitive to detect acetone in a range from 1 to 10 ppm even

in the presence of interfering gases. The flower-like Cu-WO₃ material has the potential for use in a practical acetone gas sensor in the future.

Conflict of Interests

The authors declare that there is no conflict of interests regarding the publication of this paper.

References

- [1] C. López-Gándara, J. M. Fernández-Sanjuán, F. M. Ramos, and A. Cirera, "Role of nanostructured WO₃ in ion-conducting sensors for the detection of NO_x in exhaust gases from lean combustion engines," *Solid State Ionics*, vol. 184, no. 1, pp. 83–87, 2011.
- [2] X. Wang, N. Miura, and N. Yamazoe, "Study of WO₃-based sensing materials for NH₃ and NO detection," *Sensors and Actuators B: Chemical*, vol. 66, no. 1–3, pp. 74–76, 2000.
- [3] A. Hameed, I. M. I. Ismail, M. Aslam, and M. A. Gondal, "Photocatalytic conversion of methane into methanol: performance of silver impregnated WO₃," *Applied Catalysis A: General*, vol. 470, pp. 327–335, 2014.
- [4] I. M. Szilágyi, S. Saukko, J. Mizsei, A. L. Tóth, J. Madarász, and G. Pokol, "Gas sensing selectivity of hexagonal and monoclinic WO₃ to H₂S," *Solid State Sciences*, vol. 12, no. 11, pp. 1857–1860, 2010.
- [5] S. Bai, K. Zhang, R. Luo, D. Li, A. Chen, and C. C. Liu, "Low-temperature hydrothermal synthesis of WO₃ nanorods and their sensing properties for NO₂," *Journal of Materials Chemistry*, vol. 22, no. 25, pp. 12643–12650, 2012.
- [6] G. Xi, J. Ye, Q. Ma, N. Su, H. Bai, and C. Wang, "In situ growth of metal particles on 3D urchin-like WO₃ nanostructures," *Journal of the American Chemical Society*, vol. 134, no. 15, pp. 6508–6511, 2012.
- [7] N. Yamazoe, "New approaches for improving semiconductor gas sensors," *Sensors and Actuators B: Chemical*, vol. 5, no. 1–4, pp. 7–19, 1991.
- [8] S. Bai, C. Chen, D. Zhang et al., "Intrinsic characteristic and mechanism in enhancing H₂S sensing of Cd-doped α -MoO₃ nanobelts," *Sensors and Actuators B: Chemical*, vol. 204, pp. 754–762, 2014.
- [9] W. Wang, *Research on Surface Doped Tungsten Oxide Gas-Sensing Mechanism*, Tianjin University, TanJin, China, 2011.
- [10] N.-E. Sung, I.-J. Lee, A. Thakur, K. H. Chae, H.-J. Shin, and H.-K. Lee, "Properties of Cu-doped ZnO films by RF sputtering method: thickness dependence," *Materials Research Bulletin*, vol. 47, no. 10, pp. 2891–2894, 2012.
- [11] F.-H. Wang, H.-P. Chang, C.-C. Tseng, C.-C. Huang, and H.-W. Liu, "Influence of hydrogen plasma treatment on Al-doped ZnO thin films for amorphous silicon thin film solar cells," *Current Applied Physics*, vol. 11, supplement, no. 1, pp. S12–S16, 2011.
- [12] Y. Zheng, C. Chen, Y. Zhan et al., "Photocatalytic activity of Ag/ZnO heterostructure nanocatalyst: correlation between structure and property," *The Journal of Physical Chemistry C*, vol. 112, no. 29, pp. 10773–10777, 2008.
- [13] S. Bai, T. Guo, D. Li, R. Luo, A. Chen, and C. C. Liu, "Intrinsic sensing properties of the flower-like ZnO nanostructures," *Sensors and Actuators B: Chemical*, vol. 182, pp. 747–754, 2013.
- [14] Y.-X. Qin, K.-X. Liu, C.-Y. Liu, and X.-B. Sun, "P-type conductivity and NO₂ sensing properties for V-doped W₁₈O₄₉

- nanowires at room temperature,” *Acta Physica Sinica*, vol. 62, no. 20, Article ID 208104, pp. 1–7, 2013.
- [15] D.-D. Qin, C.-L. Tao, S. A. Friesen et al., “Dense layers of vertically oriented WO_3 crystals as anodes for photoelectrochemical water oxidation,” *Chemical Communications*, vol. 48, no. 5, pp. 729–731, 2012.
- [16] J.-H. Lee, “Gas sensors using hierarchical and hollow oxide nanostructures: overview,” *Sensors and Actuators B: Chemical*, vol. 140, no. 1, pp. 319–336, 2009.
- [17] H.-J. Kim, J.-W. Yoon, K.-I. Choi, H. W. Jang, A. Umar, and J.-H. Lee, “Ultrasensitive and sensitive detection of xylene and toluene for monitoring indoor air pollution using Cr-doped NiO hierarchical nanostructures,” *Nanoscale*, vol. 5, no. 15, pp. 7066–7073, 2013.
- [18] A. Phuruangrat, D. J. Ham, S. J. Hong, S. Thongtem, and J. S. Lee, “Synthesis of hexagonal WO_3 nanowires by microwave-assisted hydrothermal method and their electrocatalytic activities for hydrogen evolution reaction,” *Journal of Materials Chemistry*, vol. 20, no. 9, pp. 1683–1690, 2010.
- [19] Z. Wang, P. Sun, T. Yang et al., “Flower-like WO_3 architectures synthesized via a microwave-assisted method and their gas sensing properties,” *Sensors and Actuators B: Chemical*, vol. 186, pp. 734–740, 2013.
- [20] X. Bai, H. Ji, P. Gao, Y. Zhang, and X. Sun, “Morphology, phase structure and acetone sensitive properties of copper-doped tungsten oxide sensors,” *Sensors and Actuators, B: Chemical*, vol. 193, pp. 100–106, 2014.
- [21] I.-D. Kim, A. Rothschild, T. Hyodo, and H. L. Tuller, “Microsphere templating as means of enhancing surface activity and gas sensitivity of $\text{CaCu}_3\text{Ti}_4\text{O}_{12}$ thin films,” *Nano Letters*, vol. 6, no. 2, pp. 193–198, 2006.
- [22] R. W. J. Scott, S. M. Yang, G. Chabanis, N. Coombs, D. E. Williams, and G. A. Ozin, “Tin dioxide opals and inverted opals: near-ideal microstructures for gas sensors,” *Advanced Materials*, vol. 13, no. 19, pp. 1468–1472, 2001.

Review Article

Functionalized Mesoporous Silica Membranes for CO₂ Separation Applications

**Hyung-Ju Kim, Hee-Chul Yang, Dong-Yong Chung, In-Hwan Yang,
Yun Jung Choi, and Jei-kwon Moon**

Korea Atomic Energy Research Institute, 989-111 Daedeok-daero, Yuseong-gu, Daejeon 305-353, Republic of Korea

Correspondence should be addressed to Hyung-Ju Kim; hyungjukim@kaeri.re.kr

Received 2 October 2015; Accepted 10 November 2015

Academic Editor: Juan M. Coronado

Copyright © 2015 Hyung-Ju Kim et al. This is an open access article distributed under the Creative Commons Attribution License, which permits unrestricted use, distribution, and reproduction in any medium, provided the original work is properly cited.

Mesoporous silica molecular sieves are emerging candidates for a number of potential applications involving adsorption and molecular transport due to their large surface areas, high pore volumes, and tunable pore sizes. Recently, several research groups have investigated the potential of functionalized mesoporous silica molecular sieves as advanced materials in separation devices, such as membranes. In particular, mesoporous silica with a two- or three-dimensional pore structure is one of the most promising types of molecular sieve materials for gas separation membranes. However, several important challenges must first be addressed regarding the successful fabrication of mesoporous silica membranes. First, a novel, high throughput process for the fabrication of continuous and defect-free mesoporous silica membranes is required. Second, functionalization of mesopores on membranes is desirable in order to impart selective properties. Finally, the separation characteristics and performance of functionalized mesoporous silica membranes must be further investigated. Herein, the synthesis, characterization, and applications of mesoporous silica membranes and functionalized mesoporous silica membranes are reviewed with a focus on CO₂ separation.

1. Introduction

To overcome the increasing challenges posed by the need for new energy sources and environmental protection, advanced molecular separation and purification technologies are required. Absorption [1], adsorption [2, 3], membrane separation [4], and capture [5] technologies are currently available to address these challenges. Among them, membrane-based separations are becoming increasingly relevant for a number of applications due to their low energy requirements and steady-state operations [6–9]. Membrane-based separation is applicable not only to liquids but also to gases. Membranes are widely used in desalination industry and for other industrial purposes such as wastewater treatment [10] and recovery of valuable organic matter [11]. Membrane separation can be further classified into pervaporation [12], microfiltration, ultrafiltration [13], nanofiltration [14], reverse osmosis [15], and forward osmosis [15] depending on the manner of membrane operation and its pore range. In gas separation, natural gas sweetening, that is, removal of CO₂ and H₂S from

hydrocarbons [16], and CO₂ separation in a coal-fired power plant [17] are the most important processes. Additionally, membrane separation is used to induce separation between electrodes in battery-related applications [18].

With the large specific surface areas, high pore volumes, tunable pore sizes, and stability, mesoporous silica is decent candidate as membrane material for separation applications [19]. Its uniform pore structures and high silanol group densities also make it attractive for separation and purification applications [20]. Silanol groups are important for using silica as versatile support after modification.

Mesoporous materials are typically formed using a micelle-templating process, following either an electrostatically driven cooperative assembly pathway or a nonionic route in the presence of uncharged surfactants as structure-directing agents. M41S was the first reported ordered mesoporous silica material [21]. Emerging applications in catalysis, adsorption, and separation have boosted the development of many other ordered mesoporous silica materials, such as the SBA-n [22, 23], Fudan University Material (FDU) [24],

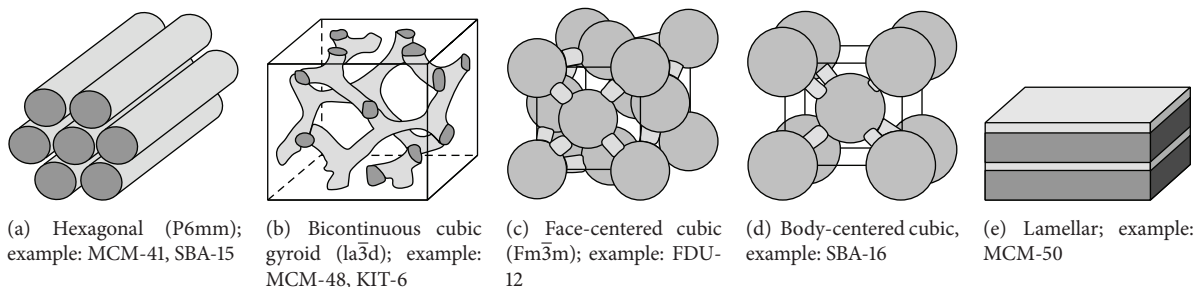


FIGURE 1: Structures of various ordered mesoporous materials [27].

Korea Advanced Institute of Science and Technology (KIT) [25], and anionic-surfactant-templated mesoporous silica (AMS) [26] families. Many of these mesoporous materials (see Figure 1) have been explored for separation applications [27].

A number of studies on the adsorption uptake of acidic gases such as CO_2 by mesoporous silica molecular sieves have been reported [27, 28]. Mesoporous silica, such as SBA-15 [29], MCM-41 [30], and MCM-48 [31], were shown to be good supports for separation membranes, offering selectivity over other gases such as CH_4 and N_2 . Since gas separation is derived from transport phenomena and mesostructures are a framework of gas transport, a 3D structure with interconnected pores is highly preferred to overcome the limitation of diffusion. Modification of these molecular sieves with organic groups is required to tailor their specific sorption capacities [32]. Thus, effective methods for the fabrication of mesoporous silica membranes and their functionalization with appropriate modification agents are crucial for advancing their practical application. Herein, amine-functionalized mesoporous silica membranes and their use for CO_2 gas separation are discussed.

2. Functionalized Silica Membranes

2.1. Mesoporous Silica Membranes. Adapting mesoporous silica molecular sieve powders to a membrane configuration while preserving their adsorptive properties presents an attractive but challenging possibility for developing separation processes. For instance, mesoporous silica in a membrane configuration allows gas separation under steady-state conditions, wherein selective adsorption occurs on the feed side, followed by selective diffusion across the membrane with continuous desorption on the permeate side. Specifically for CO_2 separation, the CO_2 molecules are chemisorbed on the active layer of the membrane (in the pores), diffused through the pores of the membrane, and then desorbed from the other side of the membrane [27]. At the same time, other gases are retained by the membrane layer. Figure 2 shows a schematic of such transport at the molecular level. Because mesoporous silica molecular sieves do not have mechanical strength, various macroporous supports, including ceramics and polymers, are necessary. These support materials do not function as barriers; only the mesoporous silica membrane layer acts as a bottleneck for the transport process. Thus,

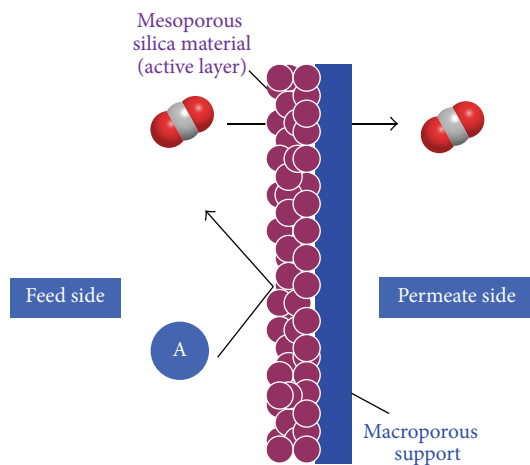


FIGURE 2: Schematic of transport at the molecular level through a supported asymmetric mesoporous silica membrane. CO_2 is the permeating gas, and A is the retentate gas molecule.

mesoporous materials in the form of thin films on supports (asymmetric membranes) may offer a number of advantages in many emerging applications [33]. Such membranes act as barriers to the mass transfer between phases, allowing the separation of the phases under a driving force. Previously, thin layers of mesoporous silica membranes have been grown on ceramic supports such as α -alumina [34, 35] to increase their mechanical stability [36]. Both disk and tubular configurations are possible. However, compared with the formation of disk-type membranes, the deposition of mesoporous silica membranes on tubular α -alumina supports is challenging due to the nucleation and growth behavior that occurs on curved surfaces. On the other hand, the tubular form guarantees a high packing density with a large surface area. Recently, mesoporous silica membranes were successfully synthesized on polymeric hollow fiber supports for more versatile applications. It is possible to fabricate much thinner (μm level) polymeric hollow fibers than tubular ceramic supports (mm level), and thus significantly higher packing densities and larger surface areas per module can be achieved. In addition, polymer-based supports are generally cheaper than ceramic materials and highly reproducible. One disadvantage of polymeric supports compared with ceramic supports is their limited thermal stability, which prevents

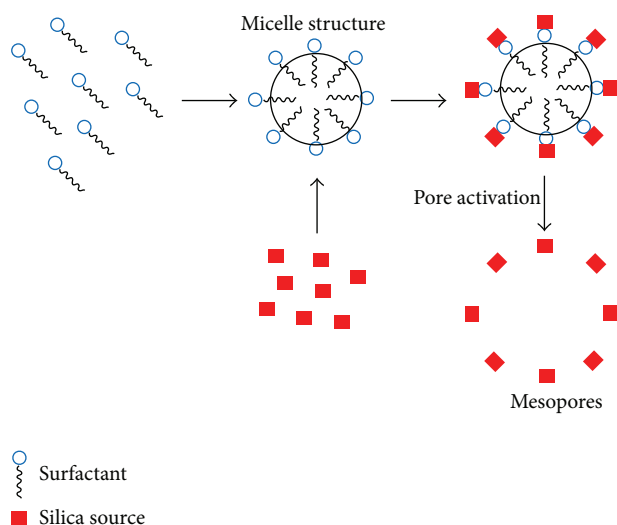


FIGURE 3: Mechanism for the synthesis of mesoporous silica in the presence of a cationic surfactant.

the use of high-temperature surfactant removal processes, particularly calcination. Thus, there are pros and cons for each type of support that must be considered when selecting the appropriate support material for a specific application.

Supported mesoporous silica membranes with controlled structures, like silica powder, are synthesized via the well-established sol-gel method but in the presence of support materials. This technique involves hydrolysis and condensation of respective precursors to form colloidal sols [27]. Figure 3 shows the mechanism for the synthesis of mesoporous silica in the presence of a cationic surfactant. When dissolved in water, the cationic surfactant forms micelle structures. In this process, the cationic “heads” of the surfactant molecules are arranged to the outer side, while their hydrophobic “tails” collect in the center of each micelle. The silica source then covers the micelle surfaces. Once the surfactant is removed via calcination or extraction, the pores are activated.

Pretreatment of the supports using several different methods has been attempted to improve the quality of the membranes. Polishing of ceramic supports provides even surfaces that afford more reproducible membranes. Seed layer deposition has also been shown to result in smoother surfaces and increase the chance of nucleation that influences membrane growth.

Synthesized mesoporous silica membranes can be characterized using various techniques. The most important property of membranes is a defect-free and continuous layer. To monitor the top surfaces and cross sections of membranes, scanning electron microscopy (SEM) is employed. Accurate determination of the membrane thickness, which is an important variable for calculating the gas permeability, is obtained via SEM coupled with energy-dispersive X-ray spectroscopy (EDS) (see Figure 4). To avoid rupture of the silica layer and silica/support interface, treatment with liquid nitrogen is generally performed first to preserve the membrane layer for proper observation. Unlike mesoporous silica

powders, however, other properties of mesoporous silica membranes are not easily characterized and investigated. Thus, numerous efforts are underway to obtain the same information that can be gathered for silica powders. For instance, N_2 physisorption analysis is used to directly investigate the pore structure of silica powders, but this technique is quite limited for supported mesoporous silica membranes due to the presence of the support and the small quantity of membrane. As an alternative, a nondestructive, reusable N_2 physisorption method was developed as a lab-made apparatus for supported inorganic membranes [37]. This method was used to determine the direct pore structure of supported mesoporous silica membranes, and the results were compared with those obtained for powder samples of zeolite [38] and mesoporous silica [39] membranes. Depending on the thickness of membrane, this method requires around 10 consistent membranes. If the membranes are varied, obtained data have low reliability. To reduce the needed sample quantity and other artifacts, a more advanced technique is required for future research.

2.2. Functionalization of Mesoporous Silica Membranes. The typical pore sizes (2 to 50 nm) of mesoporous silica membranes preclude direct application in molecular separations involving small and light gases. Thus, to impart highly selective properties to these membranes, further modification of the mesopores is necessary. Conventional CO_2 capture technology uses aqueous amines to absorb CO_2 , but this conventional method has several disadvantages in terms of regeneration, energy consumption, and so forth. In addition, the conventional method is only cost effective for concentrated streams of CO_2 . As an alternative benchmark technology for aqueous amine absorption, amine-functionalized mesoporous silica powder materials, such as MCM-41 [40] and SBA-15 [41] with high concentrations of amine groups inside their pores, have been shown to exhibit unusually high CO_2 sorption capacities. This selectivity is attributed to both the presence of amines on the surfaces of the powder particles and the high loading of amine groups in the mesopores following functionalization. Based on the above concept, the fabrication of amine-functionalized mesoporous silica in a membrane configuration has long been of interest for CO_2 separation. Amine-functionalized membranes should provide steady-state operation, be easy to regenerate and energy efficient, and enable the capture CO_2 from dilute streams.

There are three major techniques for the functionalization of mesopores: cocondensation, impregnation, and postsynthesis grafting, as shown in Figure 5. Impregnation involves loading a large quantity of amines dissolved in a solvent inside the pores (Figure 5(a)). However, the loaded amines tend to conglomerate, and these agglomerates are not stable after several adsorption/desorption cycles or under pressurized gas flow. During cocondensation, the amine groups are covalently bonded to the silica matrix (Figure 5(b)) and a certain percentage of the Si atoms are replaced by amino-silane groups. This method results in the uniform distribution of various functional groups without pore blocking. In

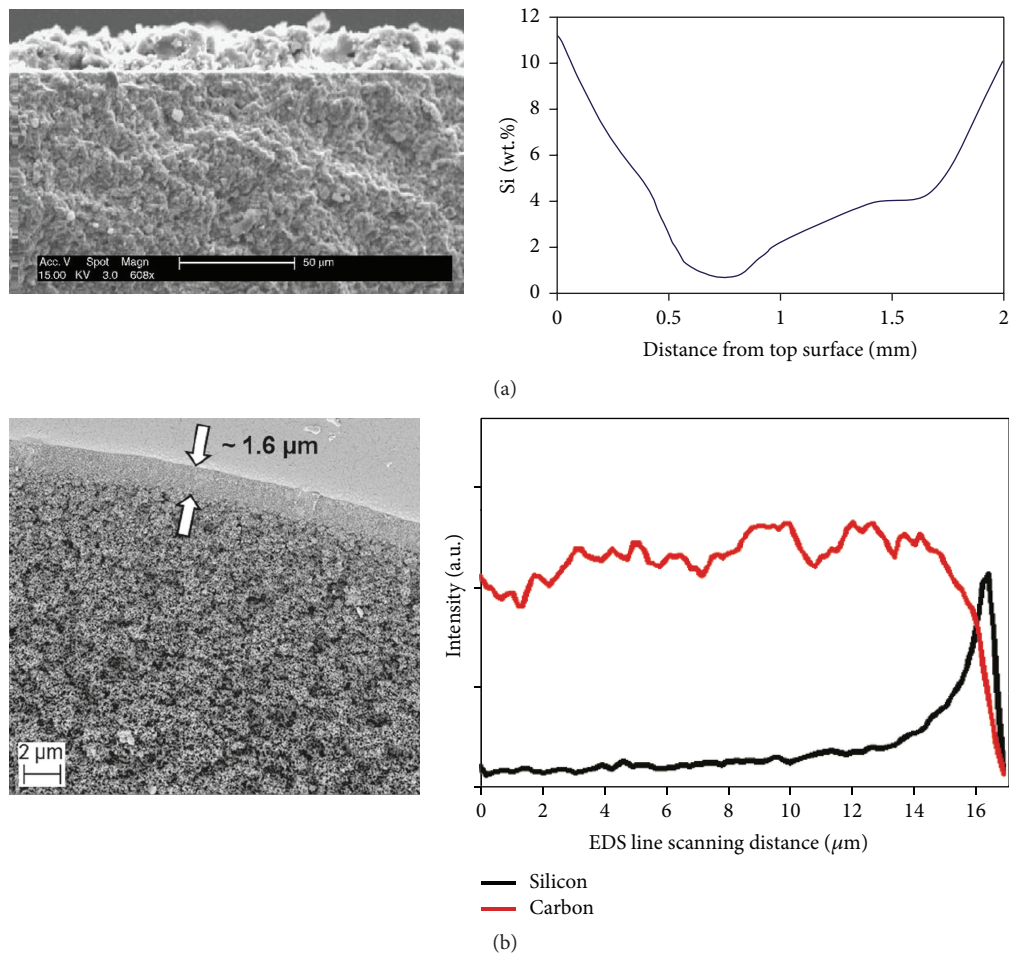


FIGURE 4: SEM images coupled with EDS line scanning analyses for (a) a flat MCM-48 membrane on an α -alumina support [52] and (b) worm-like mesoporous silica membrane on a polymeric hollow fiber support [42].

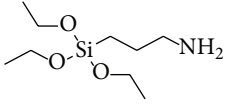
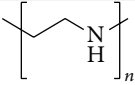
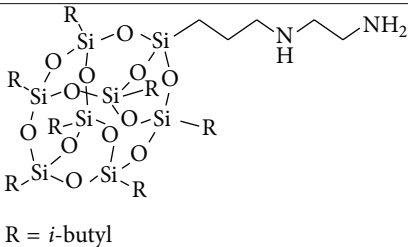
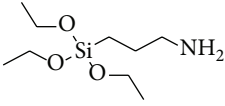
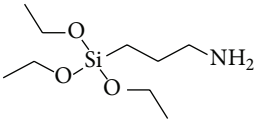
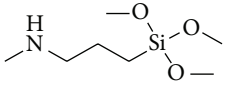
postsynthesis grafting, a reaction occurs between the silanol groups of the silica and the amines (Figure 5(c)). This approach maintains the substrate structure, and the formed amino oxides remain stable, even after several adsorption/desorption cycles.

There have been numerous studies of the amine functionalization of mesoporous silica membranes [42–48]. Table 1 lists reported examples of mesoporous silica membranes that have been functionalized with amine groups for CO_2 separation. Various supports, mesoporous silicas, functionalization agents, and methods have been used till date. Because CO_2 separation is governed by a gas diffusion mechanism, mesoporous silica containing three-dimensional interconnected pore structures, with MCM-48 as a good representative material, is most often selected by researchers to avoid the consideration of the deposition direction. The common supports used to impart mechanical strength to the mesoporous silica layer include ceramics, alumina, and more recently polymers. As mentioned above, the preferred pore activation process (thermal calcination or solvent extraction) is highly dependent on the support material. For amine modification, postsynthesis grafting provides more stable

amino-oxide hybrid membranes than other techniques. In addition, because it is important to be able to correlate pore structures, presumably the monolayer of the amine group, to transport phenomena, postsynthesis grafting is the preferred functionalization method. Amine groups are selected based on not only their affinities and reactivity with the silanol groups on the mesoporous silica but also their ability to capture CO_2 , which is typically estimated from their performance when adsorbed on silica powder.

2.3. Characterization of Functionalized Mesoporous Silica Membranes. Verification of the functionalization of mesoporous silica membranes is another challenging step. Characterization of amine-functionalized mesoporous silica powders involves the determination of their amine loading, bonding properties, and CO_2 capture capacities [49]. The ability to characterize amine-functionalized membranes is, as described above, somewhat limited, but it is possible to use similar approaches. SEM observation to confirm that the membrane remains intact and the support and silica structure have not collapsed following incorporation of the

TABLE I: Published mesoporous silica membranes functionalized with amine groups for CO₂ separation.

Support	Mesoporous silica	Functionalization agent	Functionalization method	Ref.
Alumina disk	MCM-48		Postsynthesis grafting	[47]
α -Alumina disk	MCM-48		Postsynthesis grafting	[43]
Polymeric hollow fiber	Worm-like mesoporous silica	 R = <i>i</i> -butyl	Impregnation	[42]
Vycor tube	Vycor tube		Postsynthesis grafting	[46]
Polymeric hollow fiber	Worm-like mesoporous silica		Postsynthesis grafting	[48]
γ -Alumina disk	Hybrid silica	 	Cocondensation	[44]

amine groups is generally a prerequisite prior to quantitative analysis (Figures 6(a)-6(b)).

Amine loading can be directly determined via thermogravimetric analysis, as is the case for silica powders, but obtaining the required sample quantity is often unrealistic considering the thinness of membrane layers. Thus, amine loading is typically calculated indirectly by comparing the gas permeation properties of nonfunctionalized and amine-functionalized membranes. A significant decrease in the permeability of different gases indirectly indicates the loading of amine groups in the pores.

For silica powders, it is also easy to obtain information on the bonding between silanol and amine groups using various spectroscopic techniques (Fourier transform-infrared (FT-IR), Raman, ultraviolet-visible, etc.) and the quantity of adsorbed CO₂ after CO₂ capture. However, once again the limited sample quantity for supported mesoporous silica membranes makes the use of these methods unrealistic. Thus, most efforts focus on characterization of the membrane surface. FT-IR/attenuated total reflectance (ATR) spectroscopy is one of the most reliable tools for this analysis (Figure 6(c)). X-ray diffraction (XRD) analysis has also been proved to be a useful method. In Figure 6(d), it can be seen that the

peaks in the XRD pattern of a polyethylenimine- (PEI-) modified MCM-48 membrane are blunter and lower in intensity than those for a bare MCM-48 membrane. This result indicates that the contrast between the pores and pore walls was reduced following amine functionalization and thus suggests that the mesoporous silica membrane was properly functionalized.

The CO₂ capture capacity is reflected by the selectivity of the membrane during the separation process. Gas permeation tests (single or mixed gases) are used to evaluate the membrane separation performance. As described above, a significant drop in permeability occurs following the pore modification. Moreover, the selectivity (ratio of the permeabilities of different gases) is tailored according to the choice of amine functional groups.

2.4. CO₂ Separation Using Mesoporous Silica Membranes. The permeability (P_A) of a membrane to a gas molecule A is

$$P_A \equiv \frac{N_A l}{p_2 - p_1}, \quad (1)$$

where N_A is the steady-state flux of the gas through the membrane, l is the membrane thickness, and p_2 and p_1 are

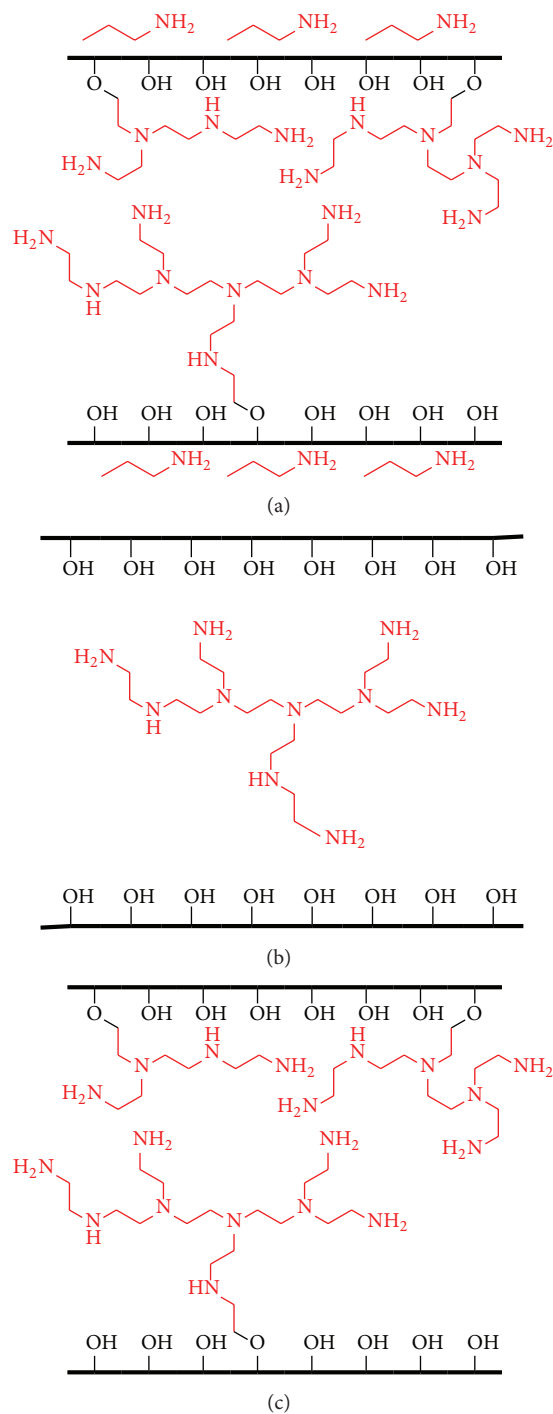


FIGURE 5: Porous silica pores loaded with polyethylenimine (PEI) using three different loading techniques: (a) cocondensation, (b) impregnation, and (c) postsynthesis grafting.

the upstream and downstream partial pressures of gas A , respectively. When the diffusion process obeys Fick's law and the downstream pressure is much less than the upstream pressure, the permeability is given by

$$P_A = D_A S_A, \quad (2)$$

where D_A is the average effective diffusivity through the membrane and S_A is the apparent sorption coefficient caused by the silica surface or the amine groups.

The ideal selectivity of a membrane for gas A over gas B is hence the ratio of their gas permeabilities:

$$\alpha_{A/B} = \frac{P_A}{P_B} = \left[\frac{D_A}{D_B} \right] \left[\frac{S_A}{S_B} \right], \quad (3)$$

where D_A/D_B is the diffusivity selectivity, that is, the ratio of the diffusion coefficients of gases A and B . The ratio of the solubilities of gases A and B , S_A/S_B , is the solubility selectivity. The diffusivity selectivity is strongly influenced by the difference in sizes of the penetrant molecules and the size-sieving ability of the membrane material, whereas the solubility selectivity is controlled by the relative adsorption/thermodynamic affinities of the penetrants for the membrane matrix [50]. An interesting aspect of amine-functionalized mesoporous silica membranes is that both types of selectivities can potentially be controlled as a result of the membrane modification.

Figure 7 shows the mechanism for CO_2 adsorption on amine-oxide surface, which is facilitated by the transport of CO_2 molecules. Unlike most other gas molecules, CO_2 reacts with amine groups via an acid-base reaction. Specifically, two moles of the amine group reacts with one mole of CO_2 to form a carbamate. The pressure of the gas flow then causes the CO_2 molecules to hop along the surface via adsorption on the next set of two amine groups. This surface diffusion contributes to the CO_2 flow and results in the CO_2 molecules passing more rapidly through the membrane than other gases, and it is the source of the selectivity for CO_2 . Notably, when water is present, the effect of surface diffusion is greater because only one mole of the surface amine is needed to react with one mole of CO_2 by forming ammonium bicarbonate, leading to an even more rapid flow of CO_2 through the membrane and thus higher selectivity. Consequently, each single reaction aids in the smooth flow of a CO_2 molecule via facilitated transport. It should also be noted that the temperature and feed pressure affect the rate of desorption of CO_2 molecules from the amine groups, and the feed ratio and CO_2 concentration in the feed affect the competitive transport of different gases.

Table 2 lists the important parameters for the CO_2 separation performance of reported amine-functionalized mesoporous silica membranes. Excellent membrane performance requires both high selectivity and high CO_2 permeance, as described by Robeson [51]. However, there is a trade-off between the two, as can be seen in Table 2. A high loading of amine groups provides very high selectivity but results in low permeance values. On the other hand, high CO_2 permeance properties with low amine loading levels result in very low selectivities. In addition, Kumar and Kim reported reverse selective properties wherein CO_2 molecules were trapped and passed more slowly through the membrane than other gases when amine groups with very high affinities for CO_2 were used [43, 48]. In these cases, due to the strong affinities of the amine groups, cross-linking occurred and resulted in sticky diffusion of the CO_2 . Amine-cross-linking occurs when ammonium carbamates are formed because two

TABLE 2: Performance of published amine-functionalized mesoporous silica membranes for CO₂ separation (GPU = 3.35 × 10⁻¹⁰ mol m⁻² s⁻¹ Pa⁻¹).

CO ₂ permeance (GPU)	Selectivity (CO ₂ /N ₂ or CH ₄)	Presence of water	Temperature	Ref.
3	800	X	373 K	[47]
0.144	0.012	O	294 K	[43]
100	17	X	308 K	[42]
0.8	10	X	393 K	[46]
1.8	0.15	X	308 K	[48]
9.4	2.5	O	308 K	[48]
63	4	X	393 K	[44]

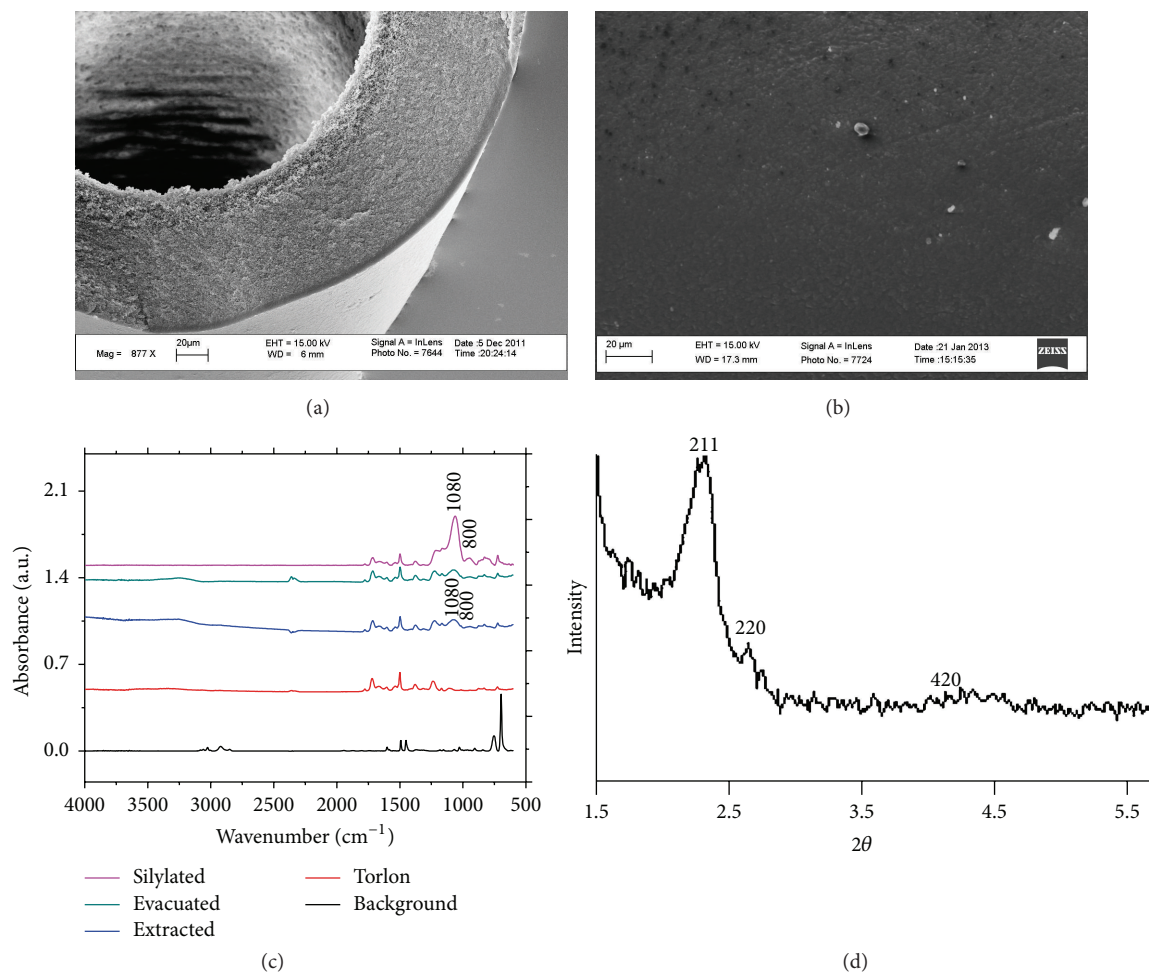


FIGURE 6: Characterization of modified mesoporous silica membranes. SEM images of the (a) cross section and (b) top view of an aziridine-functionalized mesoporous silica membrane [48], (c) FT-IR/ATR spectra for a silylated mesoporous silica membrane [53], and (d) XRD pattern of a PEI-modified MCM-48 membrane [43].

amine groups sterically exist very close. Thus, appropriate mesoporous materials, functionalization agents, and modification techniques must be employed when developing CO₂ separation membranes. On the other hand, because a wide range of amine-functionalized mesoporous silica membranes are available today, there is significant potential for fabricating highly tailored, and therefore very selective, membranes for CO₂ separation.

3. Summary

Membrane-based separation of CO₂ from mixed gas flows represents a rapidly growing research field for the porous materials community. Amine-functionalized mesoporous membranes show significantly promising CO₂ separation due to the strong adsorption properties of the surface amine groups and the regular mesopore structure used to support

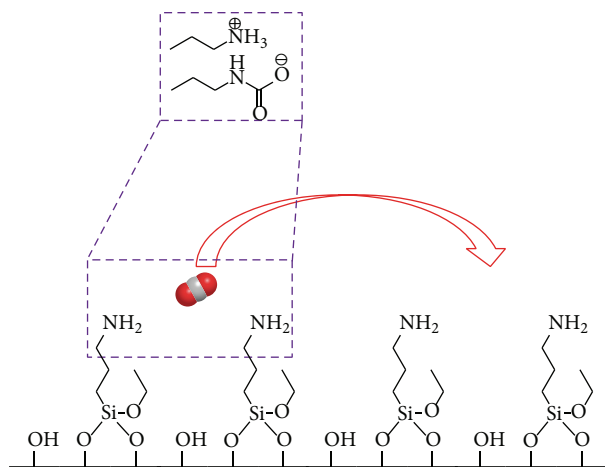


FIGURE 7: Mechanism of CO_2 adsorption on an amine-oxide surface and facilitated transport of a CO_2 molecule.

them. However, because the synthesis and characterization of amine-functionalized mesoporous silica membranes are complex, much is not yet known regarding amine loading levels, membrane pore structures, gas permeation mechanisms and their kinetics, and the correlations between these properties. Based on results obtained to date, it is thought that, along with polymers, zeolites, metal organic frameworks, and mixed-matrix membranes, amine-functionalized mesoporous silica membranes represent a technologically scalable platform. This review briefly discusses the efforts to synthesize mesoporous silica membranes, functionalize them with amines, characterize the functionalized membranes, and study their performance in CO_2 separation applications.

Conflict of Interests

The authors declare that there is no conflict of interests regarding the publication of this paper.

Acknowledgment

This work was supported by the National Research Foundation of Korea (NRF) grant funded by Korea government (MSIP) (no. NRF-2012M2A8A5025658).

References

- [1] S. Bishnoi and G. T. Rochelle, "Absorption of carbon dioxide into aqueous piperazine: reaction kinetics, mass transfer and solubility," *Chemical Engineering Science*, vol. 55, no. 22, pp. 5531–5543, 2000.
- [2] W. Chaikittisilp, S. A. Didas, H.-J. Kim, and C. W. Jones, "Vapor-phase transport as a novel route to hyperbranched polyamine-oxide hybrid materials," *Chemistry of Materials*, vol. 25, no. 4, pp. 613–622, 2013.
- [3] W. Chaikittisilp, H.-J. Kim, and C. W. Jones, "Mesoporous alumina-supported amines as potential steam-stable adsorbents for capturing CO_2 from simulated flue gas and ambient air," *Energy & Fuels*, vol. 25, no. 11, pp. 5528–5537, 2011.
- [4] W. J. Koros and G. K. Fleming, "Membrane-based gas separation," *Journal of Membrane Science*, vol. 83, no. 1, pp. 1–80, 1993.
- [5] R. Banerjee, A. Phan, B. Wang et al., "High-throughput synthesis of zeolitic imidazolate frameworks and application to CO_2 capture," *Science*, vol. 319, no. 5865, pp. 939–943, 2008.
- [6] H. Lin, E. Van Wagner, B. D. Freeman, L. G. Toy, and R. P. Gupta, "Plasticization-enhanced hydrogen purification using polymeric membranes," *Science*, vol. 311, no. 5761, pp. 639–642, 2006.
- [7] P. Bernardo, E. Drioli, and G. Golemme, "Membrane gas separation: a review/state of the art," *Industrial and Engineering Chemistry Research*, vol. 48, no. 10, pp. 4638–4663, 2009.
- [8] I. F. J. Vankelecom, "Polymeric membranes in catalytic reactors," *Chemical Reviews*, vol. 102, no. 10, pp. 3779–3810, 2002.
- [9] C. C. Striemer, T. R. Gaborski, J. L. McGrath, and P. M. Fauchet, "Charge- and size-based separation of macromolecules using ultrathin silicon membranes," *Nature*, vol. 445, no. 7129, pp. 749–753, 2007.
- [10] T. Melin, B. Jefferson, D. Bixio et al., "Membrane bioreactor technology for wastewater treatment and reuse," *Desalination*, vol. 187, no. 1–3, pp. 271–282, 2006.
- [11] Š. Schlosser, R. Kertész, and J. Marták, "Recovery and separation of organic acids by membrane-based solvent extraction and pertraction: an overview with a case study on recovery of MPCA," *Separation and Purification Technology*, vol. 41, no. 3, pp. 237–266, 2005.
- [12] R. Y. M. Huang, *Pervaporation Membrane Separation Processes*, Elsevier, Amsterdam, The Netherlands, 1991.
- [13] M. Cheryan, *Ultrafiltration and Microfiltration Handbook*, Technomic, Lancaster, Pa, USA, 1998.
- [14] W. R. Bowen, A. W. Mohammad, and N. Hilal, "Characterisation of nanofiltration membranes for predictive purposes—use of salts, uncharged solutes and atomic force microscopy," *Journal of Membrane Science*, vol. 126, no. 1, pp. 91–105, 1997.
- [15] S. Sourirajan, *Reverse Osmosis*, Academic Press, New York, NY, USA, 1970.
- [16] H. Q. Lin, E. Van Wagner, R. Raharjo, B. D. Freeman, and I. Roman, "High-performance polymer membranes for natural-gas sweetening," *Advanced Materials*, vol. 18, no. 1, pp. 39–44, 2006.
- [17] C. Hendriks, *Carbon Dioxide Removal from Coal-Fired Power Plants*, Kluwer Academic Publishers, 1994.
- [18] S. W. Choi, S. M. Jo, W. S. Lee, and Y.-R. Kim, "An electrospun poly (vinylidene fluoride) nanofibrous membrane and its battery applications," *Advanced Materials*, vol. 15, no. 23, pp. 2027–2032, 2003.
- [19] Y. Lu, R. Ganguli, C. A. Drewien et al., "Continuous formation of supported cubic and hexagonal mesoporous films by sol-gel dip-coating," *Nature*, vol. 389, no. 6649, pp. 364–368, 1997.
- [20] G. S. Attard, J. C. Glyde, and C. G. Göltner, "Liquid-crystalline phases as templates for the synthesis of mesoporous silica," *Nature*, vol. 378, no. 6555, pp. 366–368, 1995.
- [21] C. T. Kresge, M. E. Leonowicz, W. J. Roth, J. C. Vartuli, and J. S. Beck, "Ordered mesoporous molecular sieves synthesized by a liquid-crystal template mechanism," *Nature*, vol. 359, no. 6397, pp. 710–712, 1992.
- [22] T.-W. Kim, R. Ryoo, M. Kruk et al., "Tailoring the pore structure of SBA-16 silica molecular sieve through the use of copolymer blends and control of synthesis temperature and time," *Journal of Physical Chemistry B*, vol. 108, no. 31, pp. 11480–11489, 2004.

- [23] N. Hiyoshi, K. Yogo, and T. Yashima, "Adsorption of carbon dioxide on amine-modified MSU-H silica in the presence of water vapor," *Chemistry Letters*, vol. 37, no. 12, pp. 1266–1267, 2008.
- [24] T. Yu, H. Zhang, X. Yan et al., "Pore structures of ordered large cage-type mesoporous silica FDU-12s," *Journal of Physical Chemistry B*, vol. 110, no. 43, pp. 21467–21472, 2006.
- [25] S. Ruthstein, J. Schmidt, E. Kesselman et al., "Molecular level processes and nanostructure evolution during the formation of the cubic mesoporous material KIT-6," *Chemistry of Materials*, vol. 20, no. 8, pp. 2779–2792, 2008.
- [26] T. Yokoi, H. Yoshitake, and T. Tatsumi, "Synthesis of anionic-surfactant-templated mesoporous silica using organoalkoxysilane-containing amino groups," *Chemistry of Materials*, vol. 15, no. 24, pp. 4536–4538, 2003.
- [27] T.-L. Chew, A. L. Ahmad, and S. Bhatia, "Ordered mesoporous silica (OMS) as an adsorbent and membrane for separation of carbon dioxide (CO₂)," *Advances in Colloid and Interface Science*, vol. 153, no. 1-2, pp. 43–57, 2010.
- [28] A. MacArio, A. Katovic, G. Giordano, F. Iucolano, and D. Caputo, "Synthesis of mesoporous materials for carbon dioxide sequestration," *Microporous and Mesoporous Materials*, vol. 81, no. 1–3, pp. 139–147, 2005.
- [29] X. Wang, V. Schwartz, J. C. Clark et al., "Infrared study of CO₂ sorption over "molecular basket" sorbent consisting of polyethylenimine-modified mesoporous molecular sieve," *Journal of Physical Chemistry C*, vol. 113, no. 17, pp. 7260–7268, 2009.
- [30] X. Xu, C. Song, J. M. Andresen, B. G. Miller, and A. W. Scaroni, "Novel polyethylenimine-modified mesoporous molecular sieve of MCM-41 type as high-capacity adsorbent for CO₂ capture," *Energy & Fuels*, vol. 16, no. 6, pp. 1463–1469, 2002.
- [31] S. Kim, J. Ida, V. V. Guliants, and J. Y. S. Lin, "Tailoring pore properties of MCM-48 silica for selective adsorption of CO₂," *The Journal of Physical Chemistry B*, vol. 109, no. 13, pp. 6287–6293, 2005.
- [32] C. W. Jones, K. Tsuji, and M. E. Davis, "Organic-functionalized molecular sieves (OFMSs):: II. Synthesis, characterization and the transformation of OFMSs containing non-polar functional groups into solid acids," *Microporous and Mesoporous Materials*, vol. 33, no. 1–3, pp. 223–240, 1999.
- [33] M. E. Davis, "Ordered porous materials for emerging applications," *Nature*, vol. 417, no. 6891, pp. 813–821, 2002.
- [34] D.-H. Park, N. Nishiyama, Y. Egashira, and K. Ueyama, "Enhancement of hydrothermal stability and hydrophobicity of a silica MCM-48 membrane by silylation," *Industrial & Engineering Chemistry Research*, vol. 40, no. 26, pp. 6105–6110, 2001.
- [35] B. A. McCool, N. Hill, J. DiCarlo, and W. J. DeSisto, "Synthesis and characterization of mesoporous silica membranes via dip-coating and hydrothermal deposition techniques," *Journal of Membrane Science*, vol. 218, no. 1-2, pp. 55–67, 2003.
- [36] L. G. A. van de Watera and T. Maschmeyer, "Mesoporous membranes—a brief overview of recent developments," *Topics in Catalysis*, vol. 29, no. 1-2, pp. 67–77, 2004.
- [37] K. D. Hammond, G. A. Tompsett, S. M. Auerbach, and W. C. Conner, "Apparatus for measuring physical adsorption on intact supported porous membranes," *Journal of Porous Materials*, vol. 14, no. 4, pp. 409–416, 2007.
- [38] K. D. Hammond, M. Hong, G. A. Tompsett, S. M. Auerbach, J. L. Falconer, and W. C. Conner Jr., "High-resolution physical adsorption on supported borosilicate MFI zeolite membranes: comparison with powdered samples," *Journal of Membrane Science*, vol. 325, no. 1, pp. 413–419, 2008.
- [39] H.-J. Kim, K.-S. Jang, P. Galebach et al., "Seeded growth, silylation, and organic/water separation properties of MCM-48 membranes," *Journal of Membrane Science*, vol. 427, pp. 293–302, 2013.
- [40] Y. Belmabkhout and A. Sayari, "Effect of pore expansion and amine functionalization of mesoporous silica on CO₂ adsorption over a wide range of conditions," *Adsorption*, vol. 15, no. 3, pp. 318–328, 2009.
- [41] J. C. Hicks, J. H. Drese, D. J. Fauth, M. L. Gray, G. Qi, and C. W. Jones, "Designing adsorbents for CO₂ capture from flue gas-hyperbranched aminosilicas capable of capturing CO₂ reversibly," *Journal of the American Chemical Society*, vol. 130, no. 10, pp. 2902–2903, 2008.
- [42] K.-S. Jang, H.-J. Kim, J. R. Johnson et al., "Modified mesoporous silica gas separation membranes on polymeric hollow fibers," *Chemistry of Materials*, vol. 23, no. 12, pp. 3025–3028, 2011.
- [43] P. Kumar, S. Kim, J. Ida, and V. V. Guliants, "Polyethylenimine-modified MCM-48 membranes: effect of water vapor and feed concentration on N₂/CO₂ selectivity," *Industrial & Engineering Chemistry Research*, vol. 47, no. 1, pp. 201–208, 2008.
- [44] S. B. Messaoud, A. Takagaki, T. Sugawara, R. Kikuchi, and S. T. Oyama, "Alkylamine-silica hybrid membranes for carbon dioxide/methane separation," *Journal of Membrane Science*, vol. 477, pp. 161–171, 2015.
- [45] Y.-F. Lin, C.-H. Chen, K.-L. Tung, T.-Y. Wei, S.-Y. Lu, and K.-S. Chang, "Mesoporous fluorocarbon-modified silica aerogel membranes enabling long-term continuous CO₂ capture with large absorption flux enhancements," *ChemSusChem*, vol. 6, no. 3, pp. 437–442, 2013.
- [46] M. Ostwal, R. P. Singh, S. F. Dec, M. T. Lusk, and J. D. Way, "3-Aminopropyltriethoxysilane functionalized inorganic membranes for high temperature CO₂/N₂ separation," *Journal of Membrane Science*, vol. 369, no. 1-2, pp. 139–147, 2011.
- [47] Y. Sakamoto, K. Nagata, K. Yogo, and K. Yamada, "Preparation and CO₂ separation properties of amine-modified mesoporous silica membranes," *Microporous and Mesoporous Materials*, vol. 101, no. 1-2, pp. 303–311, 2007.
- [48] H. J. Kim, W. S. Chaikittisilp, K. S. Jang et al., "Aziridine-functionalized mesoporous silica membranes on polymeric hollow fibers: Synthesis and single-component CO₂ and N₂ permeation properties," *Industrial & Engineering Chemistry Research*, vol. 54, no. 16, pp. 4407–4413, 2015.
- [49] P. Bollini, S. A. Didas, and C. W. Jones, "Amine-oxide hybrid materials for acid gas separations," *Journal of Materials Chemistry*, vol. 21, no. 39, pp. 15100–15120, 2011.
- [50] H. Lin and B. D. Freeman, "Gas solubility, diffusivity and permeability in poly(ethylene oxide)," *Journal of Membrane Science*, vol. 239, no. 1, pp. 105–117, 2004.
- [51] L. M. Robeson, "The upper bound revisited," *Journal of Membrane Science*, vol. 320, no. 1-2, pp. 390–400, 2008.
- [52] P. Kumar, J. Ida, S. Kim, V. V. Guliants, and J. Y. S. Lin, "Ordered mesoporous membranes: effects of support and surfactant removal conditions on membrane quality," *Journal of Membrane Science*, vol. 279, no. 1-2, pp. 539–547, 2006.
- [53] H.-J. Kim, N. A. Brunelli, A. J. Brown et al., "Silylated mesoporous silica membranes on polymeric hollow fiber supports: synthesis and permeation properties," *ACS Applied Materials & Interfaces*, vol. 6, no. 20, pp. 17877–17886, 2014.

Research Article

Evaluation of Optimal Pore Size of (3-Aminopropyl)triethoxysilane Grafted MCM-41 for Improved CO₂ Adsorption

Zhilin Liu, Yang Teng, and Kai Zhang

Beijing Key Laboratory of Emission Surveillance and Control for Thermal Power Generation,
North China Electric Power University, Beijing 102206, China

Correspondence should be addressed to Kai Zhang; kzhang@ncepu.edu.cn

Received 3 June 2015; Revised 27 July 2015; Accepted 30 July 2015

Academic Editor: Khaldoun Bachari

Copyright © 2015 Zhilin Liu et al. This is an open access article distributed under the Creative Commons Attribution License, which permits unrestricted use, distribution, and reproduction in any medium, provided the original work is properly cited.

An array of new MCM-41 with substantially larger average pore diameters was synthesized through adding 1,3,5-trimethylbenzene (TMB) as the swelling agent to explore the effect of pore size on final adsorbent properties. The pore expanded MCM-41 was also grafted with (3-Aminopropyl)triethoxysilane (APTES) to determine the optimal pore size for CO₂ adsorption. The pore-expanded mesoporous MCM-41s showed relatively less structural regularity but significant increments of pore diameter (4.64 to 7.50 nm); the fraction of mesopore volume also illustrated an increase. The adsorption heat values were correlated with the order of the adsorption capacities for pore expanded MCM-41s. After amine functionalization, the adsorption capacities and heat values showed a significant increase. APTES-grafted pore-expanded MCM-41s depicted a high potential for CO₂ capture regardless of the major drawback of the high energy required for regeneration.

1. Introduction

Fossil fuels will remain in abundant provision well into the 21st century and contribute to the high standard of living enjoyed by the industrialized world. However, the environmental and economic threats caused by possible climate change which is commonly referred to as the greenhouse effect make their future uncertain [1]. In order to reduce global warming and enjoy the benefits of fossil fuels, CO₂ adsorption and separation in a cost-effective and environmentally friendly way is one of the most promising means [2, 3].

Several groups [4–9] proposed to immobilize amines onto the mesoporous materials to capture CO₂. Mesoporous silica such as MCM [9], SBA [10, 11], MSU [12], silica foam [13], and KIT-6 [14] types have attracted great attention of a large community of researchers for gas separation applications. They found that the CO₂ adsorption rate and capacity are chiefly determined on not only amine content but also the support porosity. Moreover, the two factors are not thoroughly independent since supports with higher pore

sizes could load more amines. Among many well-known mesoporous materials, MCM-41 offers many advantages in terms of rapid adsorption kinetics, easy-to-design pore structure, large surface area, and low energy required for regeneration [15–17]. Additionally, MCM-41 possesses a large amount of Si-OH on its surface which provides abundant reaction sites and Si in the framework of silica could be replaced by other atoms, which makes the modification easier [18].

Various methods have been developed for the synthesis of MCM-41 silica with larger pore sizes [19–22]. Conventional MCM-41 silica exhibits a typical pore size within the range of 3 to 4 nm. Corma et al. [23] obtained MCM-41 with the pore size of 6 nm to 7 nm after rising the synthesis temperature (408–448 K). Zhao et al. [24] also concluded that the temperature could affect the pore size. Wang and Kabe [25] modified the pH to increase the pore size from 3.83 nm to 5.27 nm. Expanders (e.g., alkanes [26], amines [22], and trimethylbenzene [27]) also have been used for the pore expansion of mesoporous materials. Wang and Yang [10] expanded the pore diameter of SBA-15 through adding TMB

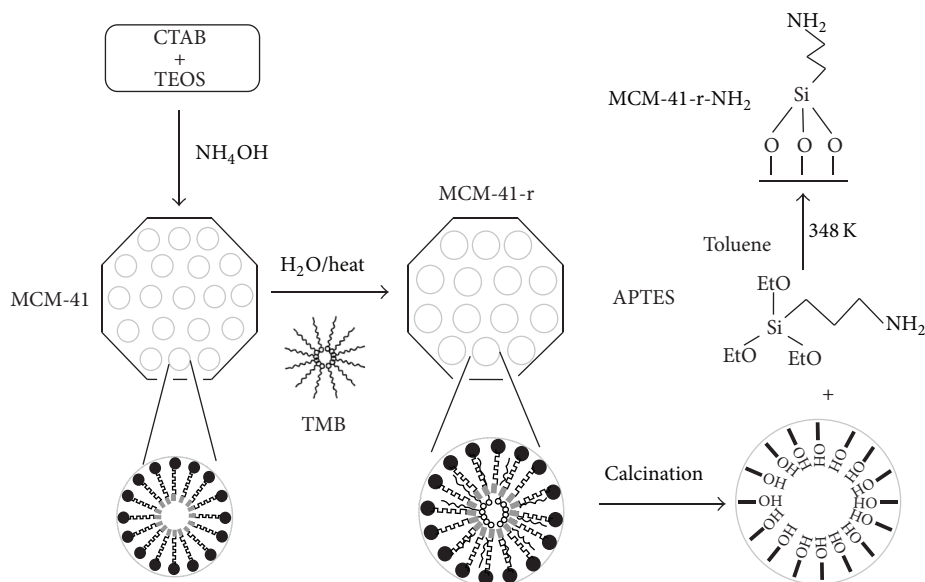


FIGURE 1: Synthesis route of APTES grafted pore-expanded MCM-41.

as swelling agent to 7.6 nm and after amine grafted, the pore diameter reduced to 5.3 nm. The CO₂ adsorption capacity of APTES grafted SBA-15 reached 1.6 mmol/g. Loganathan et al. [19, 28] prepared pore expanded MCM-41 by varying the amount of ammonia (the required preparation materials). As the amount of ammonia decreased, the pore size and volume of MCM-41 increased. The CO₂ capacity of pore expanded MCM-41 was as much as 1.2 mmol/g. However, valuable information obtained shows that pore expansion easily led to a decrease of the mesostructure order. When the pore size is larger than 5 nm, the nanostructures become unstable and the pore walls cannot support three-dimensional skeleton; it is likely to cause the structural collapse. The difficulty to modify the pores increases with the presence of swelling agent. Additionally, most papers only found that pore enlargement could enhance the CO₂ adsorption performance [4, 22, 29, 30], but few work study the relationship between the pore size and CO₂ adsorption behavior.

Therefore, evaluating the optimal pore size is of great importance to synthesis amine-functionalization adsorbents for improved CO₂ adsorption. According to this, in this paper, a series of pore-expanded MCM-41s with increasing pore size were used as supports and APTES which contains three amine groups per organic chain was preferred as the grafted species to obtain superior capacity. Well-uniformed pore-expanded MCM-41s were examined; the effect of pore size on CO₂ adsorption capacity, surface grafted, and adsorption heat was also investigated.

2. Materials and Method

2.1. Materials. The reagents of Tetraethylorthosilicate (TEOS) used for the synthesis of pore-expanded MCM41 was purchased from Tianjin Fu Chen Chemical Reagents Factory; the chemical formula is C₈H₂₀O₄Si and the molar

mass is 208.33 g/mol, AR. Hexadecyltrimethyl ammonium bromide (CTAB) with the molar mass of 364.446 g/mol was used as the template agent and the chemical formula is C₁₉H₄₂BrN. 1,3,5-trimethylbenzene (TMB) was chosen as the swelling agent and produced by Tianjin Guangfu Fine Chemical Research Institute, AR. Ethanol (95% ACS grade), toluene (99% ACS grade), and ammonia (25% ACS grade) were bought from Beijing Chemical Works. (3-Aminopropyl)triethoxysilane (APTES) obtained from J&K Scientific Ltd. was used as the amino silane coupling agent.

Figure 1 illustrates the procedure for the synthesis of pore-expanded MCM-41 and a schematic diagram of the amine grafting. The periodic mesoporous MCM-41 was prepared in the presence of CTAB and TEOS according to the procedure reported by Cai et al. [17] and was further expanded through adding swelling agent. MCM-41-r0, MCM-41-r2, MCM-41-r4, MCM-41-r6, and MCM-41-r8 were successfully synthesized and r means the molar ratio between swelling agent and template agent.

The five pore-expanded MCM-41s were used as supports and APTES was chosen as the amine base to synthesize the amine grafted MCM-41s. Toluene was added to the flask as the reaction solvent, and then excess APTES was added; thereafter, measured MCM-41 was put into the flask; the mixed solution was placed in a magnetic stirrer at 348 K for 20 hours. After cooling the solution to room temperature, the product was recovered by filtration on a Buchner funnel, washed with water, and dried in air at ambient temperature to acquire the amine-grafted materials. The materials were named as MCM-41-r-NH₂ s.

2.2. Characterization and CO₂ Adsorption Measurements. The crystal structures of all adsorbents were characterized by X-ray diffraction (XRD) on D8 ADVANCE (Bruker,

German) diffractometer operating at 40 kV and 30 mA with CuK α radiation (0.1541 nm). The XRD diffraction patterns were taken in the 2θ range of 1.3° – 10° at a scan speed of $0.5^\circ \cdot \text{min}^{-1}$.

Pore diameter, volume, and surface area of the samples synthesized were evaluated via N₂ physical adsorption analysis through ASAP2020 (Micromeritics, USA) automatic adsorption system. The N₂ adsorption data was recorded at the liquid N₂ temperature (77 K). The surface area and the pore size distribution were calculated by the BET and BJH equations. The total pore volume was estimated from the amount of adsorbed N₂ at the partial pressure $P/P_0 = 0.99$.

Thermal gravimetric analysis (TA Instruments, USA) was applied to determine the amount of amine loading and the thermal stability of adsorbent. From a series of experiments, it was determined to treat the materials at 373 K for a period of 60 min in N₂ to remove all the water and CO₂ adsorbed from the air. After the initial heat treatment, a heating rate of $10 \text{ K} \cdot \text{min}^{-1}$ up to 973 K in N₂ was conducted to calculate the real amine impregnated on substracts.

CO₂ adsorption measurements were also performed on thermal gravimetric analysis under atmosphere pressure. A mixture gas of 10% CO₂ and 90% N₂ was used as the model flue gas. In each run, the adsorbents were loaded into an alumina sample pan and afterward pretreated at 283 K for 1 hour in N₂ to remove the adsorbed moisture, and then the adsorbents were cooled to the adsorption temperature of 308 K prior to their exposure to the mixture gas. The desorption run was conducted in a pure N₂ flow at 373 K to achieve complete desorption.

3. Results and Discussion

3.1. Material Characterization. The Nitrogen adsorption isotherms observed from Figure 2 of MCM-41-r0 and MCM-41-r2 exhibit a typical type IV adsorption-desorption isotherm according to the IUPAC classification, which demonstrates the characteristic of mesoporous materials. The capillary condensation in mesopores of MCM-41-r2 in mesopores occurred at a higher relative pressure due to their larger pore diameter compared with conventional MCM-41. The pore diameter of MCM-41-r2 increased significantly to 5.12 nm. The pore volume of MCM-41-r2 was around 1.00 cm^3 , similar to the value of MCM-41-r0. The pore-expanded MCM-41-r2 showed comparably lower pore volume of $771 \text{ m}^2/\text{g}$ but the value is not far from that of conventional MCM-41 ($865 \text{ m}^2/\text{g}$). The pore size of MCM-41-r2 increased significantly but the mesostructure order decreased as a result of pore expansion. In order to continuously enlarge the pore size of MCM-41, more swelling agent was required to add into the mixture; however, excessive swelling agent may destroy the mesostructure.

Due to a slight loss of the mesostructure during the pore-expansion process, the intensity of diffraction peaks of MCM-41-r2 was lower than that of MCM-41-r0 [31] as demonstrated in Figure 3 which showed the XRD patterns of MCM-41-r0 and MCM-41-r2. The highest peaks observed shifted to lower

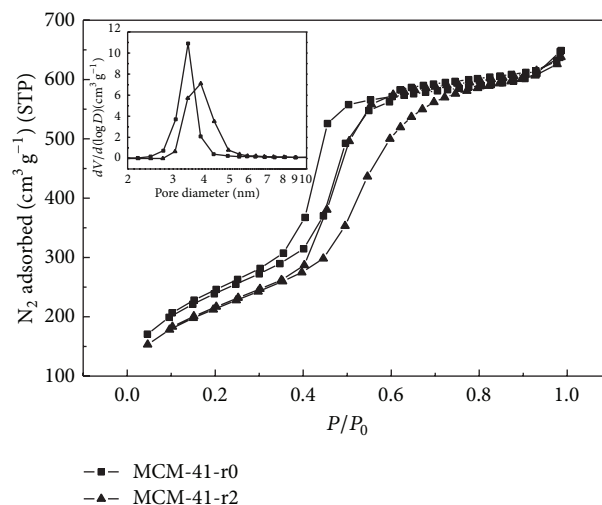


FIGURE 2: The Nitrogen adsorption isotherms of MCM-41-r0 and MCM-41-r2 and the distribution of pore size.

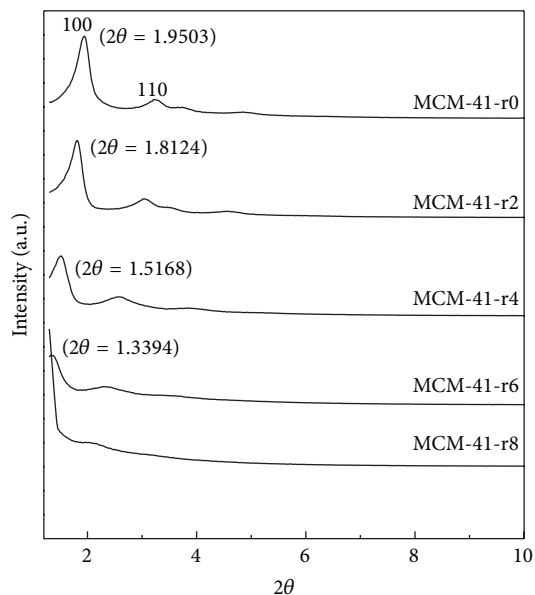


FIGURE 3: The XRD patterns of pore-expanded MCM-41s.

2θ from 1.9503° to 1.8124° , and the smaller 2θ related to the large cell parameters.

As shown in Figure 3, all the pore-expanded MCM-41s were studied to explore the effect of swelling agent on structure characteristics. In the process of pore-expanding, when increasing the amount of TMB, TMB molecules congregate to form “big oil particle” and TMB added to the reaction gel can be solubilized inside the hydrophobic regions of micelles. The hydrophobic solvate interaction of the aromatic molecule with the hydrocarbon tails is analogous to the hydrophilic solvate interaction of water with the charged head groups of CTAB. This caused an increase in the micelle diameter and an enlargement of the pore size. The TMB between the surfactant molecules of the micelles can interact with

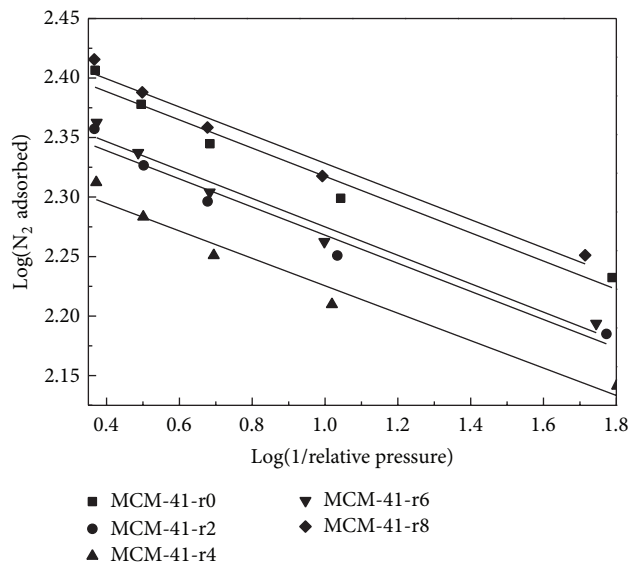


FIGURE 4: D-R plots of N_2 adsorption isotherm on the pore expanded MCM-41.

the ammonium cations of the surfactants through its π -electrons. It caused an additional increase in the micelles and consequently an enlargement of the pore size [32]. It is clear that the peaks between 1° and 2° can still be observed when the ratios of TMB/CTAB are less than 8; however, the intensity of the peaks decreased greatly. The pattern had a clear (100) peak at 1.9503° ; the sample prepared using a TMB/CTAB ratio of 2 exhibited a $d(100)$ spacing of 5.12 nm compared with 4.64 nm in the absence of TMB. No peak was detected for samples synthesized with the TMB/CTAB ratio of 8, indicating that a disordered pore structure was obtained. From inspection of these XRD patterns, a conclusion is drawn that the structural ordering of the obtained materials decreases as the ratio of TMB/CTAB increases.

Figure 4 depicts the micropore volume of the pore expanded MCM-41 calculated using the Dubinin-Radushkevich (D-R) equation [33]:

$$\log W = \log W_0 - D \left(\log \left(\frac{P}{P_0} \right) \right)^2. \quad (1)$$

Here, $D = B(T/\beta)^2$, B is the adsorbent constant, β is the affinity coefficient, W is the amount of the liquid adsorbate at relative pressure of P/P_0 , and W_0 is the micropore volume. The results are shown in Table 1, with the increase of the molar ratio between swelling agent and template agent; both mesopore volume and percentages of mesopore volume were increasing which proved that the pore expanded mesoporous MCM-41s were synthesized successfully.

Table 1 also summarizes the textural properties calculated from N_2 adsorption isotherms. As the swelling agent increased, the pore sizes rose slightly from 4.64 nm to 7.50 nm. In the process of crystallization reaction, the TMB molecules entered the surfactant micelles, and, consequently, the pore sizes were expanded. The increase of TMB resulted in the concomitant increase of pore size, but when the

TABLE 1: Pore structure parameters of the MCM-41s used different amount of swelling agent.

Sample	S_{BET}^a m ² /g	V_{total}^b cm ³ /g	V_{Micro}^c cm ³ /g	V_{Meso}^d cm ³ /g	F_{meso}^e %	d^f nm
MCM-41-r0	865	1.00	0.27	0.73	0.73	4.64
MCM-41-r2	771	0.98	0.24	0.74	0.76	5.12
MCM-41-r4	696	0.97	0.22	0.75	0.77	5.61
MCM-41-r6	784	1.28	0.24	1.04	0.81	6.57
MCM-41-r8	780	1.61	0.28	1.33	0.83	7.50

^a S_{BET} : surface area calculated using BET equation.

^b V_{total} : total pore volume estimated at relative pressure.

^c V_{Micro} : micropore volume is determined from the Dubinin-Radushkevich equation.

^d V_{Meso} : subtraction of micropore volume from total volume.

^e F_{meso} : fraction of mesopore volume.

^f d : the average pore diameter.

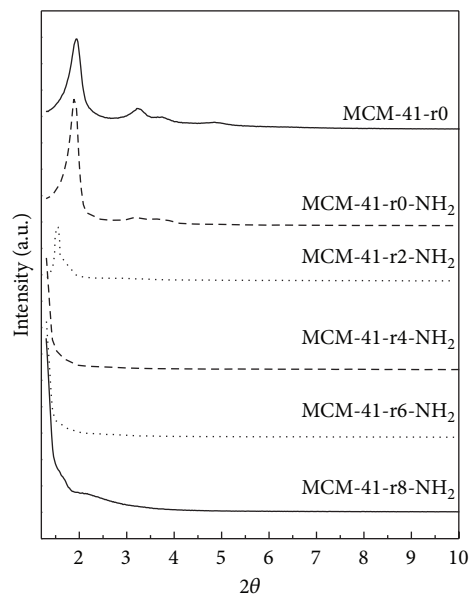


FIGURE 5: The XRD patterns of amine-grafting pore-expanded MCM-41s.

amount increased consecutively, the dissolution degrees were inconsistent in the micelle due to the effect of hydrophobic; the structural order of the hexagonal mesophase would be destroyed [30] and foam-like structures would be obtained [34]. The destroyed mesostructure made the change of surface area and pore volume irregular. As a result, the surface area and pore volume showed no significant change. Although calcined MCM-41-r8 showed structural disordering, it exhibited relatively narrow pore size distribution. Therefore, it was suitable to immobilize more APTES inside the pores.

In a further step, MCM-41-r0, MCM-41-r2, MCM-41-r4, MCM-41-r6, and MCM-41-r8 were grafted with APTES to study the effect of amine base on structure. As shown in Figure 5, it depicts the XRD patterns of amine-grafting

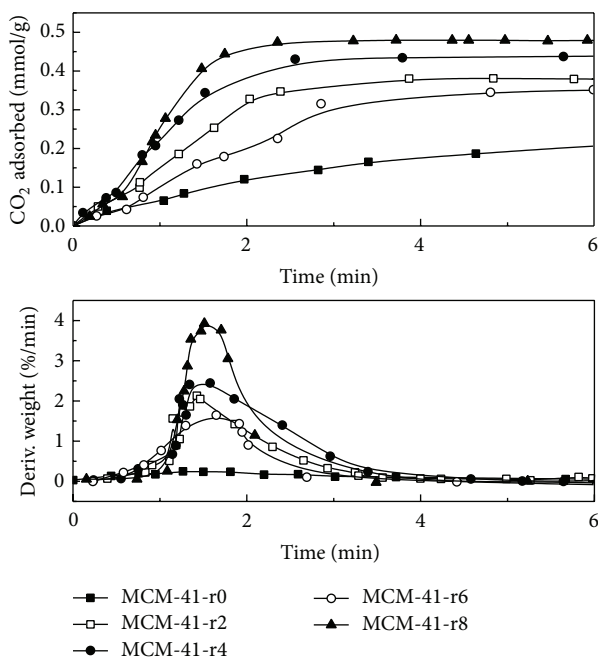


FIGURE 6: Adsorption curves and adsorption rate curves of pore-expanded MCM-41s.

pore-expanded MCM-41s compared with the original pore-expanded MCM-41; the degree of order of APTES-grafted pore-expanded MCM-41s reduced significantly as a result of grafting. It related to the presence of organosilane molecules within the pores of pore-expanded MCM-41 [31]. For MCM-41-r4-NH₂, MCM-41-r6-NH₂, and MCM-41-r8-NH₂, the mesostructure was not maintained. However, the influence of amine fictionalization and pore size could be concluded by the trend.

3.2. Adsorption

3.2.1. Influence of Pore Size on Adsorption. Figure 6 shows the CO₂ adsorption capacity and the adsorption rate on MCM-41-r0 at 308 K under the mixture gas of 10% CO₂/90% N₂ at a flow rate of 50 mL/min. Pure Nitrogen flowed through the surface of silica in the first 336 s, giving the background absorbance. Then, 10% of CO₂ in Nitrogen was substituted in the flow and adsorbed on the silica surface. The corresponding absorbance increased rapidly to reach a steady state. The maximum capacity of MCM-41-r0 calculated from the figure was 0.27 mmol/g and the largest adsorption rate was 0.30%/min.

Table 2 demonstrates the adsorption capacities and rates of the MCM-41-r samples. As seen from the table, the CO₂ adsorption capacity and adsorption rate have been significantly improved with the larger pore size when $r < 4$. In this region, MCM-41-r4 showed the largest adsorption capacity and adsorption rate of 0.44 mmol/g and 2.45%/min, respectively, even when the surface area was the smallest, and they were 1.7 and 7.8 times more than the values of MCM-41-r0. The reasons for this apparent discrepancy were that the

TABLE 2: The adsorption capacities and rates of pore-expanded MCM-41s.

Samples	Capacity (mmol/g)	Max adsorption rate (%/min)	Adsorption heat (kJ/mol)
MCM-41-r0	0.24	0.25	-15.10
MCM-41-r2	0.38	2.13	-21.21
MCM-41-r4	0.44	2.45	-24.65
MCM-41-r6	0.35	1.65	-20.02
MCM-41-r8	0.48	3.93	-26.33

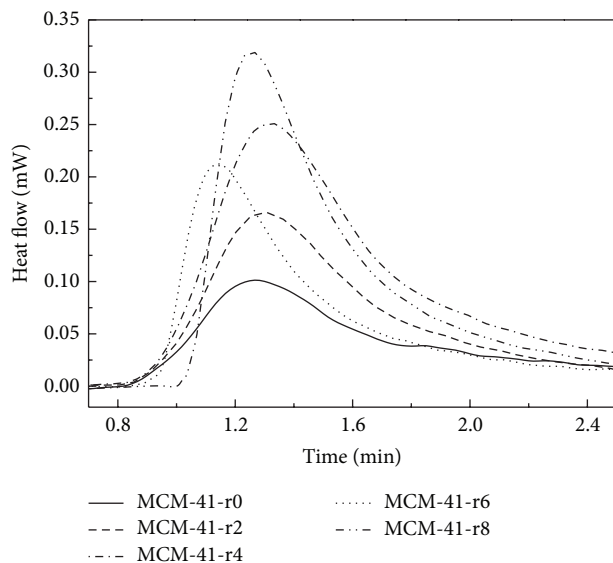


FIGURE 7: Adsorption heat of pore-expanded MCM-41s.

degree of order and crystallinity still remained high when $r < 4$ although they showed the larger pore sizes. Physical adsorption was enhanced with increasing pore size [31]. However, for MCM-41-r6, the physical adsorption capacity and rate reduced because of the destroyed mesostructure. For MCM-41-r8, the CO₂ adsorption capacity and adsorption rate illustrated apparent increases to 0.48 mmol/g and 3.93%/min separately. MCM-41-r8 showed the highest CO₂ adsorption capacity and rate, but the mesostructure was totally destroyed; the pore size and characteristics were not uniform; the adsorption mechanism was difficult to distinguish and required further research.

The adsorption heat values of pore-expanded MCM-41 samples are illustrated in Figure 7 and the results are summarized in Table 2. The corresponding values obtained from the thermodynamic analysis increased in the order of MCM-41-r0, MCM-41-r6, MCM-41-r2, MCM-41-r4, and MCM-41-r8 which are correlating with the order of the adsorption capacity; this was also consistent with a higher interaction potential between the adsorbate and adsorbent molecules with larger pore size. MCM-41-r8 showed the highest value of -26.33 kJ/mol. All the values were in the range of -27 to -15 kJ/mol, and it demonstrated that the processes belong to physical adsorption. Weak van der Waals force

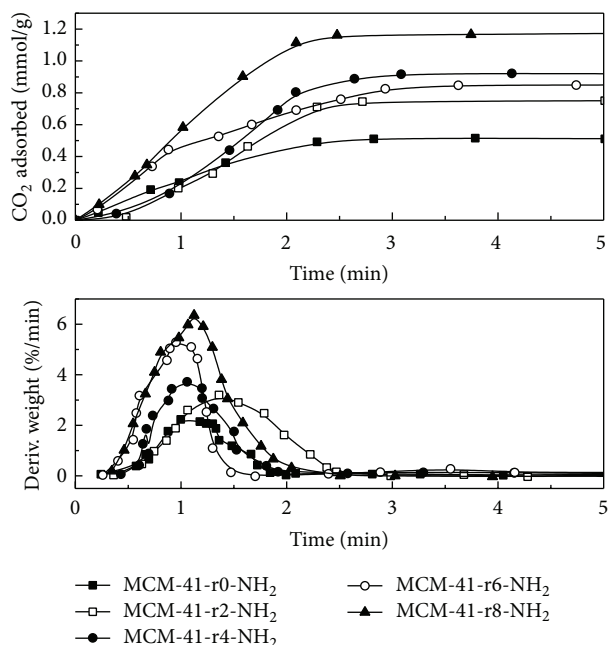


FIGURE 8: Adsorption curves and adsorption rate curve of pore-expanded MCM-41-NH₂.

TABLE 3: Summary of MCM-41-r-NH₂s adsorption data.

Materials	Adsorption capacity (mmol/g)	Max adsorption rate (%/min)	Adsorption heat (kJ/mol)
MCM-41-r0-NH ₂	0.51	1.15	-45.54
MCM-41-r2-NH ₂	0.74	3.36	-55.46
MCM-41-r4-NH ₂	0.92	3.68	-65.70
MCM-41-r6-NH ₂	0.85	3.56	-60.80
MCM-41-r8-NH ₂	1.16	4.28	-85.79

contributed to the adsorption capacity. The negative values of adsorption heat illustrated that the reaction was exothermic between the adsorbent and adsorbate interface.

3.2.2. Influence of Amine Functionalized to Adsorption. MCM-41-r-NH₂s were used to study the adsorption performance and calculate the adsorption heat; the adsorbents were kept under the condition of 393 K in the pure Nitrogen for 2 h; after that, switch the gas to 10% CO₂/90% N₂ for 5 hours to make sure there was no change of the weight.

Figure 8 represents the adsorption and adsorption rate of APTES grafted pore-expanded MCM-41. The maximum capacity calculated from the figure was 1.16 mmol/g and the adsorption heat was -85.79 kJ/mol. The adsorption capacity, adsorption rate, and adsorption heat of other APTES-grafted MCM-41-r samples are exhibited in Table 3. The adsorption capacities of APTES grafted MCM-41 increased significantly due to the amine groups which could react with CO₂ molecules. Compared with the original CO₂ adsorption capacity of 0.67 mmol/kg, the sample could absorb more

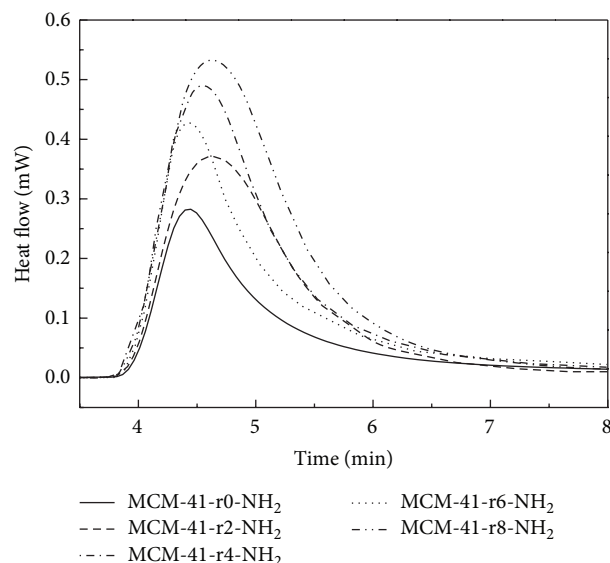


FIGURE 9: Adsorption heat of APTES grafted pore-expanded MCM-41.

CO₂. The adsorption heat values were more than 40 kJ/mol, which indicates the chemical adsorption.

For all amine-grafted materials, APTES grafted pore-expanded MCM-41s exhibited much higher adsorption capacities and adsorption rates than the APTES grafted conventional MCM-41. These data also implied that the pore-expanded MCM-41 material can be grafted with a slightly higher quantity of APTES than the conventional MCM-41. This behavior was largely due to high surface density and the possible aminosilane polymerization at the pore openings. Furthermore, the dynamic adsorption performance of APTES grafted pore-expanded MCM-41s was far superior to APTES grafted MCM-41. The plateau of max adsorption rate (MCM-41-r2-NH₂, MCM-41-r4-NH₂, and MCM-41-r6-NH₂) may be related to the mobility of the CO₂ within the pore, caused by the openness of the pore.

Figure 9 and Table 3 depict the adsorption heat of APTES grafted pore-expanded MCM-41; the trend is similar to the adsorption heat of pore expanded MCM-41. From these data, it was apparent that the pore-expanded MCM-41s were capable of grafting more amine but with negative effects of more energy consumption to break the bond between aminosilane and CO₂ molecules [35, 36].

The relationship between the fraction of mesopore/micropore volume and the CO₂ adsorption capacity of all samples is represented in Figure 10. The CO₂ adsorption capacities were increased gradually with the fraction of mesopore volume, whereas the CO₂ adsorption capacities of r6 samples were exceptions. The CO₂ adsorption capacities likely depend on the fraction of mesopore volume and pore size rather than the surface area and pore volume. The presence of well-developed mesopore is essential for optimum packing of the CO₂ molecules at room temperature and pressure. Therefore, a strategy for well-developed mesopore structures and amine functionalization is essential to obtain superior performance for CO₂ capture.

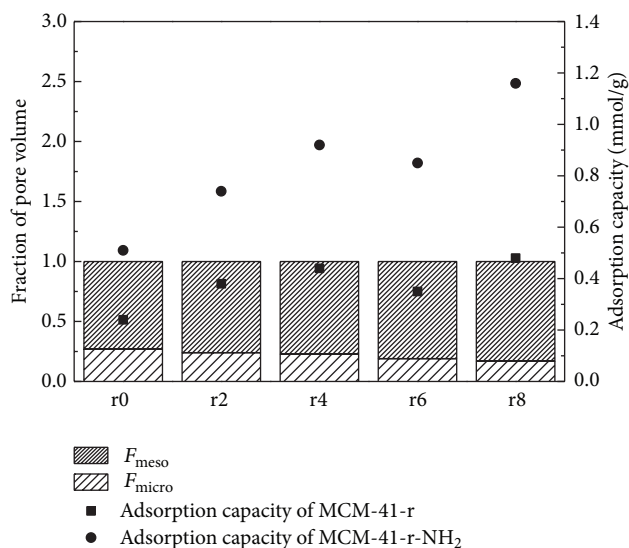


FIGURE 10: Relationship between the fraction of mesopore/micropore volume and the CO₂ adsorption capacity of MCM-41-r and MCM-41-r-NH₂.

4. Conclusion

Pore-expanded MCM-41s were prepared by 1,3,5-trimethylbenzene as the swelling agent to develop promising large pore CO₂ capture adsorbent materials. The design for the pore size was possible by controlling the molar ratio between the swelling agent and template agent. The highest CO₂ adsorption capacity for MCM-41-r8 was 0.48 mmol/g which was 1.7 times more than the original MCM-41. In addition, MCM-41-r8-NH₂ exhibited the highest adsorption capacity and adsorption rate of 1.16 mmol/g and 4.28%/min, respectively. The adsorption heat values for pore-expanded MCM-41 were in the range of -11.68 and -25.15 kJ/mol. It indicated that the reactions are exothermic and belong to physical adsorption. The adsorption heats of APETS-grafted MCM-41 and pore-expanded MCM-41 were larger than 40 kJ/mol which means chemical adsorption. More energy was needed in the regeneration process to break the bond between aminosilane and CO₂ for APTES-grafted pore-expanded MCM-41s since they could not desorb all the CO₂ molecules completely. In addition, the CO₂ adsorption capacity was strongly affected not by surface area and pore volume but by pore size and mesopore volume fraction. Therefore, modified mesoporous MCM-41 materials with a suitable pore size for CO₂ molecules are expected to be excellent solid adsorbents for achieving high CO₂ adsorption capacity if regeneration requirements could be minimized.

Conflict of Interests

The authors declare that there is no conflict of interests regarding the publication of this paper.

Acknowledgments

The authors gratefully acknowledge the National Natural Science Foundation of China (91434120, 51172251), Shanxi Province Coal-based Key Scientific and Technological Project (MD2014-09, MD2014-03), and Fundamental Research Funds for the Central Universities (2014ZD06). Thanks are due to Dr. Kaixi Li for assistance with the experiments and valuable discussion.

References

- [1] A. Somy, M. R. Mehrnia, H. D. Amrei, A. Ghanizadeh, and M. Safari, "Adsorption of carbon dioxide using impregnated activated carbon promoted by Zinc," *International Journal of Greenhouse Gas Control*, vol. 3, no. 3, pp. 249–254, 2009.
- [2] T. D. Pham, Q. Liu, and R. F. Lobo, "Carbon dioxide and nitrogen adsorption on cation-exchanged SSZ-13 zeolites," *Langmuir*, vol. 29, no. 2, pp. 832–839, 2013.
- [3] C. H. Lee, S. W. Park, and S. S. Kim, "Breakthrough analysis of carbon dioxide adsorption on zeolite synthesized from fly ash," *Korean Journal of Chemical Engineering*, vol. 31, no. 2, pp. 179–187, 2014.
- [4] R. S. Franchi, P. J. E. Harlick, and A. Sayari, "Applications of pore-expanded mesoporous silica. 2. Development of a high-capacity, water-tolerant adsorbent for CO₂," *Industrial and Engineering Chemistry Research*, vol. 44, no. 21, pp. 8007–8013, 2005.
- [5] H. Y. Huang, R. T. Yang, D. Chinn, and C. L. Munson, "Amine-grafted MCM-48 and silica xerogel as superior sorbents for acidic gas removal from natural gas," *Industrial & Engineering Chemistry Research*, vol. 42, no. 12, pp. 2427–2433, 2003.
- [6] F. Q. Liu, L. Wang, Z. Huang et al., "Amine-tethered adsorbents based on three-dimensional macroporous silica for CO₂ capture from simulated flue gas and air," *ACS Applied Materials & Interfaces*, vol. 6, no. 6, pp. 4371–4381, 2014.
- [7] A. Heydari-Gorji, Y. Belmabkhout, and A. Sayari, "Polyethylenimine-impregnated mesoporous silica: effect of amine loading and surface alkyl chains on CO₂ adsorption," *Langmuir*, vol. 27, no. 20, pp. 12411–12416, 2011.
- [8] A. Boonpoke, S. Chiarakorn, N. Laosiripojana, S. Towprayoon, and A. Chidthaisong, "Investigation of CO₂ adsorption by bagasse-based activated carbon," *Korean Journal of Chemical Engineering*, vol. 29, no. 1, pp. 89–94, 2012.
- [9] M. Gholami, M. R. Talaie, and S. F. Aghamiri, "Direct synthesis of bi-modal porous structure MCM-41 and its application in CO₂ capturing through amine-grafting," *Korean Journal of Chemical Engineering*, vol. 31, no. 2, pp. 322–326, 2014.
- [10] L. Wang and R. T. Yang, "Increasing selective CO₂ adsorption on amine-grafted SBA-15 by increasing silanol density," *Journal of Physical Chemistry C*, vol. 115, no. 43, pp. 21264–21272, 2011.
- [11] N. Gargiulo, A. Peluso, P. Aprea, F. Pepe, and D. Caputo, "CO₂ adsorption on polyethylenimine-functionalized SBA-15 mesoporous silica: isotherms and modeling," *Journal of Chemical and Engineering Data*, vol. 59, no. 3, pp. 896–902, 2014.
- [12] X. Wang, H. Li, H. Liu, and X. Hou, "AS-synthesized mesoporous silica MSU-1 modified with tetraethylenepentamine for CO₂ adsorption," *Microporous and Mesoporous Materials*, vol. 142, no. 2–3, pp. 564–569, 2011.
- [13] X. Yan, L. Zhang, Y. Zhang, K. Qiao, Z. Yan, and S. Komarneni, "Amine-modified mesocellular silica foams for CO₂ capture," *Chemical Engineering Journal*, vol. 168, no. 2, pp. 918–924, 2011.

- [14] R. Kishor and A. K. Ghoshal, "APTES grafted ordered mesoporous silica KIT-6 for CO₂ adsorption," *Chemical Engineering Journal*, vol. 262, pp. 882–890, 2015.
- [15] X. C. Xu, C. S. Song, J. M. Andresen, B. G. Miller, and A. W. Scaroni, "Novel polyethylenimine-modified mesoporous molecular sieve of MCM-41 type as high-capacity adsorbent for CO₂ capture," *Energy and Fuels*, vol. 16, no. 6, pp. 1463–1469, 2002.
- [16] A. Samanta, A. Zhao, G. K. Shimizu, P. Sarkar, and R. Gupta, "Post-combustion CO₂ capture using solid sorbents: a review," *Industrial & Engineering Chemistry Research*, vol. 51, no. 4, pp. 1438–1463, 2012.
- [17] Q. Cai, W. Y. Lin, F. S. Xiao, W. Q. Pang, X. H. Chen, and B. S. Zou, "The preparation of highly ordered MCM-41 with extremely low surfactant concentration," *Microporous and Mesoporous Materials*, vol. 32, no. 1-2, pp. 1–15, 1999.
- [18] C. T. Kresge, M. E. Leonowicz, W. J. Roth, J. C. Vartuli, and J. S. Beck, "Ordered mesoporous molecular sieves synthesized by a liquid-crystal template mechanism," *Nature*, vol. 359, no. 6397, pp. 710–712, 1992.
- [19] S. Loganathan, M. Tikmani, and A. K. Ghoshal, "Novel pore-expanded MCM-41 for CO₂ capture: synthesis and characterization," *Langmuir*, vol. 29, no. 10, pp. 3491–3499, 2013.
- [20] D. D. Das, P. J. E. Harlick, and A. Sayari, "Applications of pore-expanded MCM-41 silica: 4. Synthesis of a highly active base catalyst," *Catalysis Communications*, vol. 8, no. 5, pp. 829–833, 2007.
- [21] H. M. Zhao, D. Lin, G. Yang, Y. Chun, and Q. H. Xu, "Adsorption capacity of carbon dioxide on amine modified mesoporous materials with larger pore sizes," *Acta Physico-Chimica Sinica*, vol. 28, pp. 985–992, 2012.
- [22] A. Sayari, Y. Yang, M. Kruk, and M. Jaroniec, "Expanding the pore size of MCM-41 silicas: use of amines as expanders in direct synthesis and postsynthesis procedures," *Journal of Physical Chemistry B*, vol. 103, no. 18, pp. 3651–3658, 1999.
- [23] A. Corma, Q. Kan, M. T. Navarro, J. Pérez-Pariente, and F. Rey, "Synthesis of MCM-41 with different pore diameters without addition of auxiliary organics," *Chemistry of Materials*, vol. 9, no. 10, pp. 2123–2126, 1997.
- [24] D. Zhao, Q. Huo, J. Feng, B. F. Chmelka, and G. D. Stucky, "Nonionic triblock and star diblock copolymer and oligomeric surfactant syntheses of highly ordered, hydrothermally stable, mesoporous silica structures," *Journal of the American Chemical Society*, vol. 120, no. 24, pp. 6024–6036, 1998.
- [25] A. Wang and T. Kabe, "Fine-tuning of pore size of MCM-41 by adjusting the initial pH of the synthesis mixture," *Chemical Communications*, no. 20, pp. 2067–2068, 1999.
- [26] J. L. Blin and B. L. Su, "Tailoring pore size of ordered mesoporous silicas using one or two organic auxiliaries as expanders," *Langmuir*, vol. 18, no. 13, pp. 5303–5308, 2002.
- [27] D. M. Jiang, J. S. Gao, J. Yang, W. G. Su, Q. H. Yang, and C. Li, "Mesoporous ethane-silicas functionalized with *trans*-(1*R*,2*R*)-diaminocyclohexane: relation between structure and catalytic properties in asymmetric transfer hydrogenation," *Microporous and Mesoporous Materials*, vol. 105, no. 1-2, pp. 204–210, 2007.
- [28] S. Loganathan, M. Tikmani, and A. K. Ghoshal, "Pore-expanded MCM-41 for CO₂ adsorption: experimental and isotherm modeling studies," *Chemical Engineering Journal*, vol. 280, pp. 9–17, 2015.
- [29] R. Serna-Guerrero, Y. Belmabkhout, and A. Sayari, "Further investigations of CO₂ capture using triamine-grafted pore-expanded mesoporous silica," *Chemical Engineering Journal*, vol. 158, no. 3, pp. 513–519, 2010.
- [30] S. K. Jana, A. Mochizuki, and S. Namba, "Progress in pore-size control of mesoporous MCM-41 molecular sieve using surfactant having different alkyl chain lengths and various organic auxiliary chemicals," *Catalysis Surveys from Asia*, vol. 8, no. 1, pp. 1–13, 2004.
- [31] A. Olea, E. S. Sanz-Pérez, A. Arencibia, R. Sanz, and G. Calleja, "Amino-functionalized pore-expanded SBA-15 for CO₂ adsorption," *Adsorption*, vol. 19, no. 2–4, pp. 589–600, 2013.
- [32] Q. Wu, F. Zhang, J. Yang, Q. Li, B. Tu, and D. Zhao, "Synthesis of ordered mesoporous alumina with large pore sizes and hierarchical structure," *Microporous and Mesoporous Materials*, vol. 143, no. 2-3, pp. 406–412, 2011.
- [33] M. M. Dubinin, "The potential theory of adsorption of gases and vapors for adsorbents with energetically nonuniform surfaces," *Chemical Reviews*, vol. 60, no. 2, pp. 235–241, 1960.
- [34] J. S. Lettow, Y. J. Han, P. Schmidt-Winkel et al., "Hexagonal to mesocellular foam phase transition in polymer-templated mesoporous silicas," *Langmuir*, vol. 16, no. 22, pp. 8291–8295, 2000.
- [35] M. T. Ho, G. W. Allinson, and D. E. Wiley, "Factors affecting the cost of capture for Australian lignite coal fired power plants," *Energy Procedia*, vol. 1, no. 1, pp. 763–770, 2009.
- [36] J. Oexmann and A. Kather, "Post-combustion CO₂ capture in coal-fired power plants: comparison of integrated chemical absorption processes with piperazine promoted potassium carbonate and MEA," *Energy Procedia*, vol. 1, no. 1, pp. 799–806, 2009.

Research Article

An Investigation of Fractal Characteristics of Marine Shales in the Southern China from Nitrogen Adsorption Data

Jian Xiong,¹ Xiangjun Liu,^{1,2} and Lixi Liang²

¹School of Geoscience and Technology, Southwest Petroleum University, Chengdu 610500, China

²State Key Laboratory of Oil and Gas Reservoir Geology and Exploitation, Southwest Petroleum University, Chengdu 610500, China

Correspondence should be addressed to Jian Xiong; 361184163@qq.com

Received 3 April 2015; Accepted 29 July 2015

Academic Editor: Talhi Oualid

Copyright © 2015 Jian Xiong et al. This is an open access article distributed under the Creative Commons Attribution License, which permits unrestricted use, distribution, and reproduction in any medium, provided the original work is properly cited.

We mainly focus on the Permian, Lower Cambrian, Lower Silurian, and Upper Ordovician Formation; the fractal dimensions of marine shales in southern China were calculated using the FHH fractal model based on the low-pressure nitrogen adsorption analysis. The results show that the marine shales in southern China have the dual fractal characteristics. The fractal dimension D_1 at low relative pressure represents the pore surface fractal characteristics, whereas the fractal dimension D_2 at higher relative pressure describes the pore structure fractal characteristics. The fractal dimensions D_1 range from 2.0918 to 2.718 with a mean value of 2.4762, and the fractal dimensions D_2 range from 2.5842 to 2.9399 with a mean value of 2.8015. There are positive relationships between fractal dimension D_1 and specific surface area and total pore volume, whereas the fractal dimensions D_2 have negative correlation with average pore size. The larger the value of the fractal dimension D_1 is, the rougher the pore surface is, which could provide more adsorption sites, leading to higher adsorption capacity for gas. The larger the value of the fractal dimension D_2 is, the more complicated the pore structure is, resulting in the lower flow capacity for gas.

1. Introduction

With the increase of the global energy demands and the importing of advanced techniques, the unconventional gas reservoirs (including tight sands, coal bed methane, and shale gas) have gradually been the focus of exploration and development in many countries such as Canada, China, and Europe [1, 2], especially in China [3]. Shale gas, as one kind of unconventional gas reservoirs, is not only an important energy supplement but also a clean and green energy. In 2011, the “World Shale Gas Resources: An Initial Assessment of 14 Regions Outside the United States,” conducted by the U.S. DOE’s Energy Information Administration, evaluates the risk technically recoverable of shale gas resource to be $36.1 \times 10^8 \text{ m}^3$ in China and $19.6 \times 10^8 \text{ m}^3$ in Sichuan Basin, located in Southwest China [4]. And according to “the nation survey and devaluation of shale gas resource and favorable area selection,” issued by the Ministry of Land and Resources of the People’s Republic of China, the risk technically recoverable of shale gas reservoir is estimated to be approximately $25.08 \times 10^{12} \text{ m}^3$ in China and $14.58 \times 10^{12} \text{ m}^3$

in southern China. Some studies also suggested that there is a great development potential of shale gas resources in southern China [3, 5].

To reduce exploration risk and determine economic feasibility, considerable efforts are being undertaken to understand the knowledge of storage mechanism of shale gas and transport mechanisms of shale gas [6, 7], and pore structure of shale has a significant influence on storage mechanism and transport mechanisms. Therefore, the complex pore structure of shale is an important research field. To understand the complex pore structure of marine shales in southern China, researchers have utilized several measurement techniques to characterize the characteristics of pore structure of marine shales in southern China. Many methods such as scanning electron microscopy, field emission scanning electron microscopy, transmission electron microscopy, focused ion beam scanning electron microscopy, low-pressure gas adsorption analyses, mercury injection capillary pressure, and small-angle neutron scattering have been used to investigate characteristics of pore structure [6–16]. Among these, low-pressure nitrogen (N_2) adsorption

TABLE 1: Shale samples properties.

Region	Number	Age/formation	Types	Source
Changning-Xingwen area, Sichuan Province	L1			
	L2			
	L3		Core	[1, 8]
	L4			
	L5			
	L6			
	L7			
Changning area, Sichuan Province	L8	Lower Silurian		
	L9	Longmaxi		
	L10	Formation	Core	In this study
	L11			
	L12			
	L13			
	L14			
Shizhu area, Chongqing	L15		Outcrop	In this study
	L16			
	L17			
	L18			
Wuhu area, Anhui Province	G1	Lower Permian		
	G2	Gufeng	Core	[11]
	G3	Formation		
	G4			
Sichuan Basin	N1			
	N2	Lower Cambrian		
	N3	Niutitang	Core	[7, 13, 14]
	N4	Formation		
	N5			
Well Yuke 1, southern Chongqing	N6			
	N7			
	N8			
	N9			
	N10	Lower Cambrian		
	N11	Niutitang	Core	[10, 15]
	N12	Formation		
Well Youke 1, southern Chongqing	N13			
	N14			
	N15			
	N16			
	N17			
Qilongcun section, Xishui contry, Guizhou Province	WL1	Upper		
	WL2	Ordovician		
	WL3	Wufeng		
	WL4	Formation-	Outcrop	[24]
	WL5	Lower Silurian		
	WL6	Longmaxi		
	WL7	Formation		

TABLE 1: Continued.

Region	Number	Age/formation	Types	Source
	WL8			
	WL9			
	WL10			
	WL11			
	WL12			
	WL13			
	WL14			

analysis had been proven to be an effective method to characterize pore structures of shale [10–16]. In addition, the N_2 adsorption data had also been used to investigate the fractal characteristics of sands or coals [17–20]. There are only few reports on the fractal characteristics of shales from the Lower Cambrian Niutitang Formation in Sichuan Basin of China [7] and from the Chang-7 of the Upper Triassic Yanchang Formation in the Ordos Basin of China [16].

Compared with the extensive investigations on the fractal characteristics of sandstones and coals [17–22], similar studies on the fractal characteristics of shale in China have only received attention in recent years [7, 16]. There are several sets of marine shales with rich organic matter in southern China, including the Lower Cambrian, Upper Ordovician, Lower Silurian, and Lower Permian shale [5, 23], and those shale gas reservoirs in southern China are regarded as the main area for shale gas development [3, 23]. The objectives of the paper are to apply the fractal theory to investigate the irregularity of pore structure and study the fractal characteristics of marine shales in southern China based on the nitrogen adsorption analysis. And a parameter, fractal dimension, can be adopted to describe the fractal characteristics, which was calculated by the fractal Frenkel-Halsey-Hill (FHH) model from the N_2 adsorption data. Meanwhile, the relationships between pore structure parameters and fractal dimension have been investigated, and the relationships between fractal dimension and adsorption capacity and flow capacity of shale are also discussed. It was anticipated that our research provides the critical data presenting the fractal characteristics of the marine shales in southern China and understanding the influence of the fractal dimension on the adsorption capacity and flow capacity of the marine shales in southern China.

2. Samples and Methods

In order to investigate the fractal characteristics of marine shales with rich organic matter in southern China, four geological ages and formations are selected for the research objects, including the Lower Cambrian Niutitang Formation, Upper Ordovician Wufeng Formation, Lower Silurian Longmaxi Formation, and Lower Permian Gufeng Formation. The sample number, age, formation, and types are shown in Table 1. Part of shale samples is obtained from the Lower Silurian Longmaxi Formation in Changning area of Sichuan Province and Shizhu area of Chongqing, located in southern

China. And the obtained samples were characterized by low-pressure N_2 adsorption analysis and permeability analysis. In addition, more detailed information on low-pressure N_2 adsorption analysis, permeability analysis, and high-pressure methane adsorption analysis of the other part of shale samples can be gained in [1, 7, 8, 10, 11, 13–15, 24].

Low-pressure N_2 adsorption analysis was measured on a Quadrasorb SI Surface Area Analyzer and Pore Size Analyzer at the temperature of liquid nitrogen following Chinese National Standard (GB/T) 19587-2004 and (GB/T) 21650.2-2008. Shale samples were crushed to grains of 60–80 mesh size and then outgassed at 378 K for 24 h. For all samples, nitrogen adsorption isotherms at 77 K were measured for the relative pressure ranging from 0.01 to 0.99. The specific surface area was calculated using the Brunauer-Emmett-Teller (BET) method [25], and the total pore volume was estimated to be the liquid volume of nitrogen at a relative pressure of 0.98.

The permeability of core plug samples was measured following the Chinese Oil and Gas Industry Standard (SY/T) 5336-1996. Permeability measurements were conducted using a pulse-decay permeability measurement (Low Gas Permeability Measurement 700) with nitrogen as the medium.

Fractal analysis can be used to describe the geometric and structural properties of the solid surface [26, 27], and the quantitative evaluation of the fractal geometry was to use a parameter, the fractal dimension D , which was used as an index of pore surface roughness or pore structure complexity of the solid [27]. That is to say, the solid with more fractal dimension D has more complicated pore structure or irregular pore surface. Based on the N_2 adsorption data, the fractal dimension can be determined by applying the Frenkel-Halsey-Hill (FHH) equation [27], and the FHH model can be described as follows [22, 27, 28]:

$$\ln(V) = (D - 3) \ln\left(\ln\left(\frac{p_0}{p}\right)\right) + \text{constant}, \quad (1)$$

where V is the volume of N_2 adsorbed at each equilibrium pressure p ; p_0 is the saturation pressure; and D is the fractal dimension. Thus, according to the fractal FHH model, a plot of $\ln(V)$ versus $\ln(\ln(p_0/p))$ shows a linear relationship, and the slope may be used to calculate the fractal dimension D .

3. Results and Discussions

3.1. Pore Structure Parameters and Permeability. The results from the low-pressure N_2 adsorption analysis are shown in Table 2. From Table 2, we observe that pore structure parameters of marine shales in southern China exhibit a wide range. The specific surface area calculated from the N_2 adsorption data using the BET model ranges from 1.6545 to 32.5015 m^2/g with a mean value of 15.4417 m^2/g . The nitrogen adsorption volume at p/p_0 , about 0.98, can be used to estimate total pore volume and mean pore size. The total pore volume varies from 0.00195 to 0.04374 cm^3/g with an average of 0.00209 cm^3/g , and average pore size generally is in the range of 3.567–9.723 nm with an average of 5.7215 nm, which belongs to mesopore according to the International Union

TABLE 2: Pore structure parameters of shale samples from N_2 adsorption isotherms.

Number	Total pore volume (cm^3/g)	Specific surface area (m^2/g)	Monolayer volume (cm^3/g) ^a	Average pore size (nm) ^b
L1	0.03074	18.821	0.006685	6.532
L2	0.03313	16.509	0.005864	8.028
L3	0.02744	19.592	0.006959	5.602
L4	0.02246	15.593	0.005539	5.762
L5	0.02297	9.885	0.003511	9.296
L6	0.02823	16.881	0.005996	6.690
L7	0.01263	7.147	0.002539	7.069
L8	0.01176	6.354	0.002257	7.404
L9	0.01417	7.991	0.002839	7.095
L10	0.01602	12.458	0.004425	5.144
L11	0.01962	12.030	0.004273	6.524
L12	0.02504	14.817	0.005263	6.760
L13	0.01776	13.290	0.004721	5.345
L14	0.01769	17.358	0.006166	4.076
L15	0.01785	16.719	0.005939	4.271
L16	0.01754	16.130	0.005730	4.349
L17	0.01674	16.441	0.005840	4.074
L18	0.01700	16.993	0.006036	4.002
G1	0.02268	9.330	0.003314	9.723
G2	0.03582	19.707	0.007000	7.270
G3	0.04374	24.236	0.008609	7.219
G4	0.04097	22.473	0.007982	7.292
N1	0.03810	32.501	0.011545	4.689
N2	0.03466	25.529	0.009068	5.431
N3	0.01443	7.310	0.002597	7.897
N4	0.01908	8.361	0.002970	9.128
N5	0.02636	12.241	0.004348	8.616
N6	0.01596	11.522	0.004093	5.539
N7	0.01463	12.708	0.004514	4.605
N8	0.02181	23.903	0.008491	3.649
N9	0.02408	27.001	0.009591	3.567
N10	0.00195	1.645	0.000584	4.749
N11	0.00272	2.760	0.000981	3.947
N12	0.00528	4.770	0.001694	4.424
N13	0.00327	1.969	0.000699	6.638
N14	0.00520	3.615	0.001284	5.757
N15	0.00414	2.464	0.000875	6.718
N16	0.01894	20.172	0.007165	3.755
N17	0.00548	2.755	0.000979	7.951
WL1	0.03652	30.101	0.010692	4.853
WL2	0.02327	20.838	0.007402	4.467
WL3	0.01267	10.750	0.003818	4.716
WL4	0.02802	22.616	0.008033	4.956
WL5	0.02652	24.178	0.008588	4.387

TABLE 2: Continued.

Number	Total pore volume (cm ³ /g)	Specific surface area (m ² /g)	Monolayer volume (cm ³ /g) ^a	Average pore size (nm) ^b
WL6	0.02577	23.487	0.008343	4.389
WL7	0.02420	20.779	0.007381	4.658
WL8	0.01992	16.694	0.005930	4.773
WL9	0.02391	22.12	0.007857	4.324
WL10	0.02433	22.321	0.007929	4.360
WL11	0.02993	17.34	0.006159	6.904
WL12	0.02194	19.528	0.006936	4.494
WL13	0.02092	18.65	0.006625	4.488
WL14	0.02174	17.027	0.006048	5.106

^aThe monolayer volume is calculated by BET method [25]. ^bAverage pore size = $4 * \text{Total pore volume} / \text{specific surface area}$.

of Pure and Applied Chemistry (IUPAC) classification [29]. The marine shales in southern China are similar to the North American shales in terms of specific surface area and total pore volume [6, 30, 31].

The permeability and Langmuir volume of marine shale samples are illustrated in Table 3. From Table 3, the pulse-decay permeability values of marine shale samples are commonly less than $1\mu\text{D}$. Permeability values of these shale samples were lower than the Besa River, Muskwa, and Fort Simpson shale from Northeastern British Columbia [32]. And permeability values of these shale samples were bigger than the Barnett shale from Fort Worth Basin [33], which may be related to types of samples for measuring. Type of marine shale samples in southern China for measuring permeability was core plug, whereas type of Barnett shale samples was crushed sample. In addition, we observe that the difference of Langmuir volume of shale samples from the different references was great, which may be related to the experiment conditions of shale samples.

3.2. N_2 Adsorption-Desorption Isotherms. The isotherms for the low-pressure N_2 adsorption analysis of some shale samples are listed in Figure 1. The isotherm of each shale sample has difference in shape, while the isotherm of all shale samples belongs to type IV isotherms according to the BDDT classification [34]. The adsorption branch and the desorption branch of N_2 adsorption-desorption isotherm at higher relative pressure (more than 0.45) exist separation because of capillary condensation, resulting in a hysteresis loop [35], which mean that shale samples contain mesopore [36]. Meanwhile, from the figure, we can note that the absence of total closure of the hysteresis loop of shale samples L2 and L7 was interpreted as being due to the effect of swelling [35].

The shape of the hysteresis loop can be used to understand the pore shape of shale [36]. According to the hysteresis loop shape of N_2 adsorption-desorption isotherms, the shale samples can be divided into two groups: group A (sample L2, sample L7, and sample N2) and group B (sample N5, sample WL4, and sample WL11) (Figure 1 and Table 4). The adsorption-desorption isotherms of some shale samples

TABLE 3: Permeability and methane adsorption results for some shale samples.

Number	Permeability (μD)	Langmuir volume (cm ³ /g)	Source
L1	—	—	
L2	—	0.52	
L3	—	0.58	
L4	—	0.52	[1]
L5	—	0.43	
L6	—	0.51	
L7	0.6999	—	
L8	0.6039	—	
L9	0.7431	—	
L10	0.4142	—	In this study
L11	0.3502	—	
L12	0.3782	—	
L13	0.4264	—	
N1	0.40	13.44	
N2	0.32	12.10	[7]
N3	0.67	9.63	
N4	0.70	9.41	[7]
N5	0.55	4.03	
N6	—	3.34	
N7	—	2.43	
N8	—	4.36	
N9	—	5.04	
N10	—	2.01	
N11	—	1.83	
N12	—	2.62	[10]
N13	—	1.13	
N14	—	1.24	
N15	—	1.18	
N16	—	4.69	
N17	—	2.20	

belong to group A, which are reversible at low relative pressure, but, at higher relative pressure (more than 0.45), the desorption branches of the isotherms exist inflection point. And type of the hysteresis loops may be considered as type H2 according to the IUPAC classification [36]. Type H2 hysteresis loop is usually observed in open pores, which contain mainly inkbottle-shaped pores and a small amount of parallel-plate pores or cylindrical pores [7, 22, 36]. In contrast, at higher relative pressure (more than 0.45), the desorption branches of the isotherms of some shale samples belonging to group B do not exist inflection point. According to the IUPAC classification [36], type of the hysteresis loops may be classified as type H3, which is usually associated with slit-shaped pores [7, 22, 36].

3.3. Fractal Dimension from N_2 Adsorption Data. According to the fractal FHH model, the plots of $\ln(V)$ versus $\ln(\ln(p_0/p))$ from N_2 adsorption data are illustrated in Figure 2. From Figure 2, we observe that there are two distinct straight line segments at the whole relative pressure range,

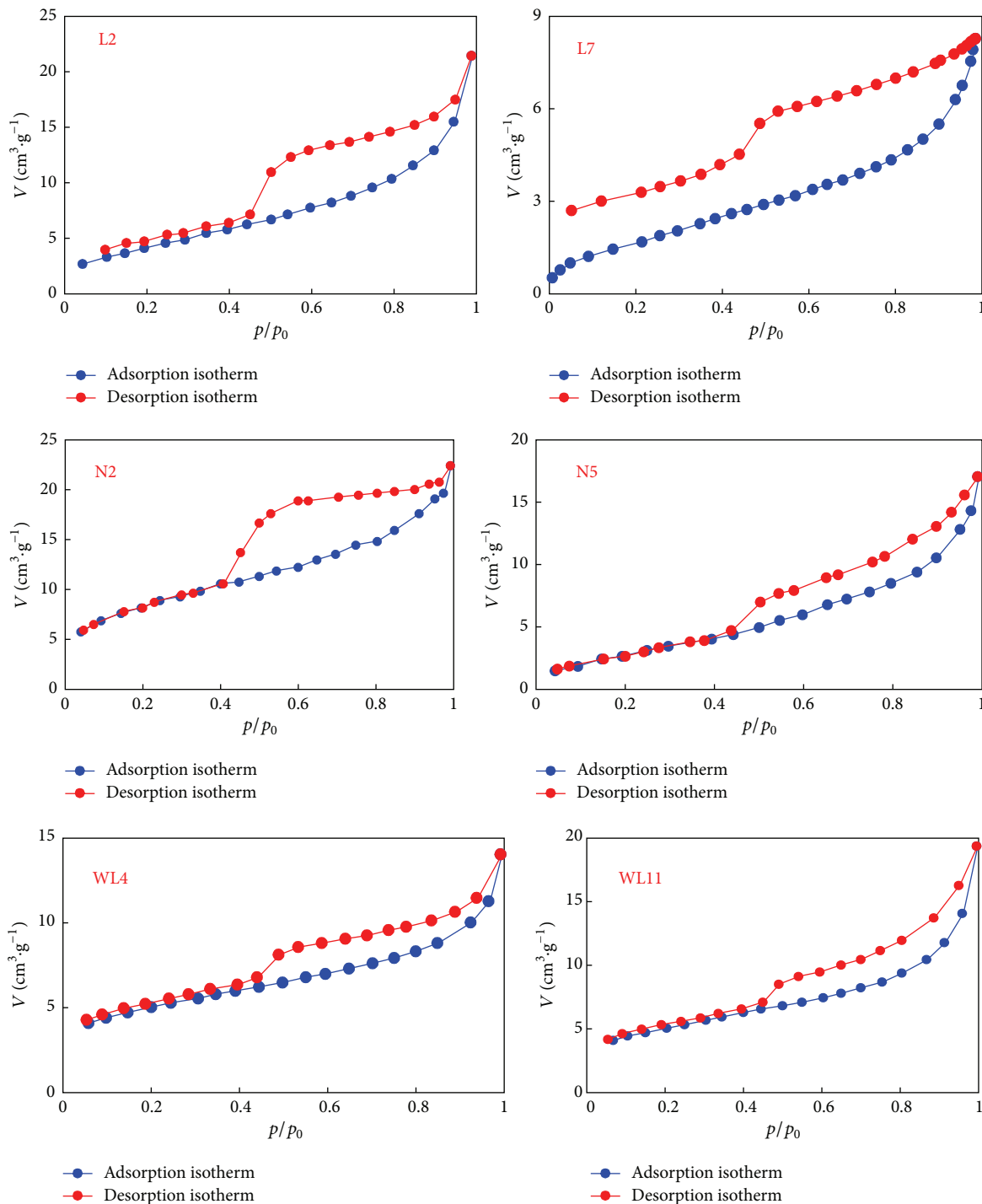


FIGURE 1: Low-pressure N_2 adsorption-desorption isotherms of some shale samples.

and the liners can obtain different slopes with piecewise fitting. A demarcation point between straight line segment at low relative pressure range and straight line segment at high relative pressure range can be gained, and the pores would be divided into small pores and large pores, respectively. Meanwhile, both of them show good fitting, suggesting that the fractal characteristics at the two intervals are different, and the fractal dimensions D_1 and D_2 are calculated from

the two linear segments (Table 4). From Table 4, we observe that all correlation coefficients are more than 0.94, suggesting that there are the fractal characteristics for marine shales in southern China. Values of fractal dimension D_1 range from 2.0918 to 2.718 with a mean value of 2.4762, and values of fractal dimension D_2 range from 2.5842 to 2.9399 with a mean value of 2.8015, indicating that there are irregular pore surface and sophisticated pore structure in shales.

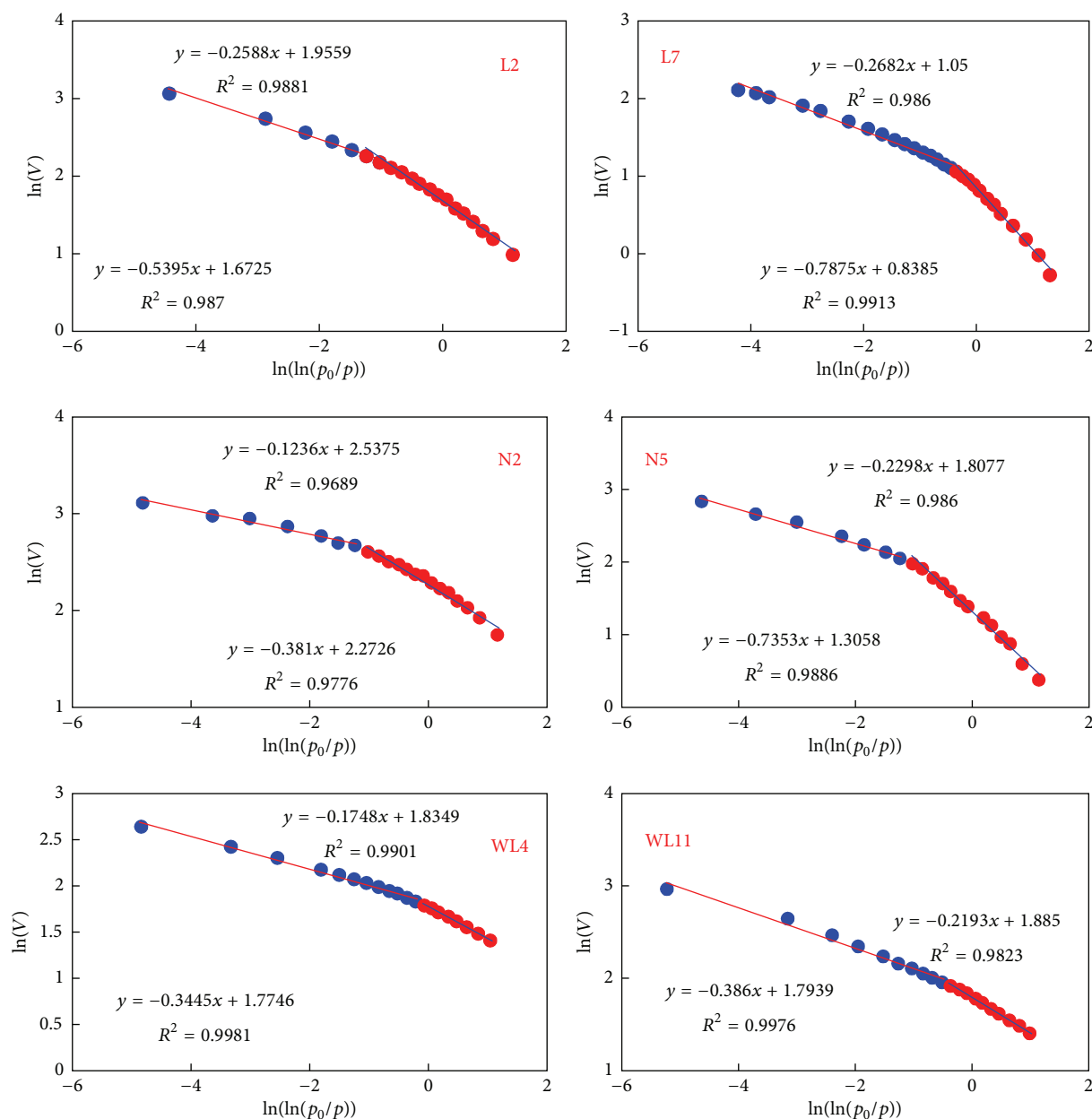


FIGURE 2: Plots of $\ln(V)$ versus $\ln(\ln(p_0/p))$ reconstructed from the N_2 adsorption data of some shale samples.

The value of fractal dimension D_1 is generally less than fractal dimension D_2 , indicating that the complexity of pore structure of large pore is more than that of small pore. This conclusion is consistent with previous work on coals and sandstones [21, 22]. In addition, Figure 3 reports that no clear correlation between fractal dimension D_1 and fractal dimension D_2 is observed, suggesting that they represent two different fractal dimensions of marine shales in southern China. This conclusion shows that the marine shales have double fractal characteristics, which is in disagreement with the previous study on the continental shales [16]. This is may be related to the continental shales that included a small amount of micropores.

From Table 4, we also observe that the fractal dimension D_1 ranges from 2.0918 to 2.693 with an average of 2.4339 and

the fractal dimension D_2 ranges from 2.713 to 2.9399 with an average of 2.8144 in group A and the fractal dimension D_1 ranges from 2.2438 to 2.718 with an average of 2.5654 and the fractal dimension D_2 ranges from 2.5842 to 2.8692 with an average of 2.7762 in group B. Comparisons of fractal dimension D_1 and fractal dimension D_2 of shale in groups A and B are shown in Figure 4. Comparing samples in groups A and B (Figure 4), the minimum, average, and maximum of fractal dimension D_1 in group A are smaller than those in group B; the minimum, average, and maximum of fractal dimension D_2 in group A are greater than those in group B. The hysteresis loop shape of shale samples in group A can be considered as type H2, which occurs mainly in inkbottle-shaped pores, whereas the hysteresis loop shape of shale samples in group B can be considered as type H3, which

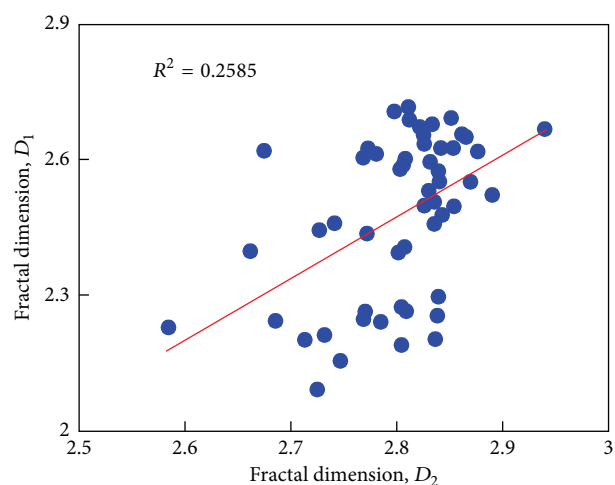
TABLE 4: Fractal dimensions derived from fractal FHH model.

Number	D_1	Coefficient (R^2)	D_2	Coefficient (R^2)	Group ^a
L1	2.6896	0.9981	2.812	0.9788	A
L2	2.4605	0.987	2.7412	0.9881	A
L3	2.6734	0.9982	2.8218	0.9899	B
L4	2.58	0.9836	2.8033	0.9978	B
L5	2.2438	0.9944	2.6854	0.9917	B
L6	2.6261	0.9918	2.7729	0.9956	B
L7	2.2125	0.9913	2.7318	0.986	A
L8	2.0918	0.9959	2.7248	0.979	A
L9	2.1558	0.9857	2.7467	0.9724	A
L10	2.2654	0.9785	2.8091	0.971	A
L11	2.2039	0.9416	2.8364	0.9718	A
L12	2.2978	0.9134	2.8395	0.9785	A
L13	2.1908	0.9254	2.8044	0.9795	A
L14	2.5074	0.9905	2.8355	0.9649	A
L15	2.5324	0.991	2.8303	0.9753	A
L16	2.4979	0.958	2.8541	0.9471	A
L17	2.4588	0.9915	2.8356	0.9544	A
L18	2.4784	0.9838	2.8429	0.9789	A
G1	2.3986	0.9815	2.6615	0.9906	B
G2	2.621	0.9841	2.6746	0.9901	B
G3	2.718	0.9796	2.8109	0.979	B
G4	2.708	0.987	2.7977	0.9902	B
N1	2.6687	0.9652	2.9399	0.9807	A
N2	2.619	0.9769	2.8764	0.9689	A
N3	2.4077	0.9865	2.8075	0.9563	A
N4	2.4372	0.9565	2.7718	0.9471	A
N5	2.2647	0.9887	2.7702	0.986	B
N6	2.6032	0.9878	2.808	0.9932	A
N7	2.5529	0.9893	2.8402	0.9745	A
N8	2.6577	0.9879	2.8615	0.9671	A
N9	2.6515	0.9885	2.8654	0.9575	A
N10	2.2483	0.9771	2.7687	0.9719	A
N11	2.3956	0.9757	2.8015	0.993	A
N12	2.4447	0.9939	2.7269	0.9972	A
N13	2.2019	0.9783	2.713	0.9878	A
N14	2.2416	0.9992	2.7849	0.9949	A
N15	2.2559	0.9904	2.8384	0.9935	A
N16	2.5229	0.9747	2.8901	0.9649	A
N17	2.2298	0.9935	2.5842	0.9823	B
WL1	2.693	0.9954	2.8513	0.9622	A
WL2	2.6797	0.9968	2.8336	0.9926	A
WL3	2.2749	0.9863	2.8044	0.9786	A
WL4	2.6555	0.9981	2.8252	0.9901	A
WL5	2.6358	0.9859	2.8259	0.9453	A
WL6	2.6267	0.996	2.8533	0.9632	B
WL7	2.6055	0.9962	2.7681	0.9902	B

TABLE 4: Continued.

Number	D_1	Coefficient (R^2)	D_2	Coefficient (R^2)	Group ^a
WL8	2.4996	0.9962	2.8259	0.9902	A
WL9	2.5891	0.9864	2.8062	0.9821	B
WL10	2.6265	0.9972	2.8418	0.975	B
WL11	2.614	0.9976	2.7807	0.9823	B
WL12	2.5759	0.9652	2.8395	0.958	B
WL13	2.5519	0.9981	2.8698	0.9565	B
WL14	2.5966	0.9858	2.8316	0.9683	B

^aTypes of adsorption-desorption isotherms are divided into group A and group B.

FIGURE 3: Relationship between fractal dimension D_1 and fractal dimension D_2 .

is usually associated with slit-shaped pores. And the pore structure of shale samples in group A is more complicated than that in group B. Therefore, the fractal dimension D_2 at higher relative pressure may be used to characterize the complexity of pore structure in shales, which is in agreement with previous study on coals [22], suggesting that the fractal dimension D_2 at higher relative pressure represents the complexity of pore structure in coals.

3.4. Relationships between Fractal Dimension and Pore Structure Parameters. The relationships between fractal dimension and pore structure parameters (specific surface area, total pore volume, and average pore size) are listed in Figure 5. From Figure 5, we observe that there is good positive correlation between the fractal dimension D_1 and specific surface area ($R^2 = 0.6584$ in Figure 5(a)) and moderate positive correlation between the fractal dimension D_1 and total pore volume ($R^2 = 0.472$ in Figure 5(b)). However, the fractal dimension D_2 has a poor positive relationship with specific surface area ($R^2 = 0.3622$ in Figure 5(a)) and no obvious relationship with total pore volume ($R^2 = 0.0756$ in Figure 5(b)). The good or moderate positive relationships indicate that shale with a higher total pore volume or specific

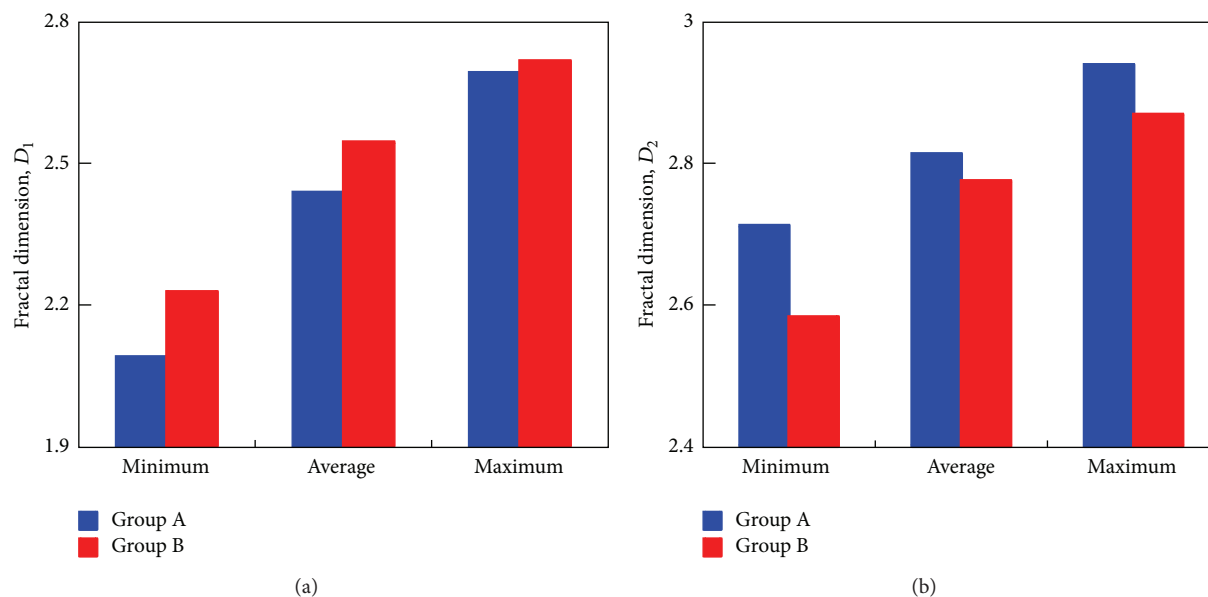


FIGURE 4: Comparison of fractal dimension D_1 and fractal dimension D_2 of shale in groups A and B.

surface area may have a greater fractal dimension D_1 . This finding is in agreement with previous research on coals [22]. Meanwhile, we also observe that there is a good positive relationship between fractal dimension D_1 and monolayer volume ($R^2 = 0.6584$ in Figure 5(c)), whereas a poor positive relationship between fractal dimension D_2 and monolayer volume ($R^2 = 0.3622$ in Figure 5(c)), indicating that shale with a higher monolayer volume would have more roughness pore surface and higher fractal dimension D_1 . In addition, the relationship between fractal dimension and average pore size is shown in Figure 5(d). From this figure, the fractal dimension D_1 has a moderate negative correlation with the average pore size ($R^2 = 0.4321$ in Figure 5(d)), while the fractal dimension D_2 has a poor negative correlation with the average pore size ($R^2 = 0.1465$ in Figure 5(d)), suggesting that the fractal dimension D_2 decreases with increasing average pore size. Shale with smaller average pore size would have more micropores [7] and higher fractal dimension D_2 , reflecting more complicated pore structure in shale.

Comparing the relationships in Figures 3–5, the fractal dimension D_1 at low relative pressure may reflect the surface fractal dimension, which may be used to characterize the roughness of pore surface of shale. However, the fractal dimension D_2 at higher relative pressure may represent the pore structure fractal dimension, which may be used to describe the complexity of pore structure of shale. From Table 4, we observe that the fractal dimension D_1 has large variable ranges, indicating that the surface of some pores in shale is regularity, whereas the surface of some pores is toughness. With the fractal dimension D_1 increasing, the pore surface in shale transforms gradually from smoothness to toughness, which suggests that the roughness of pore surface in shale exists difference, and the interaction potential energy between gas and soil surface shows uneven distribution, resulting in gas adsorption sites for gas in shale being inhomogeneous. Meanwhile, the fractal dimension D_2 has

little variable ranges, indicating that the discrepancies among fractal characteristic of pore structure of each shale sample are relatively low. A higher fractal dimension D_2 indicates that a shale sample has a more irregular pore structure.

3.5. Relationships between Fractal Dimension and Adsorption Capacity and Flow Capacity. The fractal dimension D_1 and fractal dimension D_2 represent the two different types of fractal characteristics of shale, which are pore surface fractal characteristics and pore structure fractal characteristics, respectively. Shale with a higher fractal dimension D_1 has a more rough pore surface, whereas shale with a higher fractal dimension D_2 has a more complicated pore structure. Relationships between fractal dimension and Langmuir volume of shale samples are shown in Figure 6. From this figure, there are significant positive correlations between fractal dimension D_1 and Langmuir volume from different literatures, which means that the adsorption capacity of shale increases with increasing fractal dimension D_1 , whereas fractal dimension D_2 has different relationships with Langmuir volume from different literatures. Therefore, the fractal dimension D_1 has greater influence on adsorption capacity of shale than the fractal dimension D_2 . This finding is in agreement with results from previous work on coals [22]. Shale with a higher fractal dimension D_1 has a more irregular pore surface that can provide more adsorption sites and the interface force between gas and the shale surface is greater, which would be beneficial to increase the adsorption amount of gas, leading to higher adsorption capacity of shale.

However, Yao et al. [19] and Cai et al. [20] suggested that the pore structure in coal had great effects on gas transport and coal with higher fractal dimension had less flow capacity. Chen et al. [21] studied the relationship between pore structure fractal dimension and permeability of sandstone and found that there was negative correlation

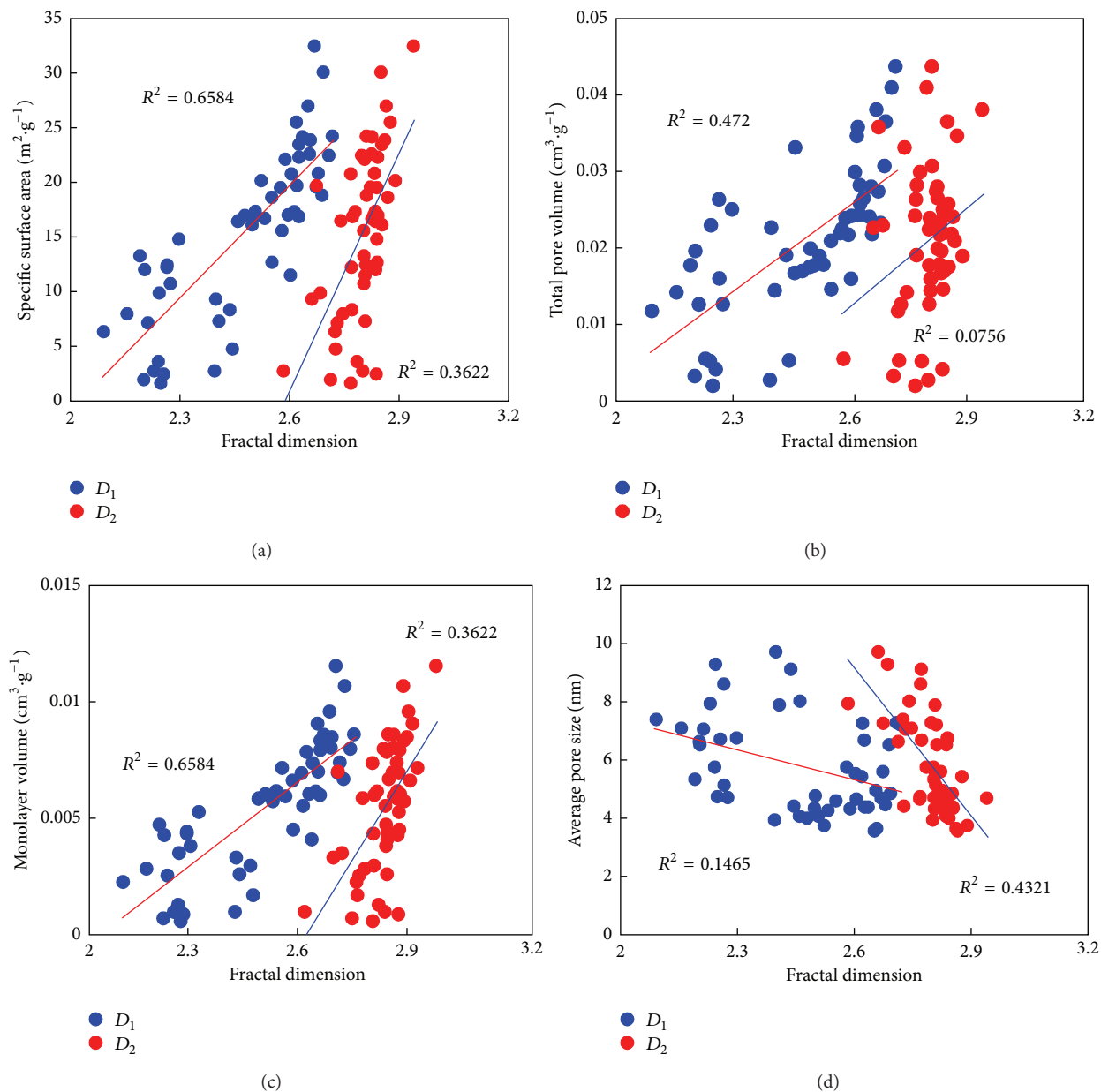


FIGURE 5: Relationships between fractal dimension and specific surface area (a), total pore volume (b), monolayer volume (c), and average pore size (d).

between pore structure fractal dimension and permeability, which mean that sandstone with a higher pore structure fractal dimension has more complex pore structure, resulting in lower permeability. Figure 7 reports relationship between fractal dimension and permeability of shale samples. There is a good-moderate negative relationship between fractal dimension D_1 and permeability ($R^2 = 0.5635$ in Figure 7), and the fractal dimension D_2 has a poor negative correlation with permeability ($R^2 = 0.1109$ in Figure 7). This finding suggests that the fractal dimension D_2 has greater influence on flow capacity of shale than the fractal dimension D_1 . Therefore, shale with a higher fractal dimension D_2 has more complicated pore structure, resulting in lower permeability

and flow capacity for gas, which makes gas adsorption, diffusion, and percolation much more difficult in shale.

Therefore, the two fractal dimensions have different impact on the development of shale gas reservoirs. Higher fractal dimension D_1 represents more roughness of pore surface of shale that offers more adsorption sites, leading to higher adsorption capacity of shale. However, higher fractal dimension D_2 represents more complicated pore structure, resulting in the decrease of permeability of shale, which makes gas adsorption, diffusion, and percolation become much more difficult. Comparing the influences of two fractal dimensions on the adsorption capacity and flow capacity, we consider higher surface fractal dimension D_1 and lower pore structure fractal dimension D_2 in shale as having

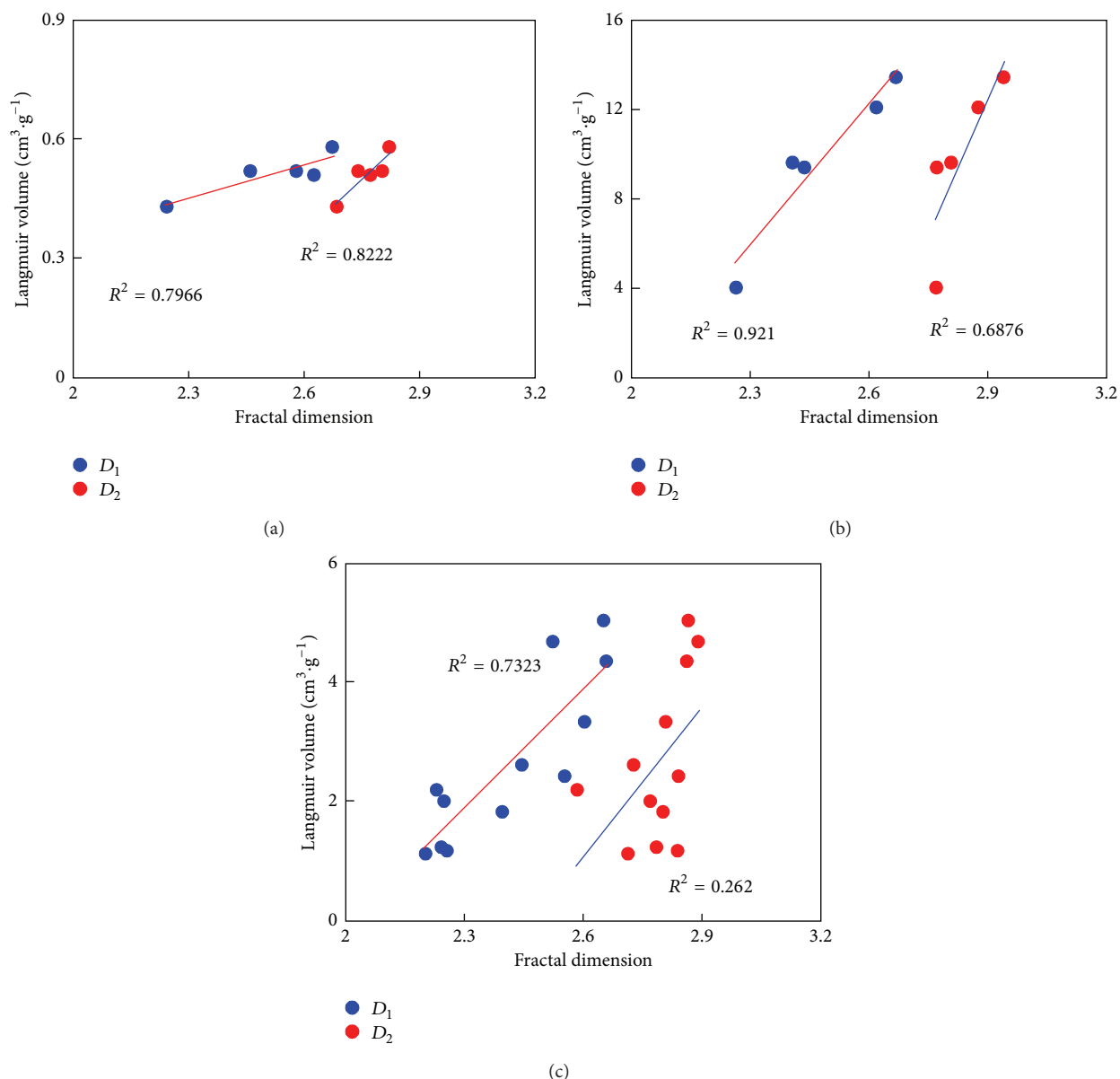


FIGURE 6: Relationships between fractal dimension and Langmuir volume (data in (a) from [1]; data in (b) from [7]; data in (c) from [10]).

higher adsorption capacity for gas and flow capacity for gas, which has an important significance in the development of shale gas reservoirs. In conclusion, shale with a greater fractal dimension D_1 has stronger adsorption capacity and should use stimulation treatment forming fracture networks to increase the flow capability for gas (decrease the fractal dimension D_2), which lead to accelerating velocity of gas desorption and increasing the gas production.

4. Conclusions

In this paper, the FHH fractal model has been applied to investigate the fractal characteristics of marine shales in southern China from nitrogen adsorption data. The relationships between pore structure parameters and fractal

dimension have been investigated. Furthermore, the relationships between fractal dimension and adsorption capacity and flow capacity of shale are also discussed. The following conclusions can be made:

- (1) The marine shales in southern China have two different types of fractal characteristics; the fractal dimension D_1 at low relative pressure represents the pore surface fractal characteristics and the fractal dimension D_2 at higher relative pressure describes the pore structure fractal characteristics.
- (2) The fractal dimensions D_1 range from 2.0918 to 2.718 with a mean value of 2.4762, and the fractal dimensions D_2 range from 2.5842 to 2.9399 with a mean value of 2.8015, indicating that there are irregular pore

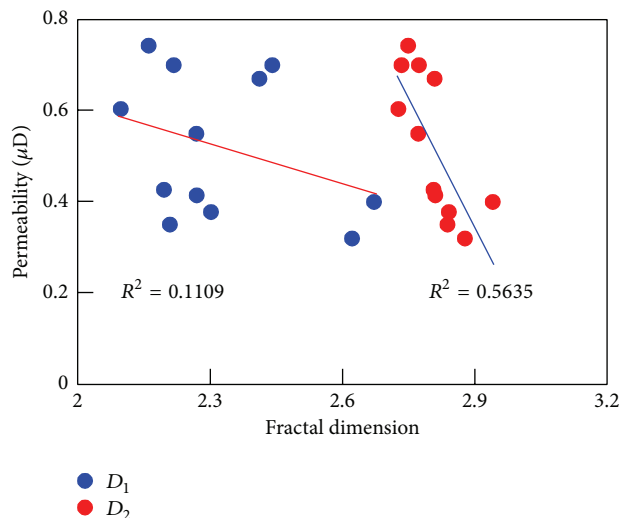


FIGURE 7: Relationship between fractal dimension and permeability.

surface and sophisticated pore structure in marine shales.

- (3) The fractal dimension D_1 has good or moderate positive relationships with specific surface area or total pore volume, whereas the fractal dimension D_2 shows moderate negative correlation with average pore size.
- (4) The higher fractal dimension D_1 represents more roughness of pore surface of shale that offers more adsorption sites, leading to higher adsorption capacity for gas in shale. However, the higher fractal dimension D_2 represents higher heterogeneity of pore structure and more complicated pore structure, resulting in the lower flow capacity for gas in shale.

Conflict of Interests

The authors declare that there is no conflict of interests regarding the publication of this paper.

Acknowledgments

The authors would like to give sincere thanks for the continuous supply of funds. This research was supported by the United Fund Project of National Natural Science Foundation of China (Grant no. U1262209), the National Natural Science Foundation of China (NSFC) (Grant no. 51274172), and the Young scholars development fund of SWPU.

References

- [1] S. Chen, Y. Zhu, H. Wang, H. Liu, W. Wei, and J. Fang, "Shale gas reservoir characterisation: a typical case in the southern Sichuan Basin of China," *Energy*, vol. 36, no. 11, pp. 6609–6616, 2011.
- [2] R. Weijermars, G. Drijkoningen, T. J. Heimovaara, E. S. J. Rudolph, G. J. Weltje, and K. H. A. A. Wolf, "Unconventional gas research initiative for clean energy transition in Europe," *Journal of Natural Gas Science and Engineering*, vol. 3, no. 2, pp. 402–412, 2011.
- [3] J. Li, M. Zheng, G. Zhang et al., "Potential and prospects of conventional and unconventional natural gas source in China," *Acta Petrolei Sinica*, vol. 33, supplement 1, pp. 89–98, 2012.
- [4] U.S. Energy Information Administration (EIA), *World Shale Gas Resources: An Initial Assessment of 14 Regions Outside the United States*, [EB/OL], 2011, <http://www.eia.gov/analysis/studies/worldshalegas>.
- [5] H. Wang, Y. Liu, D. Dong, Q. Zhao, and D. Du, "Scientific issues on effective development of marine shale gas in Southern China," *Petroleum Exploration and Development*, vol. 40, no. 5, pp. 574–579, 2013.
- [6] D. J. K. Ross and R. M. Bustin, "The importance of shale composition and pore structure upon gas storage potential of shale gas reservoirs," *Marine and Petroleum Geology*, vol. 26, no. 6, pp. 916–927, 2009.
- [7] F. Yang, Z. Ning, and H. Liu, "Fractal characteristics of shales from a shale gas reservoir in the Sichuan Basin, China," *Fuel*, vol. 115, pp. 378–384, 2014.
- [8] S. Chen, Y. Zhu, H. Wang, H. Liu, W. Wei, and J. Fang, "Structure characteristics and accumulation significance of nanopores in Longmaxi shale gas reservoir in the Southern Sichuan Basin," *Journal of China Coal Society*, vol. 24, no. 3, pp. 450–455, 2012.
- [9] J. Li, B. Yu, J. Zhang, Y. Li, and J. Wu, "Reservoir characteristics and their influence factors of the Lower Cambrian dark shale in Northern Guizhou," *Oil & Gas Geology*, vol. 33, no. 3, pp. 364–374, 2012.
- [10] S.-B. Han, J.-C. Zhang, C. Yang et al., "The characteristics of nanoscale pore and its gas storage capability in the Lower Cambrian shale of southeast Chongqing," *Journal of the China Coal Society*, vol. 38, no. 6, pp. 1038–1043, 2013.
- [11] L. Pan, G. Chen, Q. Xu, and X. Xiao, "Pore structure characteristics of Permian organic-rich shale in Lower Yangtze area," *Journal of the China Coal Society*, vol. 38, no. 6, pp. 787–793, 2013.
- [12] H. Tian, L. Pan, X. Xiao, R. W. T. Wilkins, Z. Meng, and B. Huang, "A preliminary study on the pore characterization of Lower Silurian black shales in the Chuandong Thrust Fold Belt, southwestern China using low pressure N_2 adsorption and FE-SEM methods," *Marine and Petroleum Geology*, vol. 48, pp. 8–19, 2013.
- [13] F. Yang, Z. Ning, C. Hu, B. Wang, K. Peng, and H. Liu, "Characterization of microscopic pore structures in shale reservoirs," *Acta Petrolei Sinica*, vol. 34, no. 2, pp. 301–311, 2013.
- [14] F. Yang, Z.-F. Ning, D.-T. Kong, and H.-Q. Liu, "Pore structure of shale from high pressure mercury injection and nitrogen adsorption method," *Natural Gas Geoscience*, vol. 24, no. 3, pp. 450–455, 2013.
- [15] X. Cao, B. Yu, X. Li, M. Sun, and L. Zhang, "Reservoir characteristics and evaluation on logging of the Lower Cambrian gas shale in southeast Chongqing: a case study of Well Yuke 1 and Well Youke 1," *Acta Petrolei Sinica*, vol. 35, no. 2, pp. 233–244, 2014.
- [16] X. Liu, J. Xiong, and L. Liang, "Investigation of pore structure and fractal characteristics of organic-rich Yanchang formation shale in central China by nitrogen adsorption/desorption analysis," *Journal of Natural Gas Science and Engineering*, vol. 22, pp. 62–72, 2015.
- [17] E. M. Schlueter, R. W. Zimmerman, P. A. Witherspoon, and N. G. W. Cook, "The fractal dimension of pores in sedimentary

- rocks and its influence on permeability," *Engineering Geology*, vol. 48, no. 3-4, pp. 199–215, 1997.
- [18] A. P. Radlinski, M. A. Ioannidis, A. L. Hinde et al., "Angstrom-to-millimeter characterization of sedimentary rock microstructure," *Journal of Colloid and Interface Science*, vol. 274, no. 2, pp. 607–612, 2004.
- [19] Y. Yao, D. Liu, D. Tang et al., "Fractal characterization of seepage-pores of coals from China: an investigation on permeability of coals," *Computers and Geosciences*, vol. 35, no. 6, pp. 1159–1166, 2009.
- [20] Y. Cai, D. Liu, Z. Pan, Y. Yao, J. Li, and Y. Qiu, "Pore structure and its impact on CH₄ adsorption capacity and flow capability of bituminous and subbituminous coals from Northeast China," *Fuel*, vol. 103, pp. 258–268, 2013.
- [21] L. Chen, K. Tan, J. Liu, and S. Zeng, "Pore structure fractal features of the ore-bearing layer from a sandstone-type uranium deposit, Xinjiang," *Acta Scientiarum Naturalium Universitatis Sunyatseni*, vol. 51, no. 6, pp. 139–144, 2012.
- [22] Y. Yao, D. Liu, D. Tang, S. Tang, and W. Huang, "Fractal characterization of adsorption-pores of coals from North China: an investigation on CH₄ adsorption capacity of coals," *International Journal of Coal Geology*, vol. 73, no. 1, pp. 27–42, 2008.
- [23] C. Zou, D. Dong, S. Wang et al., "Geological characteristics and resource potential of shale gas in China," *Petroleum Exploration and Development*, vol. 37, no. 6, pp. 641–653, 2010.
- [24] S. Wang, *The Study of the Shale (Gas) Features in Upper Ordovician—Lower Silurian, Uplift in the Northern of Guizhou*, Chengdu University of Technology, Chengdu, China, 2013.
- [25] S. Brunauer, P. H. Emmett, and E. Teller, "Adsorption of gases in multimolecular layers," *Journal of the American Chemical Society*, vol. 60, no. 2, pp. 309–319, 1938.
- [26] P. Pfeifer and D. Avnir, "Chemistry in noninteger dimensions between two and three. I. Fractal theory of heterogeneous surfaces," *The Journal of Chemical Physics*, vol. 79, no. 7, pp. 3369–3558, 1983.
- [27] D. Avnir and M. Jaroniec, "An isotherm equation for adsorption on fractal surfaces of heterogeneous porous materials," *Langmuir*, vol. 5, no. 6, pp. 1412–1433, 1989.
- [28] M. Jaroniec, "Evaluation of the fractal dimension from a single adsorption isotherm," *Langmuir*, vol. 11, no. 6, pp. 2316–2317, 1995.
- [29] J. Rouquerol, D. Avnir, C. W. Fairbridge et al., "Recommendations for the characterization of porous solids," *International Union of Pure and Applied Chemistry*, vol. 66, no. 8, pp. 1739–1758, 1994.
- [30] C. R. Clarkson, N. Solano, R. M. Bustin et al., "Pore structure characterization of North American shale gas reservoirs using USANS/SANS, gas adsorption, and mercury intrusion," *Fuel*, vol. 103, pp. 606–616, 2013.
- [31] D. Strapoć, M. Mastalerz, A. Schimmelmann, A. Drobnik, and N. R. Hasenmueller, "Geochemical constraints on the origin and volume of gas in the New Albany Shale (Devonian–Mississippian), eastern Illinois Basin," *AAPG Bulletin*, vol. 94, no. 11, pp. 1713–1740, 2010.
- [32] D. J. K. Ross and R. M. Bustin, "Characterizing the shale gas resource potential of Devonian–Mississippian strata in the Western Canada sedimentary basin: application of an integrated formation evaluation," *AAPG Bulletin*, vol. 92, no. 1, pp. 87–125, 2008.
- [33] F. P. Wang and R. M. Reed, "Pore networks and fluid flow in gas shales," in *Proceedings of the SPE Annual Technical Conference and Exhibition*, New Orleans, La, USA, October 2009.
- [34] S. Brunauer, L. S. Deming, W. E. Deming, and E. Teller, "On a theory of the van der Waals adsorption of gases," *Journal of The American Chemical Society*, vol. 62, no. 7, pp. 1723–1732, 1940.
- [35] S. J. Gregg and K. S. W. Sing, *Adsorption, Surface Area, and Porosity*, Academic Press, New York, NY, USA, 1982.
- [36] K. S. W. Sing, D. H. Everett, R. A. W. Haul et al., "Reporting physisorption data for gas/solid systems with special reference to the determination of surface area and porosity," *Pure and Applied Chemistry*, vol. 57, no. 4, pp. 603–619, 1985.